Fluid Dynamic Modeling of Biological Fluids: From the Cerebrospinal Fluid to Blood Thrombosis

(Article begins on next page)

16 July 2022

Doctoral Dissertation
Doctoral Program in Environmental and Civil Enginering (32.th cycle)

Fluid Dynamic Modeling of Biological Fluids: From the Cerebrospinal Fluid to Blood Thrombosis

Modeling of biological fluids: interactions of the cerebrospinal fluid pulsatility with the spinal cord and with intrathecally administrated drugs and thrombus formation in the cardiovascular system.

Giulia Cardillo
* * * * * *

Supervisors
Prof. C., Camporeale
Prof. A.I., Barakat

Doctoral Examination Committee:
Prof. Repetto Rodolfo., Referee, University of Genoa
Dr., Giuseppe Pontrelli, Referee, CNR research director
Prof. Espa Stefania, University of Rome La Sapienza
Prof. Toro Eleuterio Francisco, University of Trento
Prof. Jean Marc Chomaz, École Polytechnique of Paris
Prof. Costantino Manes, Polytechnic of Turin

Politecnico di Torino
2 September 2020

I hereby declare that, the contents and organisation of this dissertation constitute my own original work and does not compromise in any way the rights of third parties, including those relating to the security of personal data.

....

Giulia Cardillo

Turin, 2 September 2020

Summary

Understanding and modeling fluid dynamics and transport processes in the human body is a crucial aspect in biomedical research, which has received a growing attention in the last decades.

In the present thesis, three mathematical models are described. Three different biomedical issues, where fluid dynamical aspects are of paramount importance, are modeled: i) Fluid-structure interactions between cerebro-spinal fluid pulsatility and the spinal cord (analytical modeling); ii) Enhanced dispersion of a drug in the subarachnoid space (numerical modeling); and iii) Thrombus formation and evolution in the cardiovascular system (numerical modeling).

The cerebrospinal fluid (CSF) is a liquid that surrounds and protects the brain and the spinal cord. Insights into the functioning of cerebrospinal fluid are expected to reveal the pathogenesis of severe neurological diseases, such as syringomyelia that involves the formation of fluid-filled cavities (syrinxes) in the spinal cord. Furthermore, in some cases, analgesic drugs – as well drugs for treatments of serious diseases such as cancers and cerebrospinal fluid infections – need to be delivered directly into the cerebrospinal fluid. This underscores the importance of knowing and describing cerebrospinal fluid flow, its interactions with the surrounding tissues and the transport phenomena related to it. In this framework, we have proposed: a model that describes the interactions of the cerebrospinal fluid with the spinal cord that is considered, for the first time, as a porous medium permeated by different fluids (capillary and venous blood and cerebrospinal fluid); and a model that evaluates drug transport within the cerebrospinal fluid-filled space around the spinal cord –namely the subarachnoid space–.

The third model deals with the cardiovascular system. Cardiovascular diseases are the leading cause of death worldwide, among these diseases, thrombosis is a condition that involves the formation of a blood clot inside a blood vessel. A computational model that studies thrombus formation and evolution is developed, considering the chemical, bio-mechanical and fluid dynamical aspects of the problem in the same computational framework. In this model, the primary novelty is the introduction of the role of shear micro-gradients into the process of thrombogenesis.

The developed models have provided several outcomes. First, the study of the fluid-structure interactions between cerebro-spinal fluid and the spinal cord has

shed light on scenarios that may induce the occurrence of Syringomyelia. It was seen how the deviation from the physiological values of the Young modulus of the spinal cord, the capillary pressures at the SC-SAS interface and the permeability of blood networks can lead to syrinx formation. The computational model of the drug dispersion has allowed to quantitatively estimate the drug effective diffusivity, a feature that can aid the tuning of intrathecal delivery protocols.

The comprehensive thrombus formation model has provided a quantification tool of the thrombotic deposition evolution in a blood vessel. In particular, the results have given insight into the importance of considering both mechanical and chemical activation and aggregation of platelets.

Sommario

Lo studio del comportamento dei fluidi nel corpo umano, la loro circolazione e i relativi fenomeni di trasporto sono diventati un aspetto cruciale nella ricerca biomedica e negli ultimi anni la modellazione fluidodinamica sta ricevendo sempre maggiore attenzione.

Nel presente lavoro di tesi tre modelli matematici sono stati proposti, al fine di modellizzare altrettanti complessi aspetti della biomedica, nei quali la fluidodinamica del sistema gioca un ruolo fondamentale: i) le interazioni fluido-struttura tra la pulsatilità del fluido cerebro-spinale e il midollo spinale; ii) la dispersione effettiva di un farmaco all'interno dello spazio subaracnoideo; e iii) la formazione e l'evoluzione di un trombo all'interno del sistema cardiovascolare.

Il fluido cerebrospinale è un liquido simile all'acqua che circonda il cervello e il midollo spinale, allo scopo di proteggerli. Una conoscenza dettagliata della circolazione del liquido cerebrospinale e della sua interazione con i tessuti, può essere significativa nello studio della patogenesi di gravi malattie neurologiche, come la siringomielia, un disturbo che comporta la formazione di cavità piene di liquido (siringhe) nel midollo spinale.

Inoltre, in alcuni casi, i farmaci analgesici - nonché i farmaci per il trattamento di malattie gravi come tumori e infezioni del fluido cerebrospinale - devono essere somministrati direttamente nel fluido cerebrospinale. Si rende chiara quindi l'importanza di conoscere e descrivere il flusso del liquido cerebrospinale, le sue interazioni con i tessuti circostanti e i fenomeni di trasporto ad esso correlati. In questo contesto, abbiamo proposto: un modello capace di descrivere le interazioni del liquido cerebrospinale con il midollo spinale, considerando quest'ultimo, per la prima volta, come un mezzo poroso permeato da differenti fluidi (sangue capillare e venoso e liquido cerebrospinale); e un modello in grado di valutare il trasporto di un farmaco all' interno dello spazio subaracnoideo, una cavità anulare piena di fluido cerebrospinale che circonda il midollo spinale.

Il terzo modello proposto riguarda il sistema cardiovascolare. In tutto il mondo, le malattie cardiovascolari rappresentano la prima causa di mortalità. Tra queste troviamo la trombosi, una condizione che comporta la formazione di un coagulo all'interno di un vaso sanguigno, arrivando anche all'occlusione dello stesso. A tal riguardo si è sviluppato un modello computazionale che studi la formazione

e l'evoluzione dei trombi, considerando contemporaneamente gli aspetti chimico-biomeccanici e fluidodinamici del problema. Nel modello proposto per la prima volta si tiene conto dell'importante ruolo rivestito dai gradienti dello sforzo di taglio nel processo di trombogenesi.

I modelli sviluppati hanno fornito diversi interessanti risultati. In primo luogo, lo studio delle interazioni fluido-struttura tra il fluido cerebro-spinale e il midollo spinale ha messo alla luce le condizioni che possono indurre l'insorgenza della Siringomielia. Si è osservato come la deviazione dai valori fisiologici del modulo di Young del midollo spinale, delle pressioni capillari all'interfaccia midollo-spazio subarcnideo e della permeabilità dei comparti capillare e venoso, possano portare alla formazione di siringhe.

Il modello computazionale circa la valutazione della dispersione di un soluto all'interno dello spazio subaracnideo ha permesso di stimare quantitativamente la diffusività efficace di un farmaco, una grandezza che consentirebbe l'ottimizzazione di protocolli per le iniezioni intratecali.

Il modello di trombogenesi ha fornito uno strumento in grado di studiare quantitativamente l'evoluzione della deposizione piastrinica nel flusso sanguigno. In particolare, i risultati hanno fornito importanti informazioni circa la necessità di considerare il ruolo dell'attivazione e aggregazione meccanica delle piastrine accanto a quella chimica.

Résumé

L'étude du comportement des fluides dans le corps humain, leur circulation et les phénomènes de transport associés sont devenus un aspect crucial de la recherche biomédicale et ces dernières années, la modélisation de la dynamique des fluides a reçu une attention croissante. Dans cette thèse, trois modèles mathématiques ont été proposés, avec l'objectif de modéliser autant d'aspects complexes de la biomédecine, dans lesquels la dynamique des fluides du système joue un rôle fondamental: i) les interactions fluide-structure entre la pulsatilité du liquide céphalorachidien et la moelle épinière (modélisation analytique); ii) dispersion efficace d'un médicament dans l'espace sous-arachnoïdien (modélisation numérique); et iii) la formation et l'évolution d'un thrombus au sein du système cardiovasculaire (modélisation numérique). Le liquide céphalorachidien est un fluide aqueux qui entoure le cerveau et la moelle épinière afin de les protéger. Une connaissance détaillée de la circulation du liquide céphalorachidien et de son interaction avec les tissus peut être importante dans l'étude de la pathogenèse de maladies neurologiques graves, telles que la syringomyélie, un trouble qui implique la formation de cavités remplies de liquide (seringues) dans la moelle épinière. Par ailleurs, dans certains cas, des analgésiques - ainsi que des médicaments pour le traitement de maladies graves telles que les tumeurs et les infections du liquide céphalorachidien - doivent être administrés directement dans le liquide céphalorachidien. L'importance de connaître et de décrire l'écoulement du liquide céphalorachidien, ses interactions avec les tissus environnants et les phénomènes de transport qui y sont liés devient claire. Dans ce contexte, nous avons proposé: un modèle capable de décrire les interactions du liquide céphalo-rachidien avec la moelle épinière, considérant cela, pour la première fois, comme un milieu poreux imprégné de différents fluides (sang capillaire et veineux et liquide céphalo-rachidien); et un modèle capable d'évaluer le transport d'un médicament dans l'espace sousarachnoïdien, une cavité annulaire remplie de liquide céphalo-rachidien qui entoure la moelle épinière. Avec le troisième modèle proposé, nous entrons dans le système cardiovasculaire. Dans le monde entière, les maladies cardiovasculaires sont la cause principale de mortalité. Parmi ceux-ci, nous trouvons la thrombose, une condition qui implique la formation d'un caillot à l'intérieur d'un vaisseau sanguin, qui peut causer sa occlusion. À cet égard, un modèle numérique a été développé qui étudie la formation et l'évolution des

thrombus, en considérant simultanément les aspects chimico-biomécaniques et dynamiques des fluides du problème. Dans le modèle proposé pour la première fois, l'importance du rôle joué par les gradients de contrainte de cisaillement dans le processus de thrombogenèse est pris en compte. Les modèles sélectionnés ont fourni des résultats intéressants. Tout d'abord, l'étude des interactions fluide-structure entre le liquide céphalo-rachidien et la moelle épinière a mis en évidence es conditions pouvant induire l'apparition de la syringomyélie. Il a été observé comment la déviation des valeurs physiologiques du module d'Young de la moelle épinière, les pressions capillaires dans l'interface moelle-espace sousarachnoïdien et la perméabilité des compartiments capillaire et veineux, conduisent à la formation de seringues. Le modèle de calcul pour l'évaluation de la dispersion pharmacologique dans l'espace sousarachnoïdien a permis une estimation quantitatif de la diffusivité effective du médicament, une quantité qui peut aider à l'optimisation des protocoles d'injections intrathécales. Le modèle de thrombogenèse a fourni un instrument capable d'étudier quantitativement l'évolution des dépôts de plaquettes dans la circulation sanguine. En particulier, les résultats ont fourni des informations importantes sur la nécessité de considérer le rôle de l'activation mécanique et de l'agrégation des plaquettes aux côtés de la substance chimique.

Acknowledgements

My doctoral journey has been a wonderful and strenuous experience at the same time.

First of all, I sincerely would like to thank my supervisors, Professor Carlo Camporeale and Professor Abdul I. Barakat.

Professor Camporeale has prompted me to do always my best and to rely on my own strength, but when I really have encountered a problem he has always been ready to help me. I admire his way of doing research.

Professor Barakat has been a great supervisor, but when necessary also a friend, he always encouraged me and working with him and his research team has taught me more than I could hope for.

I would also to thank the Professor Jean-Marc Chomaz for his availability and for his useful advice.

Finally, I would like to thank the referees of this thesis, Prof. Rodolfo Repetto and Dr. Giuseppe Pontrelli, for their comments, suggestions and points for reflections to improve my work.

A thanks to all my great colleagues I met over the years. A special thanks to Nicole and Alessia, this journey would not have been the same without you, you are good colleagues, but above all good friends.

Thanks to my "old" colleagues Michele e Lucia that have been close to me despite the distances.

A thanks to my family, my mother who never stopped believing in me, my sister Lucia for her continuous and precious help during these years, my sister Paola, Ninni and Elena that support me every day.

A thanks to my friends Irene, Concetta, Giuseppe who have stuck with me all my life.

Last, but not least, I would like to thank Marco who supports me every day in everything I do, he turn on the light in my dark time.

To my dad and to my grand parents

Contents

List of Tables

List of Figures

Chapter 1

Introduction

Fluids, fluid dynamics, and associated transport processes are part of medicine and life sciences. Understanding and predicting fluid behavior, fluid flow and transport in the human body has become a crucial aspect in biomedical research, and in the past few decades, fluid dynamic modeling, whether analytical, computational or experimental, has received great attention.

Biological fluid flow description encompasses a wide range of spatial and temporal scales. In experimental studies, multiple factors come into play, and it is difficult to single out the contribution of each individual factor on the flow characteristics. Moreover, the setup and design of the experiments can be time consuming and is usually quite expensive. In this perspective, analytical and computational modeling approaches, based on the fundamental principles of physics and adapted to a biological framework, can allow research to elucidate cause-effect relationships and increase our understanding of physiological complex phenomena, in synergy with other approaches [121].

In the biomedical field, analytical and computational fluid dynamical models may serve a great number of different purposes, from the design and/or optimization of cardiovascular or respiratory devices, to the evaluation of the pathogenesis of deseases. An analytical model involves a closed form expression that provides an exact solution to a problem. However, analytical treatments often require an important number of simplifications and assumptions to become tractable, which often limits their ability to tackle physiologically and pathologically relevant scenarios. On the other hand, Computational Fluid Dynamics (CFD) is a largely adopted methodology of computer-based simulation able to solve complex problems in many engineering fields including the biomedical field [66]. In CFD, the solution is an approximation, but the range of problems that can be tackled is wider. Many simulations and numerical models have been used in biomedical applications, particularly in blood flow and respiratory air flow [4]. In recent years, several organizations and regulatory agencies such as the ASME and the US Food and Drug Administration have become fully engaged in formulating CFD-based

verification and validation guidelines to speed up the approval process of medical devices during their research and development phases [14].

In this thesis, three mathematical models, one analytical and two computational, are described. Three different biomedical issues, in which the fluid dynamics of the system plays a fundamental role, are modeled: i) the fluid-structure interactions between cerebro-spinal fluid pulsatility and the spinal cord (analytical modeling); ii) Aris-Taylor drug dispersion in the subarachnoid space (numerical modeling); and iii) the thrombus formation and evolution in the cardiovascular system (numerical modeling).

The cerebrospinal fluid is a liquid that surrounds and protects the brain and the spinal cord, which are the core of the central nervous system. Non-physiological cerebrospinal fluid motion, circulation or production are responsible for the onset of serious neurological diseases [32],[73]. Syringomyelia, for example, is a neurological disease that involves the formation of cerebrospinal fluid-filled cavities inside the spinal cord; it accounts for about 5 % of paraplegias, and the quality of life for patients with syringomyelia is generally lower than that of the general population, being comparable with that of patients with heart failure or malignant neoplasms [33]. In some cases, analgesic drugs need to be delivered directly into the cerebrospinal fluid as is the case for some treatments of other serious diseases such as cancers and cerebrospinal fluid infection [69]. This underscores the importance of knowing and describing cerebrospinal fluid flow, its interactions with the surrounding tissues and the transport phenomena related to it. In this context, a model that describes the interactions of the cerebrospinal fluid with the spinal cord and a model that evaluates drug transport within the cerebrospinal fluid-filled space around the spinal cord –namely the subarachnoid space–are proposed here.

The main novelty of the fluid-structure interaction model presented here is that it considers the involvement of the fluids that permeate the spinal cord, blood (capillary and venous) and cerebrospinal fluid, thus modeling the spinal cord not only as a porous medium but also as one permeated by different fluids.

The drug dispersion model described in this thesis is necessary for testing the hypothesis and the results obtained through an analytical model developed by members of this research team, Prof. Camporeale and Luca Salerno [104].

The third proposed model moves to the cardiovascular system. Cardiovascular diseases are the leading cause of death worldwide [28]. An important cardiovascular disease is thrombosis, a condition that involves the formation of a blood clot inside a blood vessel, obstructing the flow. Thrombosis and thromboembolism remain significant sources of morbidity and mortality in cardiovascular device patients. In this thesis, a computational model that studies thrombus formation and evolution, considering simultaneously the chemical, bio-mechanical and fluid dymanical aspects of the problem, is developed. In this model, the primary novelty is the introduction of the role of shear gradients into the process of thrombogenesis.

The Thesis is organized as follows. In the second Chapter, after a description

of the anatomy of the spinal cavity, the analytical modeling of the fluid-structure interactions between the cerebro-spinal fluid pulsatility and the spinal cord is presented along with its results. The third chapter is dedicated to modeling and results of Aris-Taylor drug dispersion in the subaracnhnoid space. In the fourth chapter the hemostatic process, the computational modeling of thrombus formation and the associated results are presented.

Chapter 2

Modeling the interactions of the cerebrospinal fluid pulsatility with the spinal cord

The model described in this chapter was submitted to the Journal of Fluids and Structures and the paper is currently under review.

The fluid dynamics of Cerebrospinal Fluid (CSF) and its interaction with the brain and the Spinal Cord (SC) play a fundamental role in the formation and evolution of neurological diseases [32]. Notable examples are Hydrocefalus, a disorder that leads to an increase in CSF volume in the cranial cavity, and Syringomyelia, a disease that involves the formation of longitudinal macroscopic fluid-filled cavities (syrinxes) within the spinal cord. The aetiology of such disorders remains uncertain. In this perspective, a mathematical model capable of evaluating the interactions of the cerebrospinal fluid pulsatility with the spinal cord, taking into account its porosity and the fluids within it, can be a very useful tool. In this chapter a fully analytical fluid-structure interaction model that couples the cerebrospinal fluid flow field in the Subarachnoid Space (SAS) with the pressures and displacement field inside the spinal cord is presented.

2.1   The Spinal cavity

The spinal cavity identifies the canal, inside the vertebral column, formed by the vertebrae in which the spinal cord and its membranes are located. The spinal cord is located at the center of the spinal cavity and it is sorrounded by a thin annular cavity, named the sub-arachnoid space (SAS), see Fig.2.1. Cerebrospinal fluid (CSF), a Newtonian fluid, similar to water, fills the SAS, it within which exhibits a pulsalite laminar flow. The subarachnoid space is bounded on the inner side by the pia mater, a meninx that covers the spinal cord. The pia mater

is a thin fibrous tissue that is deformable and permeable to CSF and some small solutes [50]. On the outer side there are two attached meninges: more internally the arachnoid, which is impermeable and non-vascularized and externally the dura mater, which is rigid, dense and tough [43] and separates the SAS from the epidural space. The spinal subarachnoid space has 25 ml volume and it is traversed by a variety of trabeculae, nerve roots, and dentate ligaments that consist of collagenous and connective tissues and stretch between arachnoid and pia mater. These fine anatomical structures display a considerable numeric and structural variability along the spinal cavity length [60],[80].

2.1.1 Cerebrospinal fluid

Cerebrospinal fluid is a clear, colourless Newtonian fluid, with a density and kinematic viscosity similar to water at 37°C, that fills the ventricles and the subarachnoid space of the brain and spinal cord.

The total volume of cerebrospinal fluid is approximately 150 ml and it is renewed about four times every 24 hours. CSF lies in the central nervous system either intracerebrally in the ventricular system of the brain (making up 20 % of the total CSF volume) or extracerebrally in the subarachnoid space (the remaining 80 % of the total volume)[103].

CSF originates from the choroid plexuses in the ventricles at a rate of approximately 350 $\mu L/min$ in humans [27], it leaves the ventricular system via the foramina of Luschska and Magendie, flows through cisternae (basal cisternae and the cisterna magna) [33] and through the subarachnoid space and finally drains through the arachnoid villi into venous blood.

Two components can be distinguished in CSF flow: (i) bulk flow (circulation) and (ii) laminar pulsatile flow. In bulk flow theory, CSF is produced by choroid plexus and absorbed by arachnoid granulations and villi. The force, which provides CSF movement from the ventricular system to arachnoid granulation and CSF absorption, is caused by a pressure gradient between the site of its formation (slightly high pressure) and its site of absorption (slightly low pressure)[5]. The CSF pulsatile flow results from the variation of the cerebrovascular blood and choroid plexus volume related to cardiac cycle. As follows from conservation of intracranial volume stated by the Monro–Kellie doctrine [79], these pressure fluctuations drives CSF periodically into and out of the subarachnoid space; they are also modulated by other physiological factors, such as the respiratory rate. The pulsatile flow – with a maximum velocity of 3-8 cm/s [73] – is more significant than bulk flow, because very little CSF truly circulates through the subarachnoid space so much so that the magnitude of the CSF eliminated by the spinal canal is undetectable from CINE-MRI measurements [5].

Through its pulsatile flow, CSF allows for the modulation and regulation of intracranial pressure (ICP). Furthermore CSF has other important functions: i) to

protect the brain and the spinal cord from mechanical shocks acting as a cushion and a shock absorber [54]; ii) to support the brain hydrostatically, reducing its weight by two-thirds [110]; iii) to help to maintain the correct composition of the environment surrounding nervous tissue cells and provide the supply of nutrients and disposal of the metabolic waste products (metabolic functions) [103],[137].
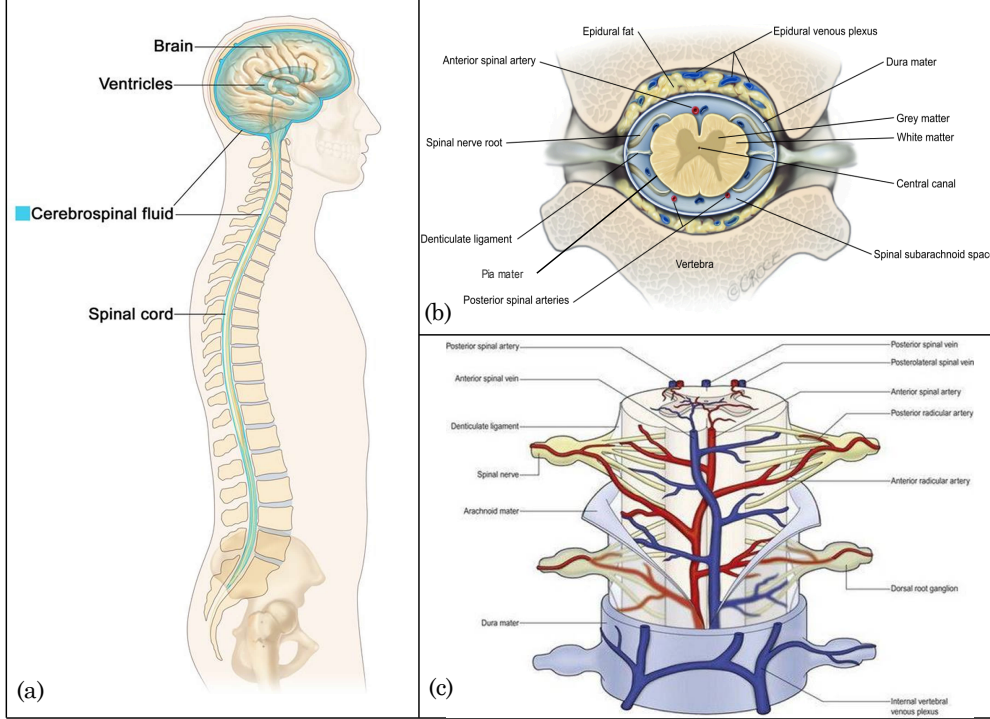
Figure 2.1: Anatomy of the spinal cavity. (a) Longitudinal view of the vertebral column. (b) Cross-section of the vertebral column (image taken from [32]). (c) Blood supply system of the spinal cord

2.1.2 Spinal Cord

The spinal cord (SC) is a fundamental part of the central nervous system, it is responsible for the transmission of both motor and sensory impulses between the brain and the body via 31 pairs of nerves which join the cord at intervals along its length [32]. The spinal cord (approximately 40–45 cm long and 1 cm thick) extends caudally in the vertebral column and is protected by the subarachnoid space. It is covered by the three meninges, i.e., the dura mater, arachnoid and the pia mater and it can be divided into four parts: cervical, thoracic, lumbar and sacral [85].

Unlike the brain, the spinal cord is composed by grey and white matter. The grey matter is surrounded by the white matter at its circumference. The spinal grey matter is crescent-shaped, although its arrangement and proportion to the white matter vary at different rostrocaudal levels [85]. The gray and white matter behave as porous-elastic media and are permeated by three fluid compartments capillaries and veins – that vascularize the spinal cord tissue – and the cerebrospinal fluid. Capillaries, veins and CSF interact each other. The arteries (posterior and anterior arteries) run outside the spinal cord (see figure 2.1(c)).

At the center of the spinal cord the central canal lies, a very small conduit filled with cerebrospinal fluid that runs along the entire length of the spinal cord (see figure 2.1(b)).

2.2   Syringomyelia

Syringomyelia is a neurological disease that involves the formation of elongated fluid-filled cavity within spinal cord. Syrinx describes the shape of the syringomyelic cyst, often tapered at the upper and lower ends [33] (see Fig.2.2). The cervical region of the spinal cord is most frequently involved, and four types of syringomyelia have been described:

Type I syringomyelia is associated with obstruction of the foramen magnum, namely the large opening in the occipital bone of the skull, with a Chiari type 1 malformation – structural abnormality of the cerebellum ("little brain")– or another obstructive lesion, such as fibrosis or tumour.

Type II syringomyelia is without obstruction of the foramen magnum and is so-called idiopathic.

Type III syringomyelia is associated with other diseases of the spinal cord such as spinal tumours, traumatic lesions of the cord and spinal arachnoiditis.

Type IV is hydromyelia usually associated with hydrocephalus. Hydromyelia corresponds to a dilatation of the central canal. Dilatation may be focal and more pronounced in the lumbar spinal cord. Hydromyelia may be an isolated finding and asymptomatic, or it may be part of a more complex syndrome [33].

2.3   State of the art

All fluid flow problems in the human body involve fluid-structure interactions [25].

The wall-fluid interactions in physiological flow, especially in hemodynamics field, have been widely studied and different mathematical methods and approaches have been developed [93].

Recently a growing interest in modelling the cerebrospinal fluid flow allows the development of important mathematical studies that describe CSF fluid dynamics
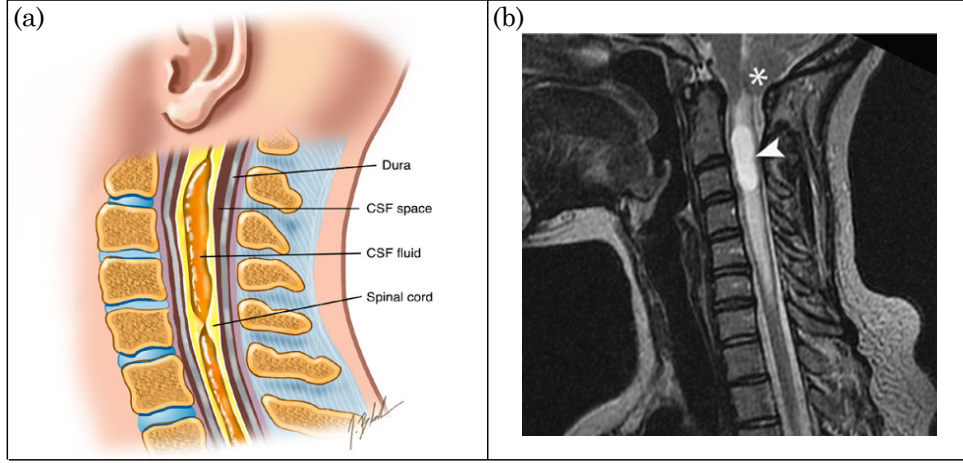
Figure 2.2: Syringomyelia. (a) Graphycal representation of the desease (image taken from [124]) (b) MRI image of a syrinx (indicated by the arrow) associated with Chiari I malformation (indicated by the star) (image taken from [32])

and its interactions with the spinal cord. Within the context of numerical approaches, Bertram et al. [9], initially developed a two-dimensional axi-symmetric numerical model of the spinal cord and the SAS, excited by pressure transients and with a distal reflecting site models scar tissue, which is commonly associated with syrinx formation . In 2009, Bertram [7] developed a fluid-structure interaction numerical model able to investigate the waves propagating in the spinal cord and the SAS, in the presence of a syrinx. Subsequently, aiming to study the nexus between Syringomielia and the Chiari Malformation, a similar numerical model investigated the effects of SAS stenosis on an adjacent syrinx localized in the spinal cord [8], and then also considering spinal cord porosity [46], [10]. Other numerical investigations considered the role of the elasticity or poroelasticity of spinal cord tissue [118] by simulating the propagation of pressure waves through an anatomically plausible 3D geometry, with boundary conditions based on in-vivo CSF pressure measurements. Three-dimensional numerical approaches determined the effects of fluid-structure interaction on CSF pressure and spinal cord motion – considered as a solid elastic medium – in a stenosis model of the spinal subarachnoid space [20]. Furthermore, with the aim of modeling pathological features, the eigenvalue problem was solved for a two-dimensional elastic fluid-solid cylindrically layered wave-guide [30].

Within the context of analytical approaches, a standard linear small-amplitude analysis of wave propagation was developed by Cirovic [23] for a system consisting of coaxial tubes of finite thickness, filled with inviscid incompressible fluid, in order to

model the CSF pulse in the spinal column. Subsequently, one-dimensional modeling of the spinal column simulated CSF pulses excited by pressure disturbances in the subarachnoid and epidural spaces by considering both the spinal cord and the dura mater as elastic structures [24]. Berkouk, Carpenter, and Lucey [6] examined the possibility that shock-like elastic jumps may initiate the formation of cysts in the spinal cord, whereas Elliott[31] developed a pair of one-dimensional analytical models borrowed from the elastic tube theory and coupled with Darcy's law for perivascular and interstitial flow, in order to investigate the role played in syrinx filling by wave-induced fluid exchanges across the pia mater.

Despite these valuable studies, a fully analytical wholly-coupled fluid-structure interaction model that considers the spinal cord as a porous medium permeated by different fluids (capillary, venous blood and CSF) is still lacking. To this regard, the present paper aims to show a model that accounts for the coupling between the flow field in the SAS, the pressures and displacement field inside the spinal cord.

2.4 Methods: Modeling the interactions of the CSF with the spinal cord

In the present work, the spinal cord, the subarachnoid space and the central canal are modeled as three coaxial infinite tubes (see Figure 2.3). The interface between the spinal cord and the subarachnoid space is considered deformable and the Central Canal (CC) is modeled in the center of the cord.

We anticipate that similarly to the well-known Womersley formulation for the blood flow solution in arteries [135], a transient pressure gradient in the SAS was imposed.

Furthermore, analogously to blood-wall interactions formulation for the arteries [93] [23], under the hypothesis of small deformation, the spinal cord dynamic is described in the framework of linear elasticity theory. At the same time, in order to model the porous nature of the spinal cord and the different fluids –capillary and venous blood and CSF– that permeate it, we adopted the Multiple network Porous-Elastic Theory (MPET), initially introduced in geomechanics for naturally fractured reservoirs, and then extended to model water transport in the brain in order to explore the etiology of hydrocephalus [127]. The MPET medium comprises a low-porosity solid matrix and high-porosity fissures filled by the fluid compartments.

2.4.1 Modeling the flow in the Subarachnoid Space

The pulsatile flow of the cerebrospinal fluid in the subarachnoid space is described by Navier-Stokes equations. In order to simplify the analytical treatment, it is convenient to assume axial symmetry and recast the governing equations in
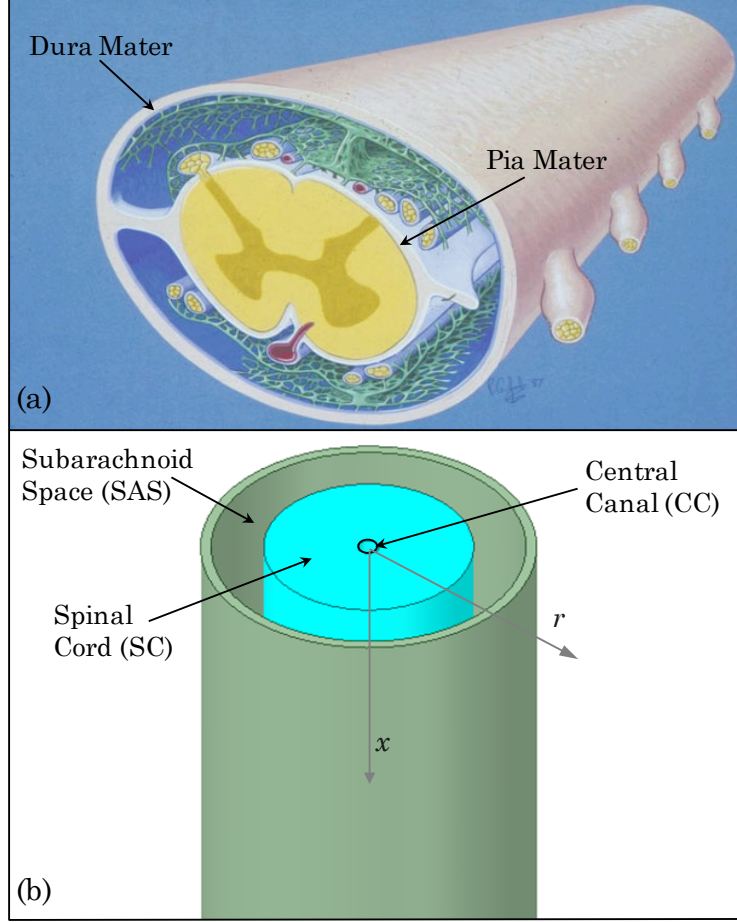
Figure 2.3: Spinal cavity: (a) Anatomy (figure taken from [33]) (b) Schematization of the problem

cylindrical coordinates with the following dimensionless quantities

$$\tilde{x} = \frac{x}{L}, \quad \tilde{r} = \frac{r}{R}, \tag{2.1}$$

$$\tilde{P} = \frac{P\rho\kappa}{\mu^2}, \quad \tilde{t} = \frac{2\pi t}{T_0}, \quad \tilde{\omega} = \frac{\omega T_0}{2\pi}, \quad \tilde{k} = kL, \quad \tilde{v} = vV_0, \tag{2.2}$$

where x is the longitudinal coordinate, r the radial coordinate, P the pressure, L and R are the length and the radius of the spinal cord, respectively, μ and ρ are the dynamic viscosity and density of the cerebrospinal fluid, κ is the intrinsic permeability of the cerebrospinal fluid network, T_0 is a reference period, ω and k are

the angular frequency and the wave-number of the pulse pressure, respectively, and V_0 is a characteristic velocity of the pulsatile flow. For the pressure P, eqs.(2.2), it was decided to consider a scaling factor that was representative of the pore pressures inside the spinal cord (see *Modeling the spinal cord* section).

In the present dimensionless notation, the longitudinal component of the Navier-Stokes equations and the continuity equation read,

$$\xi_1 \frac{\partial v_x}{\partial t} + \delta Re \left(v_x \frac{\partial v_x}{\partial x} + v_r \frac{\partial v_x}{\partial r} \right) + \xi_2 \frac{\partial P}{\partial x} = \delta^2 \frac{\partial^2 v_x}{\partial x^2} + \frac{\partial^2 v_x}{\partial r^2} + \frac{1}{r} \frac{\partial v_x}{\partial r}, \qquad (2.3)$$

$$\frac{\partial v_x}{\partial x} + \frac{\partial v_r}{\partial r} + \frac{v_r}{r} = 0, \qquad (2.4)$$

where tilde has been removed for brevity, v_x and v_r are the axial and the radial components of the velocity, $\delta = \frac{R}{L}$ is the aspect ratio, $\xi_1 = 2\pi R^2 \rho / T_0 \mu$, $\xi_2 = \mu R^2 / \rho \kappa L V_0$ and $Re = \rho R V_0 / \mu$ is the Reynolds number.

It is worth to notice that the dimensionless coefficient $\xi_1 = 2\pi R^2 \rho / T_0 \mu$ is the square of the well-known Womersley number [135] representing the ratio between the transient inertial forces and the viscous forces. The present system is characterized by a Womersley number of around 12.

In order to set the boundary conditions, we recall that the interface between the spinal cord and the cerebrospinal fluid – the pia mater – is a deformable surface, so it can be described by the function $\zeta(x,t)$. In contrast, the dura mater is supposed impermeable and non-deformable [71], [6]. No slip conditions and the impermeability of the dura mater read

$$v_x|_{r=1+\zeta} = v_x|_{r=r_d} = v_r|_{r=r_d} = 0, \qquad (2.5)$$

where the specifications r_d and $1+\zeta$ refer to the outer and the inner SAS boundaries, respectively.

From a physiological point of view, the CSF is periodically pushed from the head in the SAS, because of pulsations, related to cardiac cycle, of the choroid plexus and the intracranial arteries–that increase their volume during the systole–. In this framework, it was decided to impose a transient pressure in the SAS, in the form of propagating wavelets injected into the cranial end as a sum of hydrostatic and dynamic pressure,

$$P = \bar{P}_e + P_0 \frac{\rho \kappa}{\mu^2} e^{i(kx-\omega t)} + c.c, \qquad (2.6)$$

where *c.c.* refers to complex conjugation.

The hydrostatic component is simply related to the CSF volume contained in the annular cavity [95]. The dynamic component is instead due to the changes in the intracranial blood volume during the cardiac cycle. Under physiological conditions P_0 ranges between 0.75 mmHg [9] and 3 mmHg [26] and the oscillation frequency

ω can be assumed equal to the cardiac pulse rate $-\sim 1$ Hz in case of normocardial subject$-$. The wave number k is assumed to be known and it is related to the deformability of the spinal cord since $k = \frac{\omega}{c}$ and $c^2 = E/2\rho(1+\nu)$.

We anticipate that the structure of eq. (2.6) suggests the ansatz for the solution of the flow field in the wavelet form

$$\{v_x, v_r\} = \{\hat{v}_x, \hat{v}_r\}e^{i(kx-\omega t)} + c.c. \tag{2.7}$$

2.4.2 Modeling the spinal cord

Following the MPET approach, we consider the Spinal Cord (SC) as a solid matrix – henceforth referred to with subscript s – permeated by three different fluids, namely the capillary blood network, the CSF network and the venous network (referred to with superscripts c, e and v, respectively).

Each network is characterized by its porosity ϕ^a, density ρ^a, permeability κ^a, pressure p^a and fluid velocity relative to the solid matrix w_i^a/ϕ^a, with $a=\{c,e,v\}$ [127]. The governing equations of the whole system are: i) momentum conservation of the complete solid-fluid system; ii) momentum conservation for the fluid of each network; iii) mass conservation for each fluid network. The general form of the equation of motion of the entire system reads [143]

$$\frac{\partial \sigma_{ij}}{\partial x_i} + \rho(b_i - \ddot{u}_i) = \sum_{a=1} \rho^a \left(\dot{w}_i^a + w_j^a \frac{\partial w_i^a}{\partial x_j} \right), \tag{2.8}$$

where σ_{ij} is the total stress in the poroelastic medium, b_i is the local body force (e.g., gravity), u_i is the displacement of the solid matrix. It is assumed that the coordinate frame x_i moves with the solid phase and hence the convective acceleration rises only for the fluid phase. The stress in the solid matrix can be described by the extension to multiple fluid networks of Terzaghi's principle [125] and Biot's theory [13]

$$\sigma_{ij} = \sigma'_{ij} - \sum_a \alpha^a \delta_{ij} p^a, \tag{2.9}$$

where σ_{ij} is the total stress acting on the saturated solid matrix, and σ'_{ij} is the effective stress (i.e., the force per unit area loaded on the solid skeleton), p^a is the pore pressure and α is the so-called Biot coefficient, i.e., the ratio of the fluid volume squeezed out to the change of the total porous medium volume under isotropic compression [12]. The momentum conservation of each fluid network states the balance between pore pressure gradient, external forces, viscous drag $\boldsymbol{R}^a$ and the acceleration of the fluid relative to the solid matrix, namely

$$\rho^a(b_i - \ddot{u}_i) - \frac{\partial p^a}{\partial x_i} - R_i^a = \frac{\rho^a}{\phi^a} \left(\dot{w}_i^a + w_j^a \frac{\partial w_i^a}{\partial x_j} \right). \tag{2.10}$$

13

Here the viscous drag is assumed to follow Darcy's law $\bar{k}_{ij}^a R_j^a = w_i^a$, being $\bar{k}_{ij}^a$ the hydraulic conductivity of the fluid network. Mass conservation of each fluid network involves the rate of change of the fluid content as a function of the compressibility of the system for a given strain rate, the flux of the fluid through the matrix and any source or sink [127]. Assuming fluid incompressibility, it reads

$$\frac{\dot{p}^a}{Q} + \alpha^a \dot{\epsilon}_{ii} + \frac{\partial w_i^a}{\partial x_i} = \sum_{a \neq b} \dot{s}_{b \to a}, \tag{2.11}$$

where $\dot{\epsilon}_{ii}$ is the trace of the rate of deformation tensor of the solid matrix, and $\dot{s}_{b \to a}$ is the volumetric flux from network b to network a, while

$$\frac{1}{Q} = \frac{\phi^a}{K_f} + \frac{\alpha^a - \phi^a}{K_s}, \tag{2.12}$$

being Q the combined compressibility of the fluid and solid phases, which can be related, following the Zienkiewicz formulation [143], to the bulk moduli of each component –K_f and K_s are the fluids and solid bulk moduli respectively–.

Since the accelerations are usually small, the right-hand side of (2.8) and (2.10) can be safely neglected. Combining equation (2.8) with (2.9), and (2.10) with (2.11) we obtain, respectively

$$\frac{\partial \sigma'_{ij}}{\partial x_j} + \alpha^a \delta_{ij} \frac{\partial p^a}{\partial x_j} + \rho(b_i - \ddot{u}_i) = 0, \tag{2.13}$$

$$\frac{\dot{p}^a}{Q} + \alpha^a \dot{\epsilon}_{ii} - \frac{\partial}{\partial x_i}\left(\bar{k}_{ij}^a \frac{\partial p^a}{\partial x_j}\right) + \bar{k}_{ij}^a \rho^a(b_i - \ddot{u}_i) - \sum_{b \neq a} \dot{s}_{b \to a} = 0. \tag{2.14}$$

The theory of linear elasticity finally imposes that strain, displacements and stresses of the solid matrix satisfy

$$\epsilon_{ij} = \frac{1}{2}\left(\frac{\partial u_i}{\partial x_j} + \frac{\partial u_j}{\partial x_i}\right), \tag{2.15}$$

$$\sigma'_{ij} = 2G\epsilon_{ij}\frac{\nu\epsilon}{1 - 2\nu}\delta_{ij}, \tag{2.16}$$

where $G = \frac{E}{2(1+\nu)}$ is the shear modulus of the tissue, ϵ is the volumetric strain and ν is the Poisson ratio. Replacing equations (2.15) and (2.16) in (2.13) and (2.14), and considering an isotropic hydraulic conductivity $\bar{k} = \frac{\kappa}{\mu}$, where κ is the permeability of the fluid network and μ the viscosity of the fluid, we recover the poroelastic equations

$$G\nabla^2 \mathbf{u} + \frac{G}{1 - 2\upsilon}\nabla(\nabla \cdot \mathbf{u}) + \sum_a \alpha^a \nabla p^a + \rho(\mathbf{b} - \ddot{\mathbf{u}}) = \mathbf{0}, \tag{2.17}$$

14

$$\frac{1}{Q}\frac{\partial p^a}{\partial t} + \alpha^a\frac{\partial(\nabla\cdot\mathbf{u})}{\partial t} - \bar{k}^a\nabla\cdot[\nabla p^a + \rho^a(\mathbf{b} - \ddot{\mathbf{u}})] - \sum_{\mathbf{j}\neq\mathbf{a}}\dot{\mathbf{s}}_{\mathbf{ij}} = \mathbf{0}, \quad (\mathbf{a} = \mathbf{c}, \mathbf{e}, \mathbf{v}). \quad (2.18)$$

A positive (respectively, negative) value for $|\dot{s}_{i\rightarrow j}|$ represents loss (gain) of fluid from the network i. It is commonplace to adopt a pressure-driven closure for the fluxes, i.e. $|\dot{s}_{ab}| = -\gamma_{ab}(p^a - p^b)$, where gamma is a transfer coefficient [127].

In order to further simplify the analysis, in the following we assume: i) Gravity effects are neglected; ii) A unique value for the Biot coefficient ($\alpha^c = \alpha^v = \alpha^e = \alpha$) and porosity ($\phi^c = \phi^v = \phi^e = \phi$) is considered; iii) The axial deformation of the spinal cord is disregarded, since it is usually very small because of the axial tethering; iv) Axial symmetry is also imposed to the spinal cord. In addition to eqs. (2.1)-(2.2) the following scaling is introduced:

$$\tilde{u}_x = \frac{u_x}{\delta^2 L}, \quad \tilde{u}_r = \frac{u_r}{\delta R}, \quad \tilde{\zeta} = \frac{\zeta}{\delta R}, \quad (2.19)$$

where u_x and u_r are the axial and the radial components of the spinal cord displacement, respectively, as seen $\delta = \frac{R}{L}$ is the slenderness of the body, while ζ is the deformation of the pia mater.

The radial displacement u_r of the solid matrix is an average value over a representative elementary volume being the spinal cord a porous medium. Introducing ζ, it is possible to evaluate the exact value of the deformation of the pia mater, taking into account the porosity of the spinal cord.

We take advantage from the fact that $\delta \ll 1$ (slender body approximation), so after retaining just the dominant terms (i.e., order δ^3 or larger) the final dimensionless form of the governing equations for the spinal cord in cylindrical coordinates read

$$\eta_1\frac{\partial}{\partial x}\left(\frac{\partial u_r}{\partial r} + \frac{u_r}{r}\right) = \eta_2\sum_a\frac{\partial p^a}{\partial x}, \quad (2.20)$$

$$\delta^2\left[\delta\frac{\partial^2 u_r}{\partial x^2} + \frac{1}{r}\frac{\partial}{\partial r}\left(r\frac{\partial u_r}{\partial r}\right) - \frac{u_r}{r^2}\right] + \eta_1\left(\frac{\partial^2 u_r}{\partial r^2} + \frac{1}{r}\frac{\partial u_r}{\partial r} - \frac{u_r}{r^2}\right) = \eta_2\sum_a\frac{\partial p^a}{\partial r}, \quad (2.21)$$

$$\eta_3\frac{\partial p^a}{\partial t} + \delta\alpha\frac{\partial}{\partial t}\left(\frac{\partial u_r}{\partial r} + \frac{u_r}{r}\right) - \eta_4\frac{\partial^2 p^a}{\partial x^2} - \frac{\eta_4}{\delta^2}\left(\frac{\partial^2 p^a}{\partial r^2} + \frac{1}{r}\frac{\partial p^a}{\partial r}\right) = 0, \quad (2.22)$$

where tilde has been removed for brevity and

$$\eta_1 = \frac{\delta}{1 - 2\upsilon}, \quad \eta_2 = \frac{\alpha\mu^2}{\rho\kappa G}, \quad \eta_3 = \frac{\mu^2}{\rho\kappa Q}, \quad \eta_4 = \frac{\mu T_0}{\rho L^2 2\pi}. \quad (2.23)$$

Again, we anticipate that equation (2.6) suggests the putative solution in a wavelet form

$$\{u_r, \zeta, p^a\} = \{0, 0, \bar{P}_a\} + \{\hat{u}_r, \hat{\zeta}, \hat{p}^a\}e^{i(kx - \omega t)} + c.c. \quad (2.24)$$

15

The dimensionless boundary conditions at the interface between the SAS and the spinal cord (i.e., $r = 1 + \zeta$) read (see Appendix A for the dimensional expressions)

$$2\delta\frac{\partial u_r}{\partial r} + 2\eta_1\upsilon\left(\frac{\partial u_r}{\partial r} + \frac{u_r}{r}\right) - \eta_2\sum_{i=c,v,e}p^i = 2\delta\eta_5\frac{\partial v_r}{\partial r} - \frac{\eta_2}{\alpha}P_0, \tag{2.25}$$

$$\delta^3\frac{\partial u_r}{\partial x} = \eta_5\left(\delta^2\frac{\partial v_r}{\partial x} + \frac{\partial v_x}{\partial r}\right) \tag{2.26}$$

$$\{p^v, p^c\} = \{\bar{P}_v, \bar{P}_c\} + \{P_v, P_c\}\cdot e^{i(kx-\omega t)}, \tag{2.27}$$

$$\delta^2 Re\cdot v_x\frac{\partial\zeta}{\partial x} - \delta Re\cdot v_r + \phi\left(\delta^3\frac{\partial p^e}{\partial x}\frac{\partial\zeta}{\partial x} - \frac{\partial p^e}{\partial r}\right) = (1-\phi)\eta_6\frac{\partial\zeta}{\partial t}, \tag{2.28}$$

where ϕ is the porosity of the spinal cord and $\eta_5 = \frac{\mu V_0}{GR}$ and $\eta_6 = \frac{\delta 2\pi R^2\rho}{\mu T_0}$, while $\{\bar{P}_v, \bar{P}_c\}$ in eq. (2.27) are the externally imposed values of the venous and capillary pressures at the pia mater. These values originates from the systemic circulation which feeds the spinal cord. Equations (2.25) and (2.26) impose continuity of the normal stress and tangential stresses, respectively, across the SC-SAS interface. The normal stress on the solid side was obtained considering the extension of the Terzaghi principle of effective stress and Biot's theory to multiple fluid networks (see equation 2.9).

Being the pia mater deformable and permeable, along with the continuity of the stresses, flux mass continuity across the SC-SAS interface must be also guaranteed. To this aim, the kinematic condition is imposed (2.28). This condition specifically derives from a mass balance in a small poro-elastic volume across the interface, by virtue of Darcy's law and it links the deformation of the SC-SAS interface to the other unknowns (see Appendix A for a derivation).

At the interface between the spinal cord and the central canal (i.e., $r=r_i$) we have

$$2\delta\frac{\partial u_r}{\partial r} + 2\eta_1\upsilon\left(\frac{\partial u_r}{\partial r} + \frac{u_r}{r}\right) - \eta_2\sum_{i=c,v,e}p^i + \frac{\eta_2}{\alpha}\bar{P}_e \quad = \quad 0, \tag{2.29}$$

$$u_r = \frac{\partial p^c}{\partial r} = \frac{\partial p^v}{\partial r} \quad = \quad 0. \tag{2.30}$$

Equation (2.29) imposes the continuity of the normal stress at the interface between the central canal (CC) – filled of still cerebrospinal fluid – and the spinal cord (SC). Radial displacement is assumed to be zero at the CC-SC interface, in order to mimic the role of the fine structures – denticulate ligaments, fibrous trabecules, spinal nerves – that constrain the axis of the spinal cord. Axial-symmetry for the capillary and the venous pressure are finally imposed (equation 2.30).

2.4.3 Solutions

In order to enable the use of the boundary conditions on the deformable interface (pia mater), the domain is rectangularized through the following mapping

$$z_s = \frac{r}{1+\zeta} \quad \text{Inside the SC}, \tag{2.31}$$

$$z_e = \frac{r - (1+\zeta)}{r_d - (1+\zeta)} \quad \text{Inside the SAS}. \tag{2.32}$$

In this way z_s and z_e are both mapped into the range $[0,1]$. In particular, the CC axis corresponds to z_s=0, the CC-SC interface corresponds to z_s=r_i –r_i is the (dimensionless) radius of the central canal–,pia mater (SC-SAS interface) corresponds to z_s=1 and z_e=0, while dura mater corresponds to z_e=1.

After recalling eqs. (2.7)-(2.24) and factorising the exponential terms, the ode system reduces to

$$z_s \hat{u}'_r + \hat{u}_r - z_s \frac{\eta_2}{\eta_1} \sum_a \hat{p}^a = 0, \tag{2.33}$$

$$z_s \hat{u}''_r + \hat{u}'_r - \frac{\delta^3 k^2 z_s^2 + \eta_1}{z_s(\delta + \eta_1)} \hat{u}_r - \frac{z_s \eta_2}{\delta + \eta_1} \sum_a (\hat{p}^a)' = 0, \tag{2.34}$$

$$\alpha\delta(z_s \hat{u}'_r + \hat{u}_r) - i\eta_4 \frac{1}{\delta^2}(z_s \hat{p}''_a + \hat{p}'_a) + (\eta_3 + i\eta_4 k^2)z_s \hat{p}_a = 0, \tag{2.35}$$

$$i\hat{v}''_x + \frac{ih}{1 + hz_e}\hat{v}'_x - h^2(\xi_1 + i\delta^2 k^2)\hat{v}_x z_e + h^2 \xi_2 k P_0 = 0, \tag{2.36}$$

$$\hat{v}'_r + \frac{h}{1 + hz_e}\hat{v}_r + ihk\hat{v}_x = 0, \tag{2.37}$$

where h is the (dimensionless) thickness of the subarachnoid space. For the sake of space, we have adopted apex notation for the derivatives with respect to z_e (z_s) in the SAS (SC) domain. The boundary conditions (2.5) and (2.25)-(2.30), reduce to: At z_s=1 (z_e=0):

$$\hat{\zeta}\left(1 - \frac{1}{h}\right)\sum_a \bar{P}_a - \frac{\bar{P}_e}{\alpha} + \sum_a \hat{p}^a - \frac{2}{\eta_2}\left[\nu\eta_1 \hat{u}_r + (\delta + \nu\eta_1)\hat{u}'_r + \frac{\delta\eta_5}{h}\hat{v}'_r\right] - \frac{P_0}{\alpha} = 0, \tag{2.38}$$

$$\frac{i\eta_5}{k\delta}\hat{v}'_x - \eta_5 \hat{v}'_r + \eta_5(1-h)\hat{v}_r - \delta^2 \hat{u}'_r - \delta^2(1-h)\hat{u}_r = 0, \tag{2.39}$$

$$\hat{p}^v - P_v = \hat{p}^c - P_c = \hat{v}_x = 0, \tag{2.40}$$

$$\eta_6(\phi - 1)\hat{\zeta} + i\phi\,(\hat{p}^e)' + i\delta Re\hat{v}_r = 0. \tag{2.41}$$

At z_s=r_i:

$$\left(\sum_a \bar{P}_a - \frac{\bar{P}_e}{\alpha}\right)\hat{\zeta} + \sum_a \hat{p}^a - 2\frac{\delta + \eta_1 \nu}{\eta_2}\hat{u}'_r = 0, \tag{2.42}$$

$$u_r = (\hat{p}^c)' = (\hat{p}^v)' = 0. \tag{2.43}$$

At $z_e = 1$:

$$\hat{v}_x = \hat{v}_r = 0 \tag{2.44}$$

The solutions of the CSF flow field in the SAS are obtained by solving the Navier-Stokes equations (2.36) and (2.37) with no-slip conditions and the impermeability of the dura mater (2.44) and (2.39). Accordingly, we get

$$\hat{v}_x = \frac{\xi_2 k P_0}{c_0}(c_1 I_0[\hat{z}] - I_0[\Gamma] \cdot Y_0[i\hat{z}\Gamma] + I_0[\Gamma] \cdot Y_0[i\Gamma\hat{z}] + c_2), \tag{2.45}$$

$$\begin{aligned}
\hat{v}_r = \frac{i\xi_2 k^2 P_0}{\hat{z}\Psi_2}\Big\{ &(2(1+h)I_1[\Psi_1] - 2\hat{z}I_1[\Gamma\hat{z}])(Y_0[i\Gamma] - Y_0[i\Psi_1]) + \\
&I_0[\Psi_1][\Gamma h(z_e-1)(1+h+\hat{z})Y_0[i\Gamma] - c_3 + 2i\hat{z}Y_1[i\Gamma\hat{z}]] \\
&+ I_0[\Gamma][c_3 - \Gamma h(z_e-1)(1+h+\hat{z})Y_0[i\Psi_1] - 2i\hat{z}Y_1[i\Gamma\hat{z}])]\Big\}
\end{aligned} \tag{2.46}$$

where $I_0[]$ is the zero order modified Bessel function of the first kind, $Y_0[]$ is the zero order Bessel function of the second kind, $I_1[]$ is the first order modified Bessel function of the first kind and $Y_1[]$ is the first order Bessel function of the second kind, $\Gamma = \sqrt{k^2\delta^2 - i\xi_1}$, while $\hat{z} = 1 + hz_e$ and

$$\begin{aligned}
\Psi_1 &= (h+1)\Gamma, \tag{2.47}\\
\Psi_2 &= 2\Gamma\left(\xi_1 + i\delta^2 k^2\right)c_2. \tag{2.48}
\end{aligned}$$

The expressions of coefficients c_0-c_2 are reported in the Appendix B. Once solved the flow field in the SAS, the unknown quantities that characterize the dynamics of the spinal cord can be also found. To this aim, by combining the equations (2.33)-(2.34), and imposing no displacement in the solid matrix at the central canal (eq. 2.43) and the continuity of the tangential stress (2.39), we find

$$\hat{u}_r = \eta_5 \left[\frac{i\hat{v}_x'}{\delta^2 k} + (1-h)\hat{v}_r - \hat{v}_r'\right]_{z_e=0} z_s, \tag{2.49}$$

which provides the radial displacement – linearly dependent on the radial position – once v_x' and v_r' are computed from (2.45) and (2.46). The solutions for the capillary and venous pressures are obtained by solving (2.35) with the use of the boundary conditions (2.40) and (2.43),

$$\hat{p}^{c,v} = \frac{1}{c_4}(I_1[\Psi_3 R_1](c_5 + ic_6^{c,v}Y_0[-i\Psi_3 z_s]) + Y_1[-i\Psi_3 R_i](I_0[\Psi_3 z_s]c_6^{c,v} + c_7), \tag{2.50}$$

with

$$\Psi_3 = \sqrt{\frac{\delta^2(\eta_4 k^2 - i\eta_3)}{\eta_4}}. \tag{2.51}$$

18

The expressions of coefficients c_4-c_7 are reported in Appendix B.

Finally, the kinematic condition (2.41) provides the deformation $\hat{\zeta}$ of the SC-SAS interface

$$\hat{\zeta} = i\frac{Re \cdot \delta\hat{v}_r|_{z_e=0} + \phi\hat{p}^{e\prime}|_{z_s=1}}{\eta_6(\phi - 1)}. \tag{2.52}$$

At last, the above solutions can be used to obtain the CSF pressure from equation (2.35) with the boundary conditions (2.38) and (2.42), but its expression is quite cumbersome so it is reported in the Supplementary Material as a ready-to-use Matlab script.

2.5 Results from the fluid structure interaction model

The present mathematical model simulates the response of the spinal cord-subarachnoid space system under the action of a transient forcing pressure in the form of harmonic propagating wavelets. The main model outcomes are the spatial distribution of the CSF flow field in the SAS, the radial displacement of the porous elastic spinal cord, and CSF and blood pressures within the spinal cord.

Table 2.1: Physiological values of the fluid-structure interaction model parameters.

Quantity	Symbol	Value	Unit
CSF density [74]	ρ	1000	kg /m^3
CSF dynamic viscosity [73], [74]	μ	0.001	Pa·s
CSF network permeability [127]	κ	$1.4 \cdot 10^{-14}$	m^2
Spinal Length	L	0.50	m
External SAS radius [98], [57],[61]	R_d	0.015	m
Internal SAS radius [98], [57], [61]	R	0.01	m
Central canal radius [94]	R_i	$5 \cdot 10^{-4}$	m
Young modulus of the spinal cord [23]	E	$5.4 \cdot 10^5$	Pa
Compressibility of the system	Q	$1.5 \cdot 10^6$	Pa
Biot coefficient [127]	α	0.9	−
Poisson coefficient [127]	ν	0.35	−
Oscillation frequency [49]	ω	2π	1/s
Static csf pressure [67]	$\bar{P}_e$	1350	Pa
Amplitude csf pressure wave in the SAS [72]	P_0	400	Pa
Static capillary pressure [29]	$\bar{P}_c$	3200	Pa
Amplitude of the capillary pressure wave at r=R [112]	P_c	800	Pa
Static venous pressure [133], [95]	$\bar{P}_v$	865	Pa
Amplitude of the venous pressure wave at r=R [133]	P_v	130	Pa
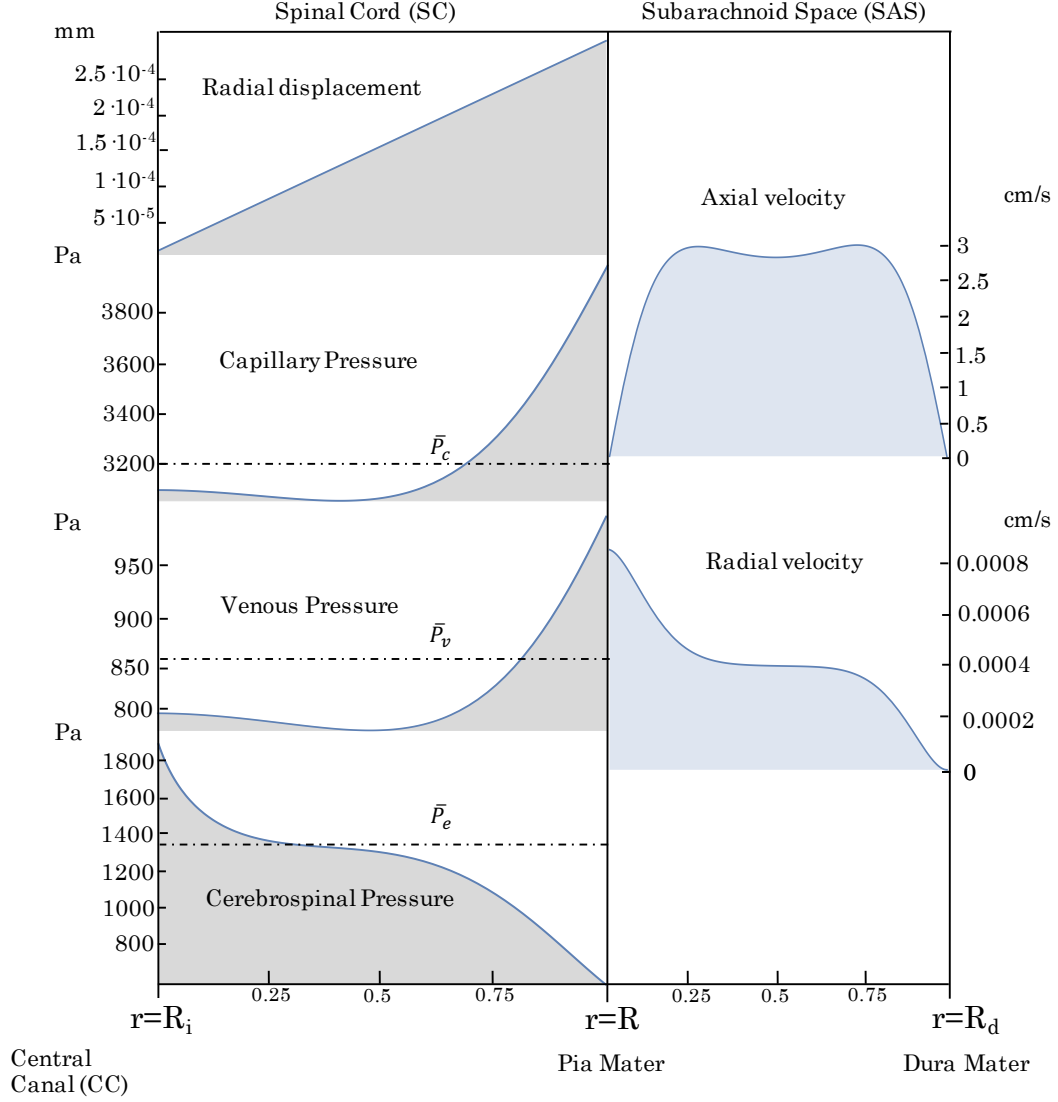
Figure 2.4: Results for the benchmark case. Right: the flow field in the subarachnoid space. Left: the spinal cord displacement and the fluid networks pressures (the dashed lines represent the static component of the pressures).

For simplicity, we will henceforth radially plot the real part of the hatted component of these solutions (see eqs. 2.7 and 2.24), considering different parametric conditions. Notice, that due to the structure of equations (2.7) and (2.24), the complete solutions have to be intended as spatially and temporally harmonic.

Figure 2.4 shows the solutions for the physiological conditions, adopted as benchmark and henceforth referred to with the subscript B (see table 2.1). Due to the pulsatile nature of the CSF flow, a Womersley-like velocity profile is established in the SAS. In addition, the deformability of the spinal cord gives rise to a radial velocity component. According to equation (2.49), we also find a linear dependence on the radial coordinate of the radial displacement in the spinal cord.

Capillary and venous pressures exhibit similar behaviors since the same conditions are imposed at the boundaries: axial symmetry condition at $r=R_i$ – i.e., $\frac{\partial p^{c,v}}{\partial r} = 0$ – and a fixed value of the wave amplitudes at the SC-SAS interface. The latter condition originates from the systemic circulation which feeds the spinal cord.

Obviously, the value of the capillary wave pressure is generally higher than the venous one. Instead, the cerebrospinal pressure has an opposite trend with respect to the blood pressures, in order to guarantee normal stress continuity at the two solid-fluid interfaces.

A sensitivity analysis is described in the following in order to exploit the model response to changes in: i) the pulsatility frequency; ii) SAS anatomy; iii) the Young modulus of the spinal cord; iv) the amplitude of the dynamic component of the venous and capillary pressure at the SAS-SC interface; v) the Biot coefficient; vi) the permeability of the blood networks.

Firstly, figure 2.5 shows the role of SAS anatomy, namely the cavity thickness. An increase in the external radius of the SAS cavity leads to a reshape of the axial [142] and radial velocity profiles, with a loss of flattening for $R_d/R_{dB} < 1$. In the spinal cord, there is an increase in the radial displacement at the SAS-SC interface and decrease in the venous and capillary pressure near the central canal. The CSF pressure increases near the interfaces ($r < 0.25$ and $r > 0.75$), and decreases in the inner core ($0.25 < r < 0.75$).

An increase in the pulsatility of the CSF pressure, namely the temporal frequency ω, is likely related to tachycardia. It leads to a decrease and flattening of the axial Womersley velocity profile [142] and a consequent fall in the radial velocity profile inside the SAS (Figure 2.6), with a moderate decrease of the radial displacement in the SC. It follows that the capillary and venous pressures decrease in the outer zone ($r > 0.5$), whereas they slightly increase in the inner zone. Again, the CSF pressure distribution shows a mirrored behavior.

The influence of the stiffness – the Young modulus E – of the spinal cord is described in figure 2.7. Although the present model considers just a single homogeneous medium, the equivalent stiffness of the overall spinal cord mostly depends on the status of the pia mater. Besides the benchmark case – that may be considered equivalent to a slightly incised pia mater – we account for the case of intact

21
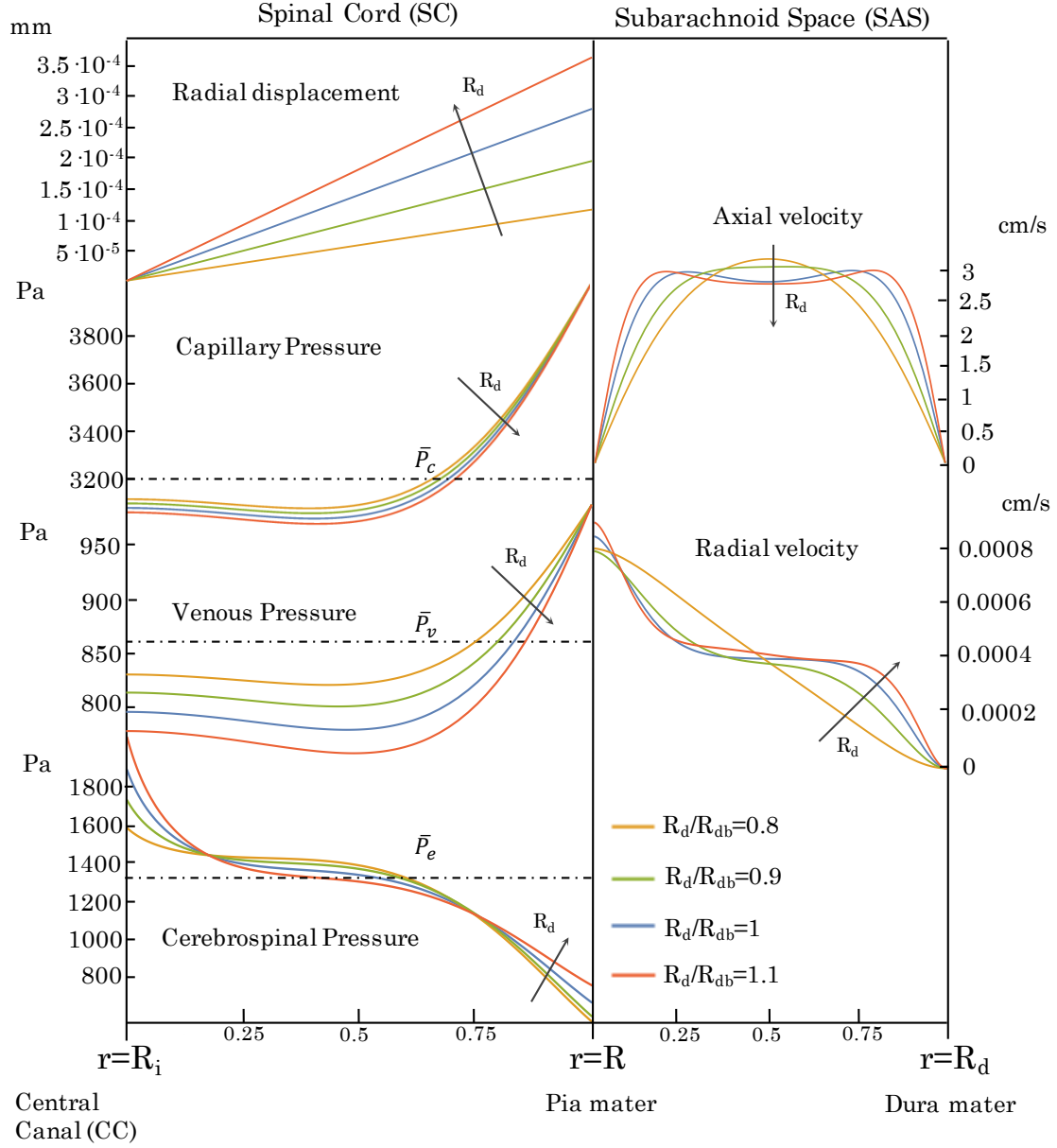
Figure 2.5: Influence of the dura mater radius R_d on the radial profiles of the dynamical quantities. Right: the flow field in the subarachnoid space. Left: the spinal cord displacement and the fluid networks pressures (the dashed lines represent the static component of the pressures)
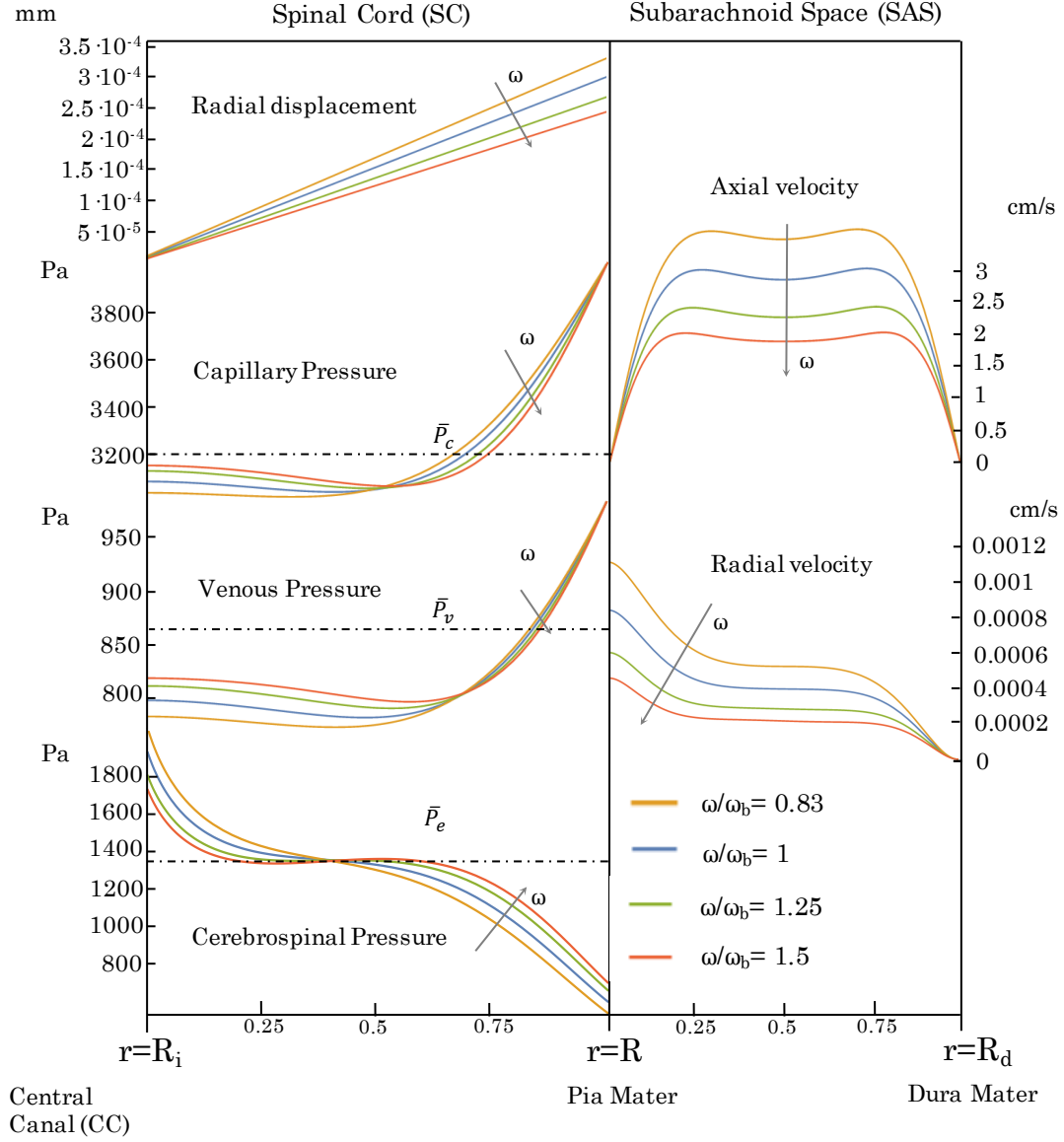
Figure 2.6: Influence of pulsatility ω. Right: the flow field in the subarachnoid space. Left: the spinal cord displacement and the fluid networks pressures (the dashed lines represent the static component of the pressures).

pia mater (E/E_B=2.2 [8]) and highly incised pia mater (E/E_B=0.16 [77]). It is instructive to notice that the SAS flow field is related to the stiffness of the spinal cord through the speed wave c. Due to the propagating waveform of the pressure forcing (eq. 2.6), the pressure gradient – and consequently the flow field – are in fact proportional to the wave number $k = \frac{\omega}{c}$ (see eqs. 2.45 and 2.46). Since it also holds c^2=$E/2\rho(1 + \nu)$ [23], a decrease in the stiffness of the spinal cord induces a decrease in the wave propagation and in turn an increase in the flow field, as it is evident from Fig. 2.7. On the contrary, the radial displacement performs an inverse relationship with the Young modulus in virtue of the linear stress-strain relationship. The fluid networks pressures are influenced by the stiffness of the spinal cord in two respects: on one hand the fluid networks pressures are related to the radial displacement (eq. 2.35) – which depends on the Young Modulus – on other hand they are related to compressibility of the system Q (see eqs. 2.12 and 2.18), where $K_s = E/3(1 - 2\nu)$.

The pressure distributions in the spinal cord are significantly affected by the elastic proprieties of the medium. In particular, CSF pressure performs a quasi-linear profile for the case of intact pia mater (high Young modulus). On the other hand, an highly incised pia mater (small Young modulus) performs a dramatic increase at the CC-SC interface and a decrease near the SC-SAS interface.

Biot coefficient (Figure 2.8) affects the blood pressure inside the SC, but not at the spinal cord-SAS interface. Conversely, CSF pressure is affected at both the solid-fluid interfaces, due to the continuity of the stresses and the Biot extension of Terzaghi principle (see eq. 2.9), creating a distribution characterized by three zones similarly to the response of the SAS anatomy changes.

The influence of the boundary conditions for capillary and venous pressure at the SC-SAS interface on CSF pressure is described in Figure 2.9. Zero pressure at the interface corresponds to the absence of pulsatility in capillary and venous blood. We notice that capillary pressure influences at great extent cerebrospinal pressure at the SC-SAS interface, while the influence of venous pressure is more moderate.

We finally conclude the sensitivity analysis by exploring the response in fluid pressures to a change in the permeability of the blood networks. It is worth noticing that an extensive parametric investigation allowed the permeability of the capillary and venous networks to be esteemed in the brain at values around to 10^{-10} m^2 ([127]). This value is nearly 7000-fold larger than the permeability of the CSF network. To the authors' knowledge, no data on blood permeability are instead available in the spinal cord. We can only presume that it is much lower than the permeability in the brain, because of the differences in morphology and physiology between brain and spinal cord. Following this rationale, all the above results were reported with blood permeability prudently kept equal to the CSF one. Nonetheless, Figure 2.10 investigates the behavior of the fluid pressure within the spinal cord while increasing the blood permeability up to the value found in the brain
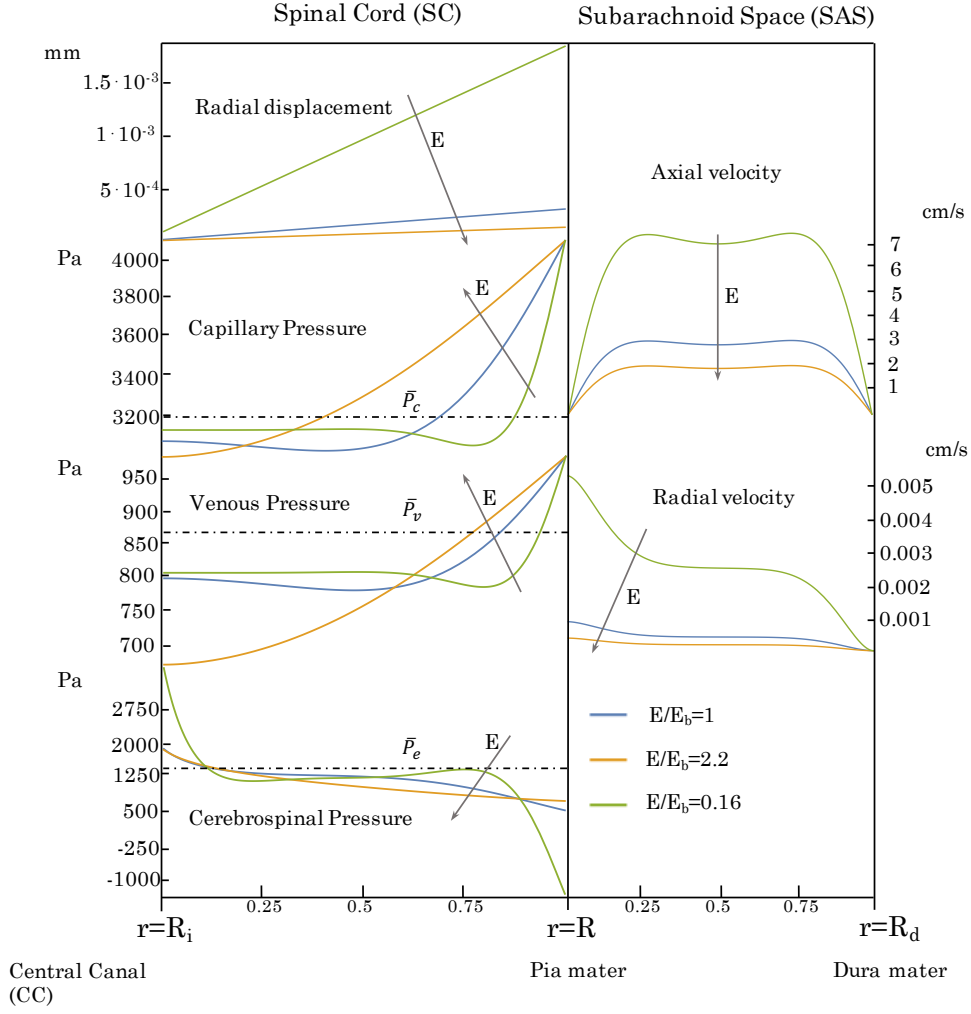
Figure 2.7: Influence of the Young modulus E. Right: the flow field in the subarachnoid space. Left: the spinal cord displacement and the fluid networks pressures (the dashed lines represent the static component of the pressures).
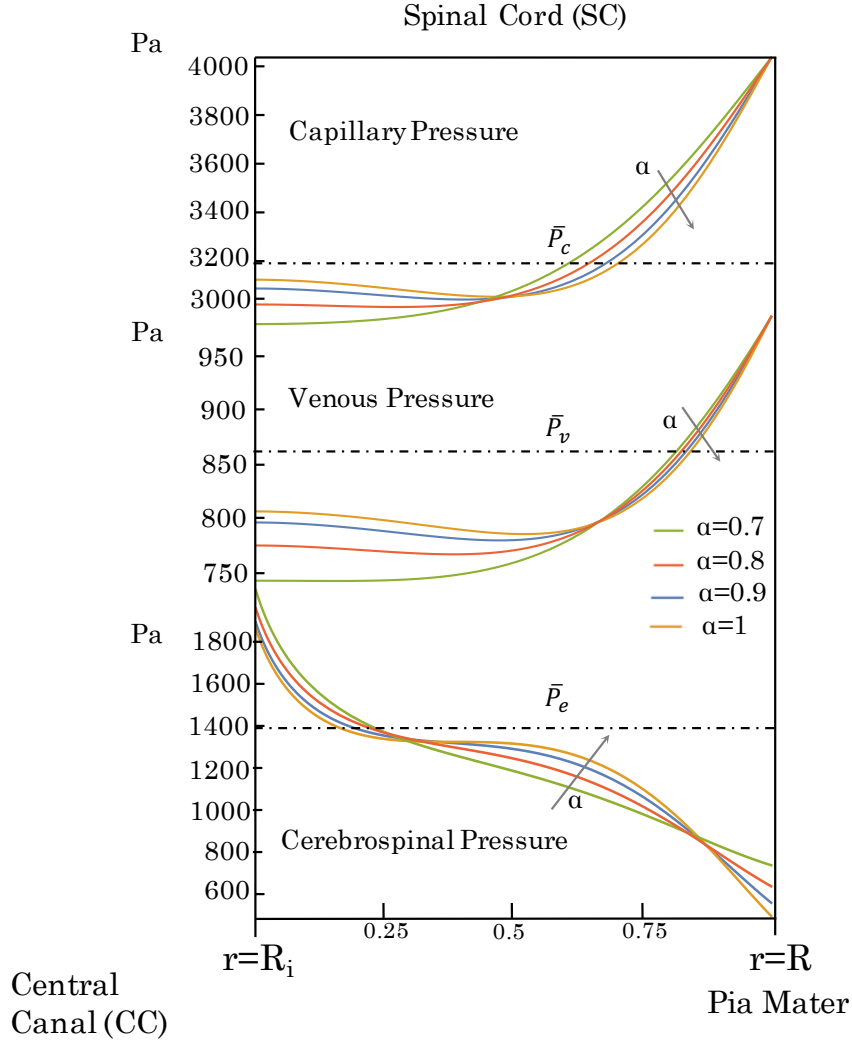
Figure 2.8: Influence of the Biot coefficient α on the pressures in the spinal cord. The dashed lines represent the static component of the pressures.

($\kappa/\kappa_b = 7000$). As long as $\kappa/\kappa_b > 70$, linear radial distributions of the capillary and venous pressures are obtained, in agreement with the results of Tully and Ventikos [127]. More importantly, an increase in the blood permeability induces a fall in the CSF pressure in the inner core of the spinal cord, a feature that might have important repercussions under pathological conditions (see Discussion).
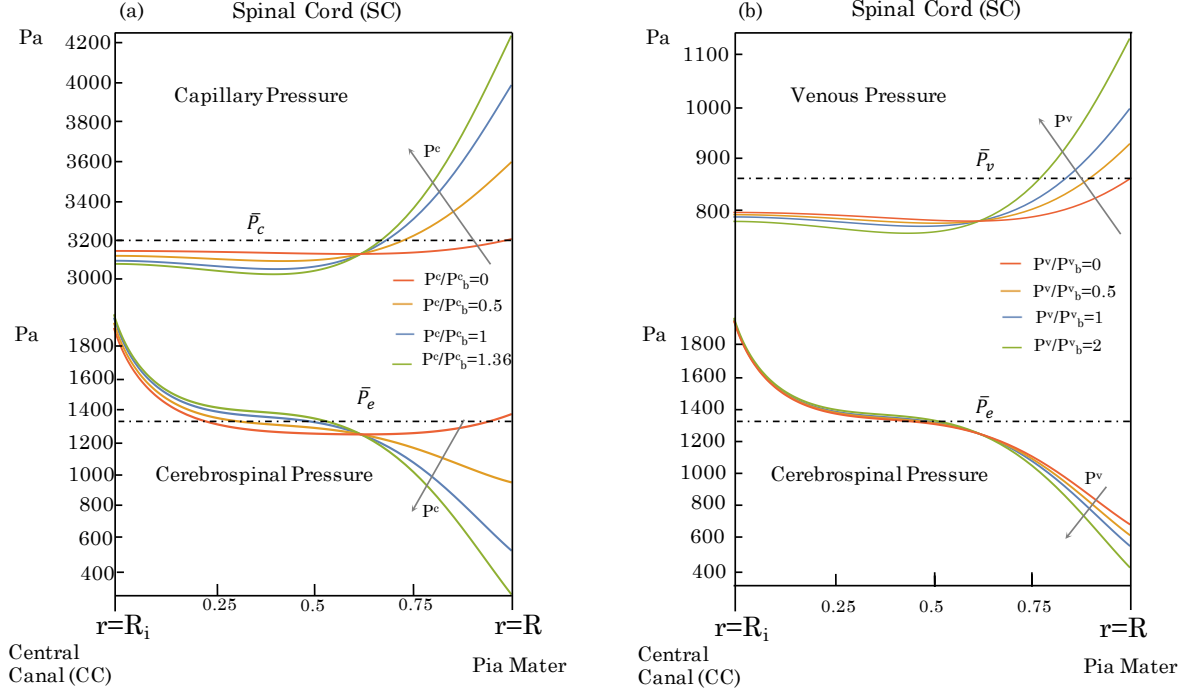
Figure 2.9: Effects of the value of the capillary (a) and venous pressure (b)imposed at the SC-SAS interface on the cerebrospinal pressure. The dashed lines represent the static component of the pressures.

2.5.1 Discussion

The present work provides a new analytical model to study the fluid-structure interactions between the cerebrospinal fluid flowing in the SAS and the spinal cord, under pulsatile conditions. We adopted the multiple network porous-elastic theory to assess the spinal cord displacement and the pressures of the three fluid compartments: capillary blood, venous blood and cerebrospinal fluid. Axial symmetry and a constant value of the Biot coefficient were assumed, while the spinal cord axial displacement and gravity effects were neglected. The Navier-Stokes equations were solved for the fluid cavity surrounding the spinal cord, under an externally imposed pressure waveform and slender-body approximation.

The model allows the flow field, the displacement of the solid matrix, and the fluid network pressures to be solved spatially along the radial position. Similarly to blood flow, the CSF flow in the SAS is parametrized by the Womersley number

27
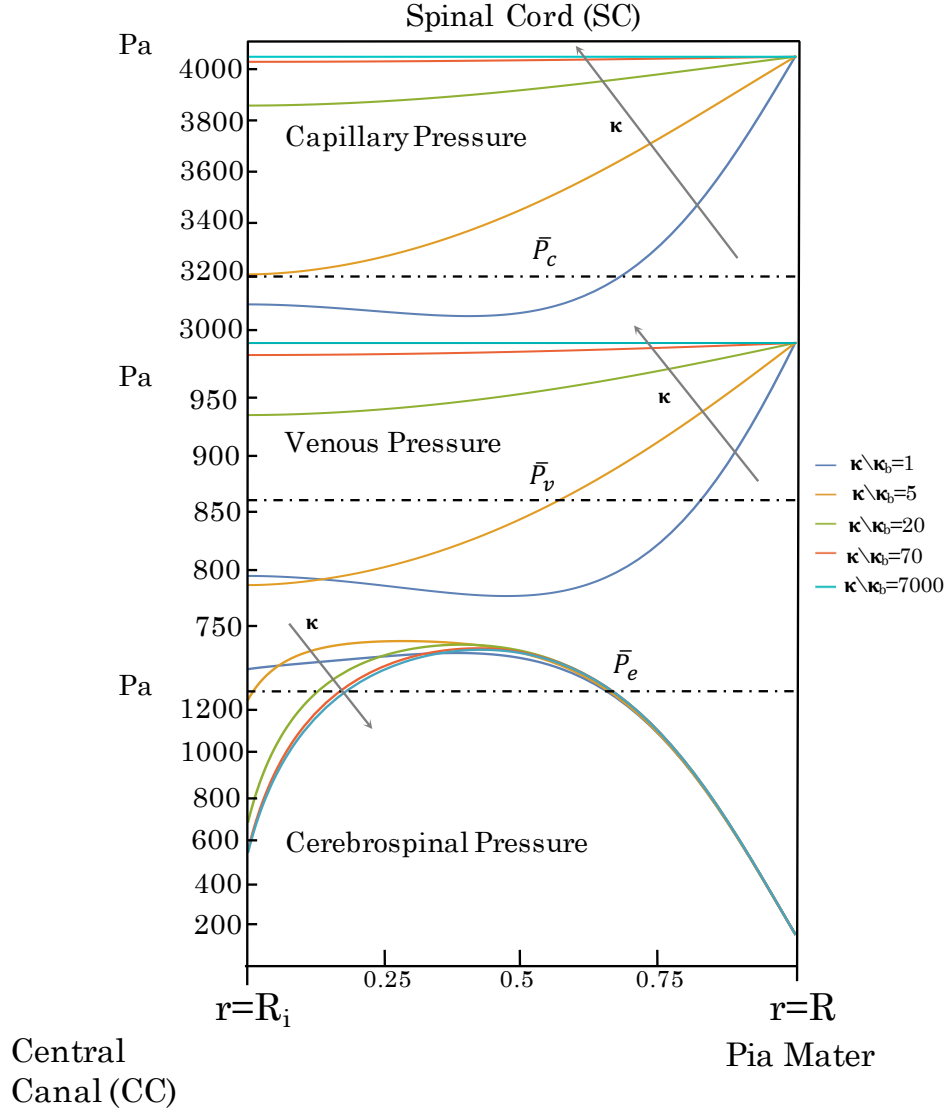
Figure 2.10: Influence of the permeability κ of blood networks on the pressures in the spinal cord. The dashed lines represent the static component of the pressures.

$W = R\sqrt{\omega/\nu} \gg 1$, since the axial velocity is affected by the transient inertial forces, which induces a lag between the velocity and pressure gradient, with the consequent formation of an inviscid plateau in the core of the velocity distribution.

The model prediction on the magnitude of the axial flow velocity is in agreement with several numerical and experimental data previously reported [52], [87], [141], [73], whereas its radial distribution is consistent with the MRI-based numerical simulations performed by Loth, Yardimci, and Alperin [74]. Furthermore, the sensitivity analysis on the external radius of the cavity performed for $W=[4.8-16]$ – see Figure 2.5 – shows that the flow field is again consistent with Loth's results (see cases $W=2.3$ and $W=16$ reported therein).

To the authors' knowledge, the profile of the CSF radial velocity in the SAS has been insufficiently investigated so far. A notable exception is the numerical evaluation reported by Roldan et al. [97], wherein the transverse velocity in the SAS has been numerically estimated to be of order of millimeters per second. Although that work was focused on a patient-specific cranio-vertrebral junction – and it is therefore not comparable with the present analysis – we notice that the present solutions in the benchmark case provide lower values. However, we have showed that an increase in stiffness of the spinal cord – i.e., considering incised pia mater (Fig. 2.7) – induces a substantial rise in the radial velocity.

The reliability of the mathematical solutions and the approximations made in the derivation were tested with the aid of some numerical simulations, where we tackled the same poroelastic problem forced by pulsatile conditions through Comsol Multiphysics 5.4 software. Overall, the percentages of relative error with respect to the theoretical flow field inside the SAS were around 2% and 15%, for the longitudinal and radial components, respectively. It is also worth notice that our numerical simulations confirm the prediction of equation (2.49) for the radial displacement, in agreement with Elliott et al. [30] and our values agree with the results reported by Bertram [7].

An additional outcome of the present mathematical model is the spatial distribution of capillary, venous and CSF pressure inside the spinal cord, which is expected to have a key role in the pathogenesis of syringomyelia [32]. The syrinxes can in fact originate in the spinal cord tissue or from abnormal dilatation of the central canal [40], a pathology also called Hydromyelia. The sensitivity analysis has shown that deviations from the physiological conditions of important parameters can influence at great extent the cerebrospinal fluid pressure inside the spinal cord. In particular, the CSF pressure is substantially affected by: i) the capillary pressure at the SC-SAS interface – a pressure proxy in the SC; ii) the Young modulus – a proxy of pia mater health status –; iii) the permeability of the blood networks. For instance, figure 2.7 shows that injuries in the pia mater (low Young modulus) induce a dramatic decrease in the CSF pressure at the SC-SAS interface. Such a localized depression might pump cerebrospinal fluid from the SAS to the SC, thus inducing syrinx formation. A similar mechanism may be also triggered in the case

29

of a rise in the capillary pressure (see Fig.2.9) and a small static component of the CSF pressure. Other scenarios imply less acute, but important, decrease of the CSF pressure at the SC-SAS interface, such as the decrease of the cardiac frequency, namely bradycardia, or a decrease of the thickness of the SAS, due for instance to a stenosis. Incidentally, this latter aspect provides a model-based justification of the role of Chiari malformation in the occurrence of Syringomyelia.

Likewise, at the CC-SC interface, when considering higher values of blood network permeability a fall in the CSF pressure is seen with a potential consequent dilation of the central canal (fig.2.10).

It is remarkable that, due to linearity of the equations, all the above mentioned effects superimpose in the case of concurrence, altogether giving rise to an inward abnormal CSF pumping, a condition heralding syrinx formation. However, such a conjecture should be scrutinized with a further stability analysis developed around the base state defined by the solution reported in this work.

The mathematical solutions here obtained are quite cumbersome so, in order to enable further developments, a fourth-order polynomial fitting for the same relationships is provided. The polynomial expressions depend on the parameters of the problem and they are evaluated by imposing the passage through the points of the solutions. The excellent overlapping for the benchmark case is reported in Figure 2.11. Furthermore, for the reader's convenience we have also implemented a Matlab ready-to-use script able to provide the solution for the CSF pressure (see the Supplementary Material).

Let us summarize the simplifications adopted in the derivation in favor of the analytical tractability. First, the complexity of the geometry of the spinal cavity was reduced to two simple coaxial tubes and, in order to allow for an evaluation of the flow field in the subarachnoid space, additional fine structures – such as spinal nerve roots, trabeculae, and denticulate ligaments – were neglected. Second, the mass exchange between the fluid networks was assumed negligible, so that the capillary and venous pressures result to be independent from each other. The re-absorption mechanism of the CSF operated by the venous system is therefore not included here. Third, the axial displacement of the spinal cord is disregarded. Indeed, Hentschel et al. [48] and Støverud et al. [118] pointed out that the longitudinal displacement is significant, so it is convenient to further test this latter hypothesis. To this aim, we take into account the axial displacement, and neglect the radial one, while imposing the same boundary conditions as above. So doing, one readily finds a solution with the axial displacement 100-fold lower than the radial one reported above, which reinforces our assumption.

Generally speaking, the present approach has a potential for the investigations of the complex dynamics involving the cerebrospinal fluid in the spinal cord. Despite of its simplicity, this model provides a first step into the direction of analytical modeling of the cerebrospinal fluid-spinal cord interaction. The ultimate purpose is to have a versatile and simple tool capable to shed light on the pathogenesis of
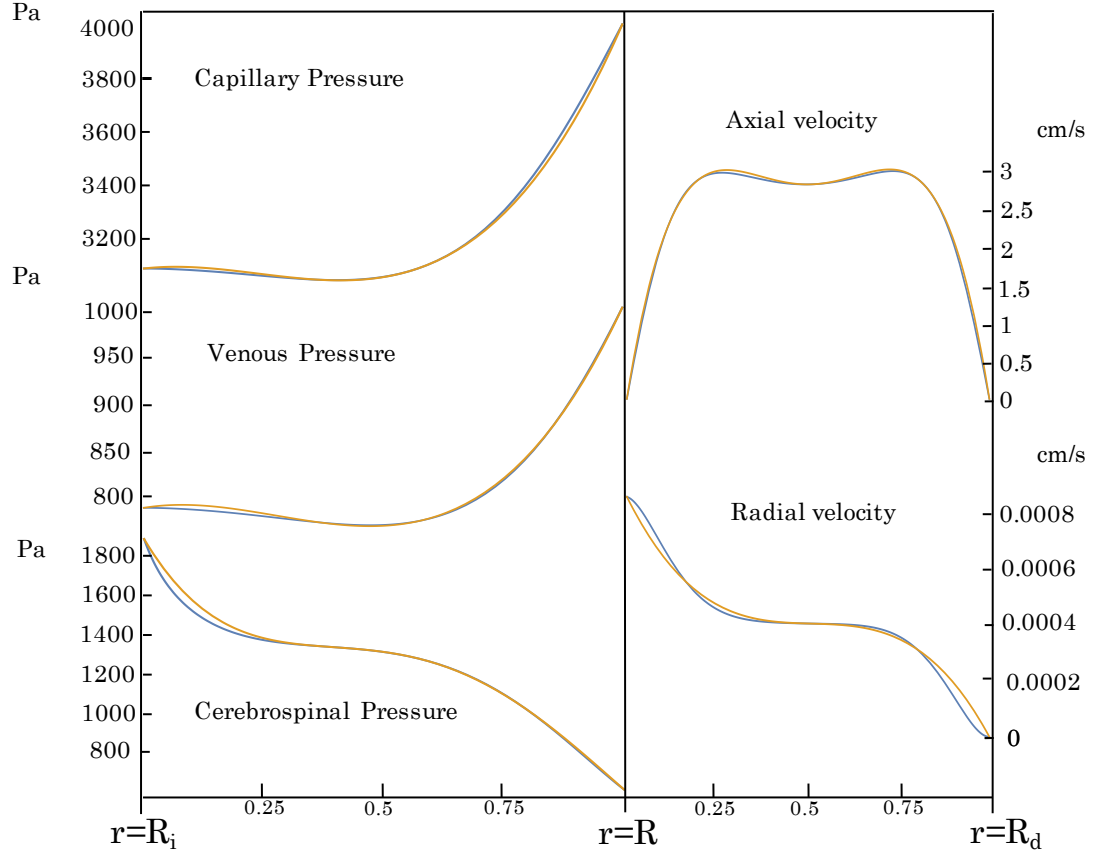
Figure 2.11: Comparison between the original solutions (blue lines) and the fitted polynomial expressions (yellow lines)

neurological diseases underpinned by altered fluid dynamics of the cerebrospinal fluid in the spinal cavity, such as syringomyelia.

Chapter 3

Modeling the interaction of the cerebrospinal fluid pulsatility with intrathecally administrated drugs

Part of the work described in this chapter has been previously published in the journal "Physical Review Fluids" [104] and presented at the XXXVI National Conference of Hydraulics and Hydraulic Construction (IDRA2018).

Intrathecal drug delivery is the administration of medications into the subarachnoid space through injection.

The Intrathecal drug delivery is currently used in clinical practice and it is promising for the treatment of several pathologies of the central nervous system (including some cancers [68] and CSF infection [96]) and for administration of analgesic drugs that cannot be delivered systematically [49]. However, intrathecal delivery protocols and facilities are not optimized yet, since under- or over-dosage may frequently occurs, thus affecting the anticancer effect or inducing nerve damage [131, 17]. Therefore the evaluation of the fluid dynamic processes and the effective diffusivity of these medications urge to be assessed quantitatively.

In this chapter, a numerical model that evaluates time-dependent dispersion coefficient of a drug administrated intratechally is presented. The numerical simulations has the purpose of testing the theoretical hypothesis and results obtained from the analytical model developed by Camporeale and Salerno [104]. They have developed a self-consistent analytical dispersion theory tailored for a drug injection into the spinal subarachnoid space, basing on the Vedel and Bruus [128] formulation.

3.1 Aris-Taylor dispersion

When an inert solute is introduced into a Poiseuille flow, the combined effect of random lateral excursions caused by diffusion and the velocity profile causes an enhanced longitudinal dispersion. If flow regime is pulsatile, differential advection and transversal diffusion combine in order to cause at each cycle a progressive longitudinal spreading of solute having effective diffusivity much larger than the molecular one. More specifically, the initially uniform plug of solute is stretched by shear-flow, so that the particles moving at different speeds increase their relative distance generating concentration gradients in the transverse direction. Such gradients promote transverse diffusion, which dislocates particles from a streamline to another with different speed and concentration. This mixing assures that, during backflow the particle may not return back into its original position, causing at each cycle a net longitudinal spreading. The result of this phenomenon is showed in figure 3.1.
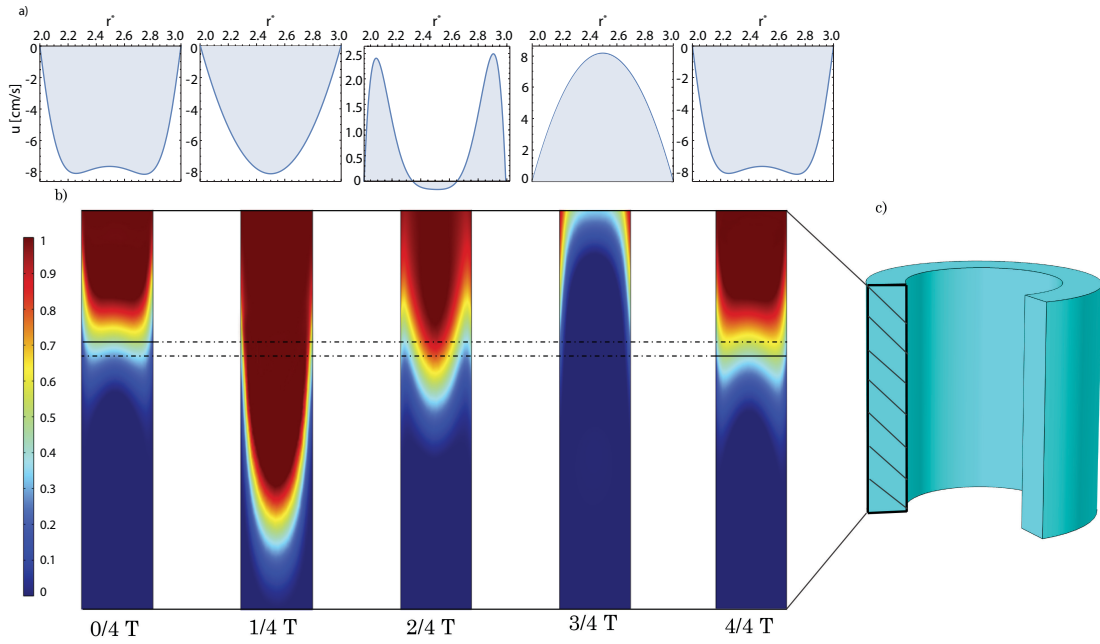
Figure 3.1: Numerical solution of the tracer dispersion in the timespan of a single period. (a) Lateral distribution of CSF velocity in the SAS at five different times. (b) Longitudinal view of the concentration field (the injection point is located at the panel's top). The solid part of the horizontal lines mark the front of the same iso-concentration contour line (c=0.6) at time t and $t+T$, respectively. It is evident the advance of the front. (c) 3D view of the computational domain.

Shear flow-enhanced dispersion was first analyzed by Taylor [123] who provided

a complete description of the asymptotic, cross-sectionally averaged axial concentration distribution under steady flow conditions. The analysis was extended to a wider range of Péclet numbers and geometries by Aris [1] using the method of statistical moments. The Taylor-Aris formulation is limited to the case of steady flows but Watson [134] evaluated the increase of mass rate transfer of a diffusing substance for oscillatory flows in circular pipes. Results were given for a general cross-section in the limiting cases of slow and fast oscillations of the flow. Vedel and Bruus [128, 129] combined the Aris method of moments with Dirac's bra–ket formalism, and obtained a relation for the effective solute diffusivity $D_e(t)$, for given time-dependent laminar flow, in a straight channel of a generic cross-sectional shape.

3.2   Intrathecal drug delivery

Intrathecal delivery is a widely used administration method of analgesic drugs.

The management of pain often involves the administration of a number of analgesic drugs. The most common route is the systemic administration, that is by mouth or by intramuscular, subcutaneous or intravenous injections. The majority of potent analgesic drugs act through the stimulation of cellular receptors that are mostly located in the central nervous system (CNS). Systemic administration allows the drug distribution throughout the body. However, drug diffusion into the CNS is hampered by anatomical and functional obstacles referred to as the blood-brain barrier (BBB). This results in a concentration gradient between the CNS and the plasma, implying that high blood levels must be achieved in order to reach appropriate concentrations in the cerebral spinal fluid. These difficulties can be bypassed by delivering the medication directly in the CSF, i.e. by intrathecal administration [82]. Intrathecal drug delivery (ITDD) has been used since the early 80's and the basic technique of administration has remained the same [113][82].

In intrathecal drug delivery, a catheter is placed close to the spinal cord, and delivers medications directly into the subarachnoid space. It is connected to a subcutaneous pump, that serves as drug reservoir. The continuous injection rate of the pump is usually less than 1 milliliter per day. Some pumps allow patients to self-administer a small bolus injection at the rate of several milliliters per hours during a few minutes [82]. Generally, catheter tip placement is at the level of the spinal cord that innervates the body region comprising the primary pain generator. Once in the CSF, intrathecally delivered medications permeate across the pia-arachnoid and white matter of the spinal cord to access the target dorsal horn receptors and ion channels engaged in nociceptive processing and transmission [111].

Recently, it has been shown that intrathecal delivery is a drug administration method promising for treatment of some cancers [68] and CSF infections [96].

3.3   State of the art

In literature, there are important experimental and computational studies that evaluate the dispersion of a drug in SAS. Hettiarachchi et al.[49] conducted infusion tests with a radio-nucleotide and fluorescent dye under both stagnant and pulsatile flow conditions, inside an experimental surrogate model of the human spinal canal. Nelissen [82] developed a laser scanning setup with which he performed quasi-instantaneous, three dimensional laser-induced fluorescence as well as two dimensional particle image velocimetry (PIV). Hsu et al. [52] proposed a novel method, namely a medical image based computational fluid dynamics, for investigating intrathecal drug delivery. This methodology combines quantitative medical imaging and computational fluid dynamics (CFD) to generate patient-specific computational models. Also Tangen et al. [122] proposed a CFD approach, evaluating flow resistance and drug transport due to spinal microanatomy in cranial and spinal CSF filled compartments that were reconstructed from human imaging data. The role of the spinal microanatomy was investigated numerically also by Stockman [116], [117]. Using the lattice Boltzmann method he numerically evaluate the dispersion enhancement via the fine structure of the SAS and the oscillatory flow of the CSF. Haga et al. [42] investigated the effects of injection parameters on solute distribution within the cervical subarachnoid space, using a Lagrangian approach in a numerical platform. Pizzichelli et al. [92] introduced a numerical model able to simultaneously account for solute transport in the fluid and in the spinal cord, using a Discontinuous Galerkin method and a three-dimensional patient-specific geometry.

Despite these valuable studies, a robust analytical model was still lacking. Professor Carlo Camporeale and Luca Salerno [104] provided a consistent theory for the computation of the time-dependent dispersion coefficient. In order to test the influence of dispersion on the kinematic behavior of velocity waves (driven by pressure waves) and to discuss the validity of theoretical results, a computational model that evaluates time-dependent dispersion coefficient of a drug administrated intratechally was developed.

3.4   Methods: Modeling drug dispersion in the subarachnoid space

The present modeling allows us to evaluate numerically the shear-induced enhanced diffusion coefficient of a drug in the subarachnoid space in the flow direction. Transport of solutes inside SAS is influenced by molecular diffusion, advection associated to the pulsatile CSF flow and the presence of anatomical fine structures within the cavity. However, in order make the treatment more feasible and to be

as close as possible to the analytical model that was wanted to be tested, some assumptions are necessary: i) The anatomical fine structure was neglected; ii) The matrix is assumed rigid, impermeable, isotropic and not influenced by CSF flow– differently from the previous model–; iii) Solute is considered as an inert scalar; iv) Drug absorption is neglected; v) The solute concentration is sufficiently low, therefore it does not influence CSF properties.

The diffusion coefficient in the flow direction was evaluated following the Aris' method of moments.

3.4.1 Aris's method of moments

The drug concentration field $c(x, r, t)$ in the subarachnoid space is driven by a standard advection-diffusion equation. After assuming axial-symmetry and using the scales $\delta_r^* = r_e^* - r_i^*$, L^*, $V^* = V_{max}^*$, c^* and $2\pi/\omega^*$ to non-dimensionalize radial and longitudinal lengths, velocities, concentration and time, respectively (where r_e^* and r_i^* are the external and the internal radius of the subarachnoid cavity, V_{max}^* the maximum value of velocity – evaluated from the dimensional form of Navier-Stokes equation–, c^* is the initial drug concentration and the ω^* is the frequency of the CSF flow oscillation), advection-diffusion equation reads:

$$\frac{\partial c}{\partial t} + Pe \cdot v \frac{\partial c}{\partial x} = \frac{\partial^2 c}{\partial x^2} + \frac{1}{r}\frac{\partial}{\partial r}\left(r\frac{\partial c}{\partial r}\right), \qquad (3.1)$$

where x and r is the (dimensionless) axial and radial coordinate and $v = v(x, r, t)$ is the longitudinal fluid velocity. Henceforth, star refers to non-dimensionless quantities.

The initial and boundary conditions associated to (3.1) are

$$c(x, r, 0) = \tilde{c}(x, r), \qquad (3.2)$$

$$\frac{\partial c}{\partial r} = 0, \quad \text{on } r = r_i \quad \text{and } r = 1, \qquad (3.3)$$

$$\partial_x c \to 0, \text{ for } x \to 0, L \qquad (3.4)$$

where $\tilde{c}$ is the initial concentration field, equation (3.3) sets zero flux at the walls while equation (3.4) sets smoothness of the solution at the upstream and downstream ends of the channel, being L the dimensionless length of the cavity.

Following Aris' method, the enhanced diffusivity coefficient is

$$\frac{D_e^*}{\mathcal{D}} = \frac{1}{2}\frac{d\mu_2}{dt} = \frac{1}{2}\frac{d}{dt}\left(m_2 - m_1^2\right), \qquad (3.5)$$

where $\mathcal{D}$ is the drug molecular diffusion and m_p is the pth full moment of the solute concentration field, namely

$$m_p = \langle 1, c_p(r, t)\rangle = \langle 1, \frac{1}{L}\int_{-L/2}^{L/2} x^p c(r, x, t)dx\rangle, \qquad (3.6)$$

37

c_p is the axial moment of concentration and the bracket notation refers to the internal product defined by

$$\langle f, g \rangle = \frac{2\pi}{a} \int_{r_i}^{r_i+1} r f(r) g(r) dr, \qquad (3.7)$$

where a is the cross section of the annular cavity.

3.4.2 Computational details

The computational model was developed using the finite element software Comsol 5.4. In agreement with the theoretical framework, the computational domain is an annular cavity bounded by two concentric cylindrical surfaces, composed by the upper and the lower part of the SAS, and a thin ring for the injection of the solute in between (see Figure 3.2). In order to reduce computational times, we have
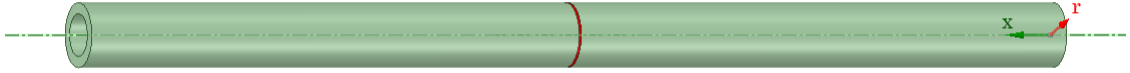
Figure 3.2: Computational domain adopted in the drug dispersion simulations

taken advantage from the azimuthal symmetry, thus considering a two dimensional axisymmetric model. The domain was spatially discretized by 5×10^4 triangular elements, using a fine mesh of the Comsol physics controlled mesh type and three orders of boundary layer elements. The solver resolves continuity equation, Navier Stokes equations and the advection-diffusion equation, computing the flow field and the concentration field in the SAS. The simulations were conducted under unsteady conditions with a time step equal to 0.05 s.

As for the model described in chapter 2, the SAS was excited by transient pressure in order to mimic the pulsatility of the CSF driven by the pulsations of the choroid plexus and the intracranial arteries during the cardiac cycle [104]:

$$\frac{\partial p^*}{\partial x^*} = \Delta^* \exp\left[i\,\omega^* t^*\right] + \text{c.c.}, \qquad (3.8)$$

where Δ^* is the amplitude of the pulse pressure gradient.

The transient pressure gradient, that was imposed in the analytical model (equation (3.8)), numerically was modeled imposing a time-dependent driving pressure at the inlet (cranial end of the domain)

$$P_{inlet} = P_0 \cos(\omega^* t^*), \qquad (3.9)$$

where P_0 is the steady pressure of the CSF within the SAS and in order to numerically emulate the propagation of a wave in a rigid domain, at the outlet boundary (the caudal end), the lagged time-dependent pressure was set

$$P_{outlet} = P_0 \cos(\omega^* t^* - k^* L^*). \tag{3.10}$$

This trick was adopted in order to numerically mimic the effect of gradient oscillation – as it was considered in the theory – without embarking in the numerical simulation of a fluid in a deformable domain. Figure 3.3 reports the pressure field and its z-derivative – the pressure gradient – along the tube at different times, as resolved by the numerical simulation. It is evident that the pressure gradient is practically constant throughout the domain, an aspect that justifies the assumptions of the present theory (namely, eq. (3.8)).
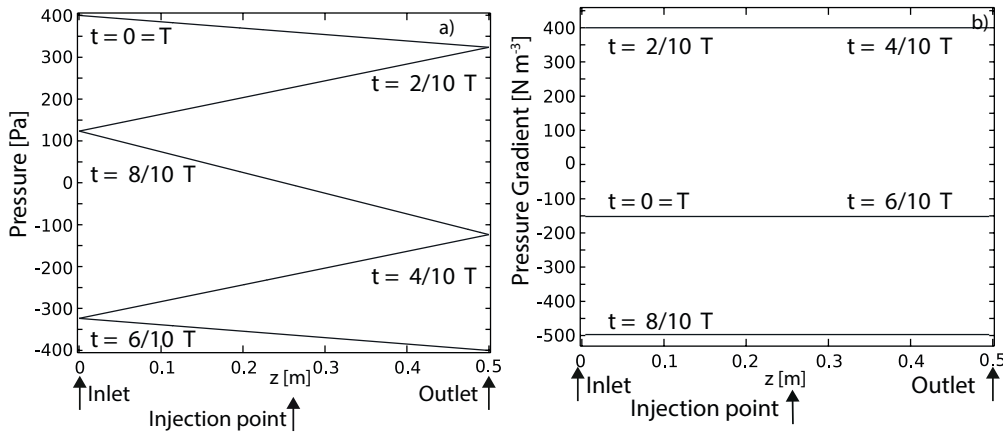
Figure 3.3: Numerical solution for the pressure field (a) and the pressure gradient (b) along the tube, over one time period.

The convection-diffusion equation was solved by considering the injected drug as a passive scalar [42] and the solute concentration was set equal to $\tilde{c}$=1 at the injection site, to mimic a continuous influx of drug. Furthermore, in order to avoid numerical errors, a smoothed step function was also applied to the initial condition for the drug concentration.

At the inlet and outlet boundaries zero concentration flux was imposed in order to mimic no leakage of the drug from the SAS. From a physiological point of view, this choice is justified by the fact that drugs injected in the middle of the spinal cavity generally permeates the pia mater before reaching the cranial or caudal end. Numerically speaking, the simulation would last very long to have solute reaching the edges of the domain. Anyway, to impose a no flux condition does not influence the problem solution. Finally, zero concentration flux and no slip condition were imposed at the walls.

The fluid dynamical problem was discretized with Lagrange P2P1 elements, Lagrange elements with quadratic interpolation for the velocity field and linear interpolation for the pressure field. To avoid excessive computational times, Comsol default linear elements were used for the convection-diffusion problem.

COMSOL Multiphysics bases on the finite element method (FEM). When solving solid mechanics applications or transport phenomena driven by diffusion, the approach is straight-forward. However, for convection-dominated transport problems, it is known that the approach can lead to numerical instabilities, namely, oscillations in the solution [107]. Thus, the Galerkin method used by Comsol to discretize the equations may become unstable for Pèclet number referred to single mesh element (Pe_{el}) larger than one, i.e., $Pe_{el} = uh/2\mathcal{D} > 1$ with h being the mesh element size. Since the present problem is convection-dominated ($Pe_{el} \gg 1$), stabilization techniques have been employed. In Comsol, all transport interfaces, such as heat transfer, fluid flow, or species transport, automatically use consistent stabilization methods, consisting of adding an artificial diffusion in the streamline direction and/or in the crosswind direction. It was decided to also consider isotropic diffusion, an inconsistent method, implemented in Comsol, that add to the physical diffusion coefficient, an artificial isotropic diffusion coefficient, defined as:

$$D_{art} = \delta h u, \tag{3.11}$$

where δ is a tuning parameter, by which the amount of artificial diffusion can be adjusted. In our simulations the Comsol default value $\delta = 0.25$ was set.

From the numerical solution of the concentration field, we spatially integrated the concentration fields at each time steps and computed $M_1(t)$, dM_1/dt and dM_2/dt. According to (3.5), we finally get the value of $D_e(t)$.

Table 3.1: Physiological values of the drug dispersion model parameters.

Quantity	Symbol	Value	Unit
CSF density [73, 74]	ρ	1050	$[kg/m^3]$
CSF dynamic viscosity [73, 74]	μ	0.001	$[Pa\,s]$
Drug molecular diffusivity	$\mathcal{D}$	2.1×10^{-10}	$[m^2/s]$
Spinal Length	L^*	0.50	$[m]$
External SAS radius [98, 57, 61]	r_e^*	0.015	$[m]$
Internal SAS radius [98, 57, 61]	r_i^*	0.01	$[m]$
Amplitude pressure wave [72]	P_0	400	$[Pa]$
Oscillation frequency [49]	ω	2π	$[1/s]$
Womersley number	W	12	
Pèclet number	$P\grave{e}$	$1.7 \cdot 10^6$	

3.5   Results from the drug dispersion model

The results obtained from the computational model were compared with those obtained from the theoretical model developed by Salerno and Camporeale (see [104]). Figure 3.1 shows how the tracer profile reflects the velocity profile at different times during the timespan of a single period T. The two horizontal lines refer to the advance of the front position of the same concentration contour line after a single period.

Furthermore, a sensitive analysis is here conducted in order to investigate the impact of the SAS anatomy, the frequency of pulsatility and the forcing pressure on the effective diffusivity. In particular, values of diffusivity in the transient regime are compared. The physiological values of the parameters are chosen as a benchmark case [49, 52, 58, 122], referred to with subscript B in the sequel. Details of the different scenarios are reported in Table 3.2, while Table 3.1 summarizes the physiological values that have been considered as the benchmark case.

Table 3.2: Summary of the different runs for the sensitivity analysis of the drug dispersion model.

Test case	R_e [m]	ω^* [1/s]	L [m]
Benchmark	0.015	2π (60 *bpm*)	5
$S_{l,1}$	0.015	2π	3
$S_{l,2}$	0.015	2π	8
$S_{l,3}$	0.015	2π	10
$S_{R,1}$	0.0120	2π	5
$S_{R,2}$	0.0135	2π	5
$S_{R,3}$	0.0165	2π	5
$S_{\omega,1}$	0.015	$11/6\,\pi$ (55 *bpm*)	5
$S_{\omega,2}$	0.015	$14/6\,\pi$ (70 *bpm*)	5
$S_{\omega,3}$	0.015	$16/6\,\pi$ (80 *bpm*)	5

Fig. 3.4a shows that D_e has a moderate decrease when the external radius of the cavity is increased (scenarios $S_{R,1-3}$). This is mainly due to a decrease in the peak velocity with a wider inertial plateau (see Fig.2.5 in the previous chapter) and to the consequent reduction of the shear in the velocity profile.

The change in the pulse pressure affects the magnitude of dispersion at a great extent (see Fig. 3.4b). For instance, a 50% reduction of Δ^* causes a fourfold decreases in D_e. Although the meninges are here assumed undeformable and x-dependency of the flow field solution has been neglected, it is instructive to relate the amplitude of the pulse pressure gradient Δ^* to the features of real CSF flow measured in humans. Such flows are kinematic waves that normally propagates with celerity $c_w^* \sim$ 5-15 m/s. Basically, this celerity is related to the wavelength l^*
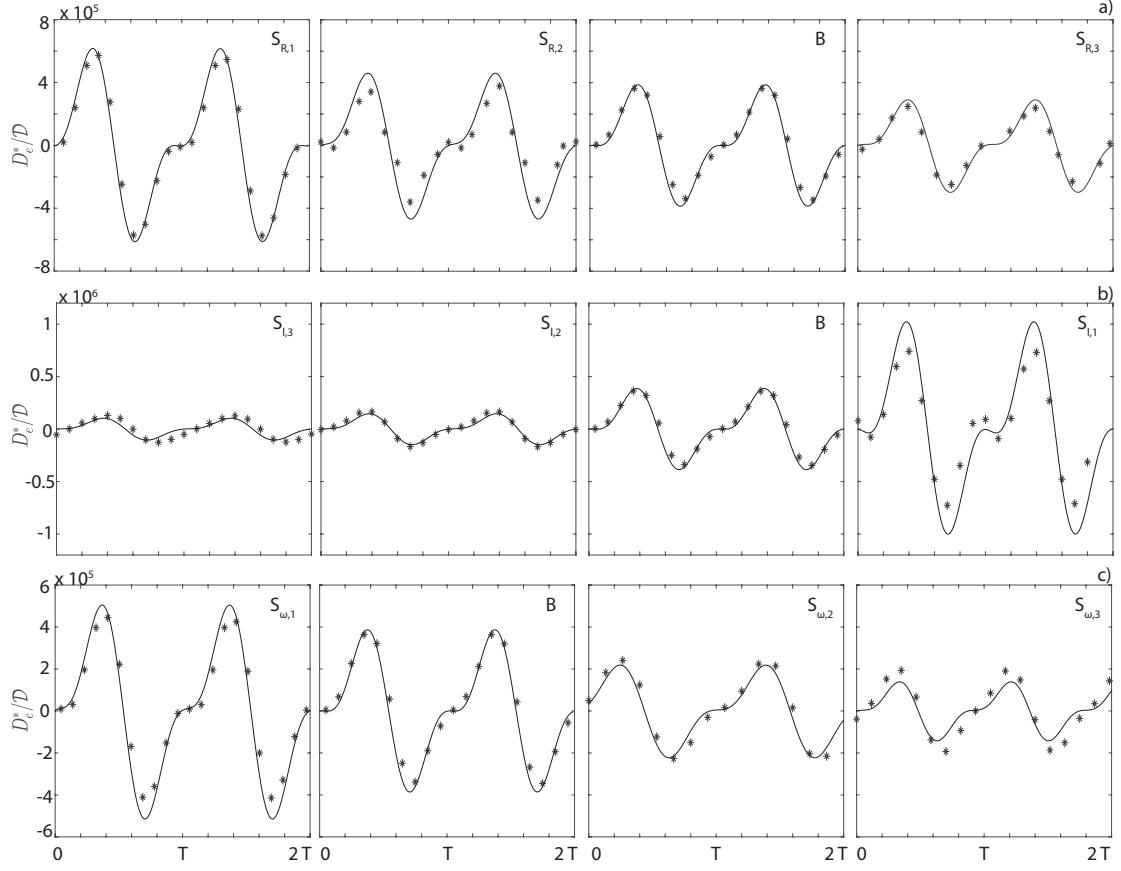
Figure 3.4: Influence of external radius ($S_{R,1-3}$), gradient amplitude ($S_{l,1-3}$) and frequency ($S_{\omega,1-3}$) on the effective dimensionless diffusivity. Letter B refers to the values of the benchmark case. Solid lines refer to the analytical results and stars refer to the numerical results. Notice the different scaling among the rows of panels.

and the frequency according to $c_w^* = \omega^* l^* / 2\pi$. Since Δ^* is the product of the pulse pressure amplitude and the spatial wavenumber k^*, an increase in Δ^* is numerically equivalent to a decrease in the wavelength $l^* = 2\pi / k^*$. It is also worth reminding that the Moens-Korteweg equation states that phase celerity (called pulse wave velocity by physicians) is proportional to the root square of the wall elastic module [84]. This means that, since the frequency is externally imposed by the heart rate, a variation in Δ^* can be also considered equivalent to different wall rigidities, although the present model does not account for this aspect explicitly. This aspect provides an additional interpretation of sensitivity analysis on Δ^*. It is in fact reasonable to suppose that more flexible boundariers may damp dispersion of solute within the SAS.

Since there is a strong correlation between heart rate and CSF pulsation, an increase (decrease) in ω allows us to understand how the effective diffusivity is

affected by tachycardic (brachycardic) patients ($S_{\omega,1-3}$). A low value of ω (i.e., small Womersely number W) implies a well-developed velocity profile, and an increase in the shear-induced dispersion [128]. Instead, if the flow varies too rapidly (high W) the velocity profile development is hindered and the peak velocity is reduced (see Fig.2.6 in the previous chapter), so the shear is dampened and the dispersion of solute decreases.

We emphasize that, for all tests the numerical results are in good agreement with the analytical predictions, even though the former are usually slightly higher than the latter. Both numerical and analytical results are characterized by a transitory phase, with the presence of a single frequency equal to ω^*, which gradually switches to a second harmonic ($2\omega^*$) at long times.

Discussion

This work provides a modeling approach for the evaluation of dispersion of a passive scalar within an annular cavity under pulsatile conditions. The results have potential relevance for drug dispersion due to intrathecal injection in the cerebrospinal fluid of the subarachnoid space.

The results have shown that pulsatility can affect the timing of drug release in a relevant way through the mechanism of shear dispersion. Due to the high value of the Womersley number ($W \sim 12$), the velocity profile of CSF in the cavity is in fact highly influenced by transient inertial forces, which cause a lag between velocity and pressure gradient and, consequently, a relatively flat distribution in the core. The characteristic time of drug dispersion, T_d, from the injection point ($z^*=0$) to the cranial end ($z^*=L^*/2$) is around $L^{*2}/4\overline{D_e^*}$ (where $\overline{D_e^*}$ is the average effective diffusivity over an oscillation period), that is dramatically lower than the sole action of molecular diffusivity ($L^{*2}/4\mathcal{D} \sim 10^4$ h) if the fluid were considered at rest, or than the pure steady flow advection (~ 4 h) if pulsatility were neglected. It is worth emphasizing that, T_d is highly dependent on the drug molecular diffusivity $\mathcal{D}$ and for intrathecal drugs the molecular diffusivity usually ranges between $\mathcal{D}=10^{-9}-10^{-11}$ 10^{-9} – Bupivacaine [82] and 10^{-11} m^2/s–Baclofen [45] [64]–.

Salerno et al. [104] have investigated the role of the porosity in the SAS, due to the presence of fine structure (trabeculae and ligaments). Although the porosity is very close to unity ($\phi \sim 0.99$), the presence of ligament strands in the cavity plays a key role in further reducing T_d with respect to the non-porous case and in weakening its dependence on the solute characteristics. Specifically, the presence of fine structures considerably reduces the dependence of the effective diffusivity on $\mathcal{D}$ and decreases the timing of dispersion (with a remarkable value of $T_d \sim 5$ min for spanning a distance of 1 mm).

The sensitivity analysis showed that some features of the pressure wave, such as Δ and ω play a key role that should be carefully monitored during intrathecal treatments. In fact, tachycardic conditions (high values of ω) or low CSF pulse

pressure gradients could delay the drug delivery and the achievement of site target of therapies. In the sensitivity analysis, mutual influence between ω and Δ was neglected, while under physiological conditions when the heart rate rises up, the total blood volume inflated and deflated in each cardiac cycle changes accordingly, so influencing the CSF pressure wave as well. On the contrary, the role of geometric parameters - such as r_i - is moderate, so the approximation of a constant cross section seems quite reasonable.

Since the theoretical model does not account for a finite domain, it develops transient regime that is much longer than the value predicted by the numerical simulations. Nevertheless, the behavior performed by the theory is in excellent agreement with the numerical simulations.

In the theoretical model developed by the Professor Carlo Camporeale and Luca Salerno, the role of the fine structure (such as nerve roots and trabeculae) on the intrathecal drug dispersion was investigated in detail. However, it was decided to test the latter model with the present numerical analysis only for the non-porous case. Thus this computational model does not include fine structures present in the subarachnoid space.

Another limitation of this approach is to consider a solute uniformly-distributed over the annular cross section at the initial time. This assumption might be considered unrealistic with respect to clinical intrathecal injections where the catheter induces non-uniformity in the initial distribution.

Furthermore, a recent study by Lawrence et al. [65] showed that spine eccentricity and its variation with axial position may induce the onset of non linear phenomenon that lead to steady streaming which influences drug dispersion, becoming the convective transport more important than shear-enhanced Taylor dispersion. But the eccentricity role is not considered in this study.

In this study, an over-simplified representation of meninges surface was deliberately used. In particular, the wall roughness was neglected. A chaotic flow triggered by the pulsatile condition [21] [86] along with the presence of ridges on the meninges surface might generate mixing phenomena, as pointed out by [119]. However, the quantification of the morphological irregularity of SAS walls requires 3D subject-specific SAS models taylored on detailed MRI imaging [106]. The comparison between a numerical modeling of high-resoluted SAS conformation and the theoretical results to investigate the role of wall roughness is therefore left to successive analyses.

To sum up, a computational model able to assess longitudinal dispersion in an annular cavity with pulsatile flow is here provided and discussed. The model has the potential to give a rapid and accurate assessment of the effective diffusivity of drugs for intrathecal therapies, highlighting the key role of CSF pulsations. Moreover, it has allowed us to identify the frequency of oscillation and the wavelength of wave pressure as the key physiological parameters of the dispersion phenomenon.

Chapter 4

Modeling thrombus formation in the cardiovascular system

Part of the work described in this chapter was presented at the XLVI Annual European Society for Artificial Organs Congress and at the 8th Biennal European Cell Mechanics Meeting.

Cardiovascular diseases (CVDs) are a group of disorders of the heart and blood vessels that constitute the leading cause of death worldwide [28]. Among CVDs, thrombosis has a significant role. Thrombosis refers to the formation of a blood clot, known as a thrombus, inside a blood vessel, obstructing the flow through the circulatory system. Thrombosis and thromboembolism remain significant sources of morbidity and mortality in cardiovascular device patients. Most implantable cardiovascular devices, such as prosthetic heart valves, endovascular stents, synthetic vascular grafts, and ventricular-assist devices, have been shown to induce thrombotic deposition [114]. The availability of a mathematical model capable of reliably predicting regions of platelet activation and deposition within a cardiovascular device would constitute a powerful tool for optimizing the design of the device flow path after appropriately considering the thrombogenicity of the blood-contacting materials and the status of the patient's hemostatic system. The aim of the current chapter is to describe the development of a numerical model, using the commercial finite element solver COMSOL Multiphysics, of platelets aggregation and thrombus formation, in order to create a tool that can help in studying possible thrombotic deposition zones inside cardiovascular devices and in general in case of flow disturbance in arteries. A comprehensive model of platelet-mediated thrombogenesis has been developed. The model includes the following critical processes: i) platelet activation induced by both chemical agonists generated at sites of vascular injury and high shear stress; ii) kinetics and mechanics of platelet-platelet and platelet-surface adhesion; iiii) platelet aggregation induced by localized shear deceleration; iv) alterations in local fluid dynamics due to the presence of a thrombus; v) platelet recirculation; and vi) platelet production by megakaryocytes.

It has long been assumed that platelet aggregation and thrombus growth are initiated by soluble agonists generated at sites of vascular injury, but recently Nesbitt et al. [83] have shown that platelet plug formation is also driven by spatial shear gradients. To our knowledge, for the first time, the proposed computational model implements and investigates the role of spatial shear gradients in the formation and evolution of a thrombus. This aspect is clinically very relevant because shear gradients, that occur in case of blood flow disturbance, are generally related to many pathological situation –i.e. stenosis, the presence of cardiovascular devices, atherosclerotic plaque, thrombus itself–.

4.1   Blood

Blood is a constantly circulating fluid providing the body with nutrition, oxygen, and waste removal.

Whole blood is a two-phase liquid composed of cellular elements suspended in plasma, an aqueous solution containing organic molecules, proteins, and salts. The cellular phase of blood includes red blood cells [RBCs], white blood cells [WBCs], and platelets [3], see Fig. 4.1.

White blood cells and platelets can affect blood rheology, but under normal conditions, red blood cells have the largest influence. Blood rheological properties are determined by the physical properties of its two phases and their relative contributions to total blood volume [81].

Blood is a non-Newtonian, shear thinning fluid with thixotropic and viscoelastic properties. Usually blood viscosity values range between 3.5 and 5.5 cP. However, blood viscosity cannot be summarized by a single value. Due to the shear thinning property of blood, the viscosity of this fluid changes depending on the hemodynamic conditions. This means that blood viscosity is different in the large arteries, the veins, and the microcirculation, where shear rates can vary from a few s^{-1} to more than 1000 s^{-1}. Blood viscosity depends on: hematocrit, the volumetric concentration of red blood cells, plasma viscosity, the ability of RBCs to deform under flow, and RBC aggregation-disaggregation properties [81].

Despite its non-Newtonian nature, it has been shown that blood follows Newtonian behavior when the shear rate exceeds 100 s^{-1} [90]. Thus, considering blood as a Newtonian fluid is generally a valid assumption in arteries.

4.1.1   Plasma

Plasma is the liquid portion of blood. It serves as a transport medium for delivering nutrients to the cells of the various organs of the body and for transporting waste products derived from cellular metabolism to the kidneys, liver, and lungs for excretion. Plasma is also a transport system for blood cells, and it plays a critical
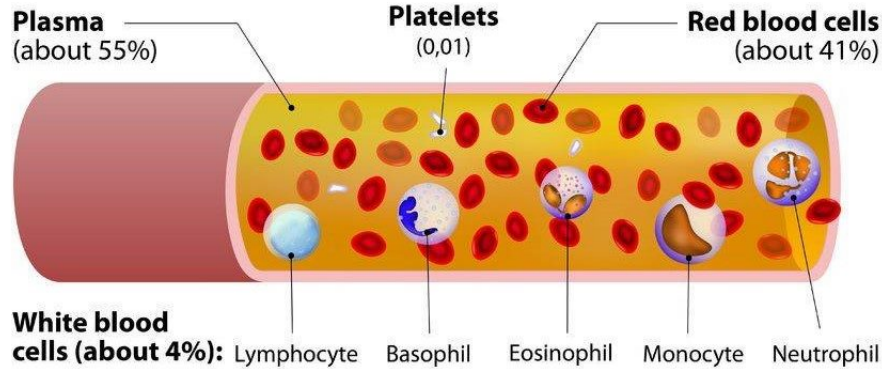
Figure 4.1: Blood composition (image taken from [89])

role in maintaining normal blood pressure. Finally, plasma helps to distribute heat throughout the body and to maintain homeostasis, or biological stability, including acid-base balance in the blood and body.

Plasma is a complex solution containing more than 90 percent water. The water of plasma is freely exchangeable with that of body cells and other extracellular fluids and is available to maintain the normal state of hydration of all tissues [139].

The major solute in plasma is a heterogeneous group of proteins constituting about 7 percent of the plasma by weight [109]. One critical group is the coagulation proteins and their inhibitors; fibrinogen circulating in the blood is converted to fibrin, which in turn helps to form a stable blood clot at the site of vascular disruption. Conversely, coagulation inhibitor proteins help to prevent abnormal coagulation (hypercoagulability) and to resolve clots after they are formed. When plasma is allowed to clot, fibrinogen converts to fibrin, trapping the cellular elements of blood. The resulting liquid, devoid of cells and fibrinogen, is called serum. Biochemical testing of plasma and serum is an important part of modern clinical diagnosis and treatment monitoring. High or low concentrations of glucose in the plasma or serum help to confirm serious disorders such as diabetes mellitus and hypoglycemia [139].

4.1.2 Blood cells

Red blood cells

The most prevalent particles suspended in blood plasma are red blood cells (RBCs), also called erythrocytes, which transport oxygen in the arterial circulation and carbon dioxide in the venous side. RBCs are composed of water (around 65 % by weight), haemoglobin (around 32 % by weight) with a small presence of

47

inorganic substances such as potassium, sodium, magnesium and calcium. Considering that normal values of hematocrit are around 40-45 %, it is not surprising that RBCs significantly affect the viscosity of whole blood. More specifically, there is an approximately 4% increase of blood viscosity per unit increase in hematocrit. RBCs are characterized by a biconcave disk shape with a diameter of around 7 μm and a volume of around 1 μm^3. This particular shape provides great flexibility, allowing passage through vessels with diameters much smaller than the RBC undeformed dimension [41]. RBCs have historically been considered passive bystanders in thrombosis. However, clinical and epidemiological studies have associated quantitative and qualitative abnormalities in RBCs, including altered hematocrit, sickle cell disease, thalassemia, hemolytic anemias, and malaria, with both arterial and venous thrombosis [18].

White blood cells

White blood cells, also called leukocytes, are particles of different sizes that occupy a small volume of the blood. White blood cells play a vital role, protecting the body from infectious processes either through physical removal of microorganisms or by the production of antibodies. White blood cells have a negligible effect on blood viscosity in large vessels, although they can play a role in very small conduits [41]. White blood cells have historically been considered passive in thrombosis. However, in recent years, it has been shown [120] that leukocytes can be induced to express tissue factor and release procoagulant molecules. These mediators can influence several aspects of thrombus formation, including platelet activation and adhesion as well as activation of the intrinsic and extrinsic coagulation pathways.

Platelets

Platelets, or thrombocytes, are the smallest particles in blood (2-3 micrometers). They are the real protagonists of hemostasis, the process of stopping bleeding through a damaged blood vessel by creating a blood clot or thrombus. When the endothelial surface of a blood vessel is injured, platelets immediately attach to the injured surface and to each other in large numbers, forming a tenaciously adherent mass of platelets. When seen in fresh blood, platelets appear spheroid, but, in the case of vessel injuries, they have a tendency to extrude hairlike filaments from their membranes and adhere to each other. They synthesize and release in tiny granules the agonists, clot-promoting substances that enable the recruitment of other platelets. Platelets are formed in the bone marrow by segmentation of the cytoplasm of cells known as megakaryocytes, the largest cells of the marrow. Within the marrow, the abundant granular cytoplasm of the megakaryocyte divides into many small segments that break off and are released as platelets into the circulating blood [109] (see figure 4.2). After about 10 days in the circulation, platelets are
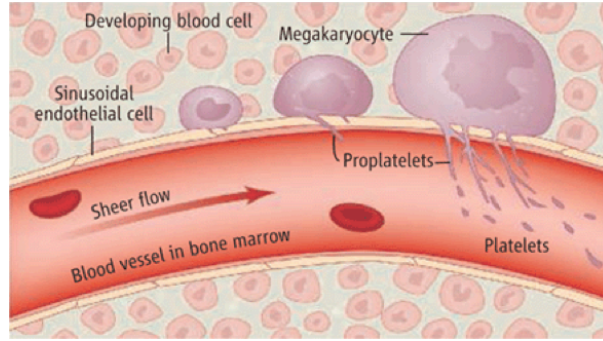
Figure 4.2: Platelet formation by segmentation of megakaryocytes (image taken from [37])

removed and destroyed [101].

4.2   Thrombus formation

Hemostasis (thrombus formation) is the normal physiological response that prevents significant blood loss after vascular injury [140]. According to Virchow's triad, there are three possible contributors to excessive and undesirable formation of clots (i.e. thrombosis): vessel wall injury or inflammation, changes in the intrinsic properties of blood, and changes in blood flow velocity [108]. The process of clot formation and growth at a site on a blood vessel wall involves a number of simultaneous processes including: multiple chemical reactions in the coagulation cascade, species transport, and platelet adhesion, all of which are strongly influenced by the hemodynamic forces [140]. There are two main components of hemostasis: primary hemostasis and secondary hemostasis. Primary hemostasis refers to platelet aggregation and platelet plug formation. Secondary hemostasis refers to the deposition of insoluble fibrin, which is generated by the coagulation cascade. These two processes occur simultaneously and are mechanistically intertwined. Thrombosis can occur whenever this process is dis-regulated [36].

4.2.1   Primary hemostasis

Primary hemostasis initiates immediately after vessel injury. The main consequence of this process is the creation of a platelet plug. There are two crucial steps in the process of primary hemostasis: platelet activation and platelet aggregation. Figure 4.3 provides a chart that summarizes the processes that lead to platelet plug formation.

49

Platelet activation

When endothelial damage occurs, platelets come into contact with exposed collagen and von Willebrand factor and thus start adhering to the damaged surface and becoming activated. Activated platelets change in shape and pseudopods form on their surface, assuming a star-like appearance, greatly increasing their adhesive properties. Indeed, only activated platelets are able to bind to other platelets. Platelet activation can be induced by chemical and/or mechanical factors. Chemical platelet activation is induced by chemical agonists such as thrombin, the adenine nucleotide ADP, and thromboxane TxA2.

The agonists are synthesized and released in dense granules by activated platelets themselves in order to enable the recruitment of other activated platelets. On the other hand, it has been shown [47],[16],[62] that platelets can also be activated by large mechanical stresses, in particular by high shear stress. In humans, physiologic mean shear stress levels in the arterial circuit reach 20 to 30 dyne/cm^2 (shear rates of whole blood are in the range of 500 to 750 s^{-1}). Pathologic levels, which can occur in a stenosed artery or in a cardiovascular device, may reach >350 dyne/cm^2 (shear rate larger than 9000 s^{-1}), and they are associated with platelet activation [62].
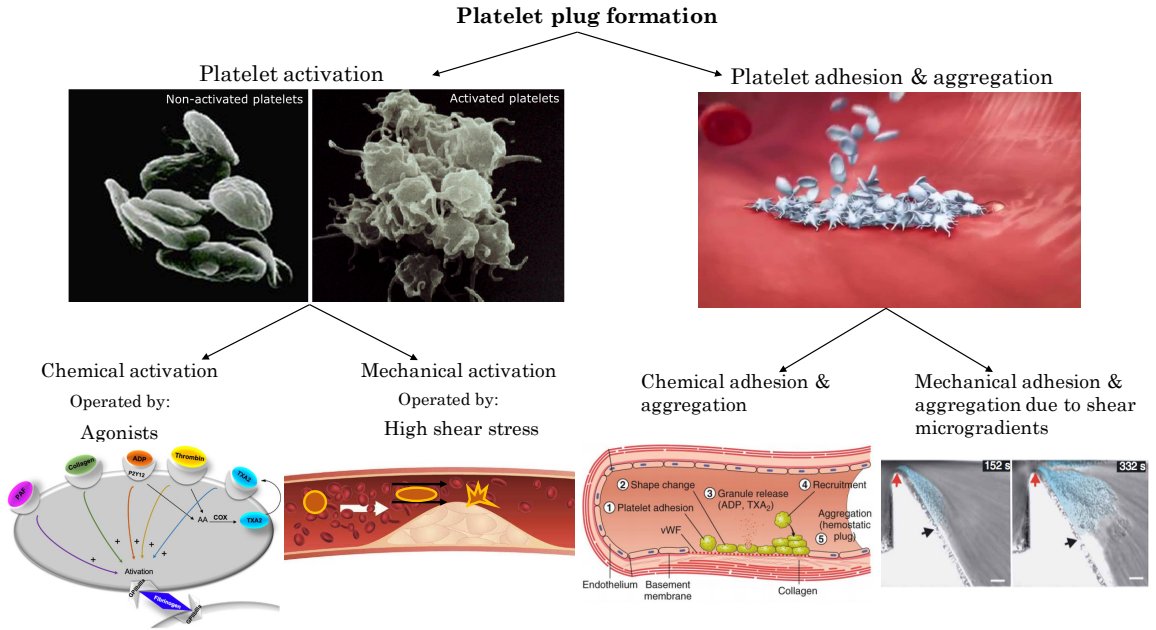

Figure 4.3: A schematization of the processes involved in platelet plug formation (Figure created using images from [105], [91],[83], [19])

Platelet aggregation

Platelet aggregation is the process of cell-to-cell adhesion, i.e. during aggregation the platelets adhere to other platelets, creating a plug. Platelet aggregation, as well as platelet activation, can be induced by chemical and/or mechanical factors. Chemical aggregation of platelets is mediated by agonists. As we have already seen, agonists activate platelets by binding to specific receptors on the platelet surface, and activated platelets recruit additional platelets to the growing hemostatic plug [100]. In addition to chemical aggregation, it has been recognized that platelet aggregation can also be mediated by mechanical factors, occurring in regions of blood flow disturbance after vascular injury. In particular, Nesbitt et al. [83] have shown that shear deceleration due to an expansion of the blood vessel induces platelet aggregation. More specifically, Nesbitt et al. have experimentally demonstrated that localized shear gradients, in the form of an increase followed by a decrease in the shear rate, expose platelets to rapidly changing hemodynamic conditions, leading to the development of stabilized platelet aggregates. Shear gradients can occur in the case of changes in vessel geometry (stenosis) as a consequence of thrombus formation itself or within cardiovascular devices.

Platelet exposure to sudden increases in shear promotes the development of membrane tethers (platelet activation), leading to the formation of transient discoid platelet aggregates. Upon subsequent exposure to decreasing shear, these tethers physically restructure, increasing the strength and stability of the discoid platelet aggregates, thereby promoting thrombus growth. Figure 4.4 reports the results obtained by Nesbitt et al. [83].

4.2.2   Secondary hemostasis

Secondary hemostasis is defined as the formation of insoluble, cross-linked fibrin by activated coagulation factors, specifically thrombin. Fibrin stabilizes the primary platelet plug. Secondary hemostasis consists of a series of enzymatic reactions, termed the coagulation cascade. The coagulation cascade can be divided into the extrinsic, the intrinsic (or contact), and the common pathways.

When the vascular system is injured, blood is exposed to extravascular tissues, which are rich in tissue factor (TF). The complex of TF and factor VIIa activates factor X and factor IX. This activation pathway is historically termed the extrinsic pathway of coagulation [75]. Factor IXa also activates factor X, in the presence of its co-factor factor VIIIa. Factor Xa, also in the presence of its co-factor factor Va, activates prothrombin to generate thrombin [88]. Thrombin has the main role in the coagulation cascade, because on the one hand it enables the formation of fibrin and on the other hand it greatly promotes platelet activation.

Figure 4.5 provides a chart that summarizes the main steps of the coagulation cascade.
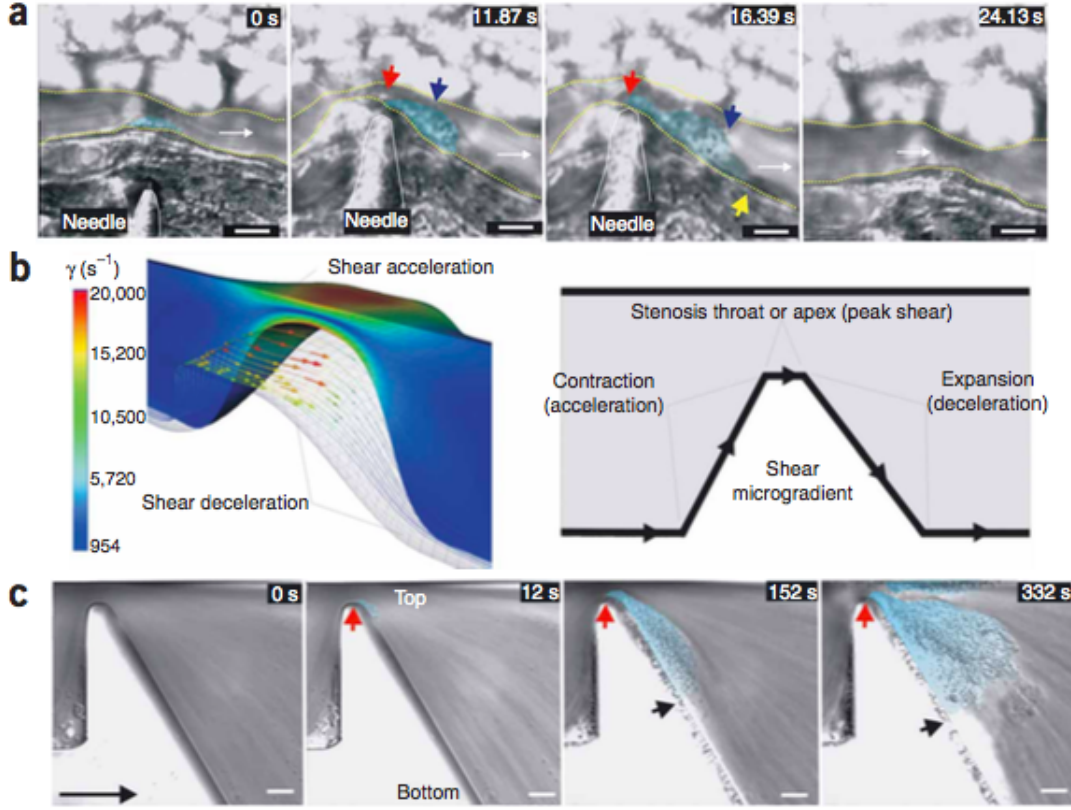
Figure 4.4: Shear gradients promote platelet aggregate formation. Nesbitt et al. results [83]: a) results in vivo in a mouse mesenteric arteriole b) CFD simulation of blood flow dynamics after localized vessel wall compression (left) and schema illustrating the three principal components defining a shear gradient or stenosis (right) c) results in a micro-channel characterized by a backward-facing

In intact and healthy blood vessels, this cascade is not activated and several anticoagulant mechanisms prevent its activation. For example, heparin stimulates the activation of the coagulation inhibitor antithrombin, which inactivates thrombin and factor Xa.

4.3   State of the art

In the past decades, Computational Fluid Dynamics (CFD) has become a very important tool in modeling and predicting the formation and the evolution of a thrombus in the cardiovascular system. One of the first continuum models of platelet aggregation was proposed by Fogelson [35],[34]. In this model, resting platelets, activated platelets and one agonist (ADP) are included, and they are
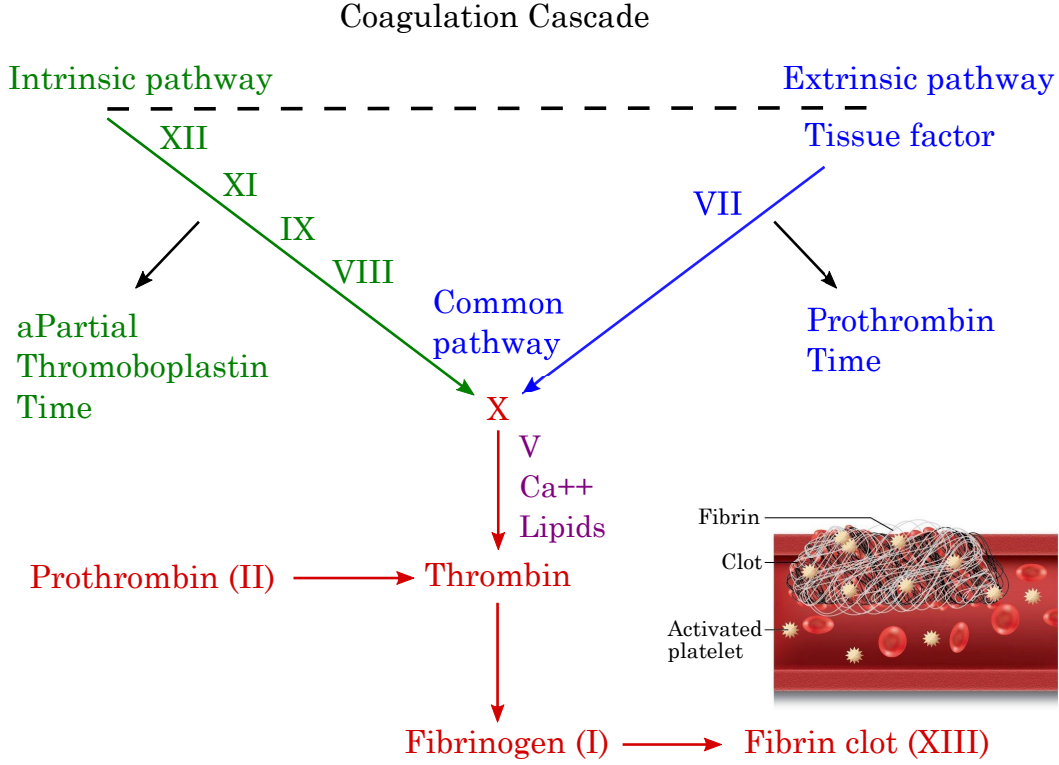
Figure 4.5: Coagulation cascade

regarded as species suspended in the blood whose concentration is obtained by solving the Navier-Stokes equations in combination with the convection-diffusion-reaction equation. Based on this work, Wang and Fogelson [132] developed numerical models, involving a hybrid finite-difference and spectral method, in order to investigate the influence of new chemically-induced activation, link formation, and shear-induced link breaking in determining when aggregates develop sufficient strength to remain intact and when they are broken apart by fluid stresses. Sorensen et al. [114],[115] used Fogelson's equations as a basis for modeling the concentration of activated and resting platelets as well as ADP [35]; they developed a more complete computational model that simulated platelet-platelet and platelet-surface adhesion, platelet activation by relevant agonists (ADP and TxA2), platelet-phospholipid-dependent thrombin generation, and thrombin inhibition by antithrombin III ATIII. The latter work is valuable, but it was mainly focused on the chemical aspect of thrombosis. Goodman et al. [38] started from the Sorensen model and added two important fluid dynamical aspects: the influence of thrombus growth on the blood flow and the possibility of embolization due to high shear stress. Hosseinzadegan and Tafti [51] based their work on Sorensen's model and introduced a rate of platelet adhesion as a function of the shear rate. Finally, Wu

et al. [138] added to the Sorensen model three important features: the study of thrombus growth, shear-induced platelet activation, and thrombus embolization due to shear.

As Sorensen et al, Menchini and Xu [78] based on convection-diffusion-reaction equation to model the resting and activated platelets transport. They predicted the formation of thrombus in the particular case of Type B aortic dissection, implementing the role of shear rates, fluid residence time, and platelet distribution. Also Bodnár and Sequeira [15] developed a model based on a series on convection-diffusion-reaction equations, but they focused on the coagulation cascade and fibrinolysis, implementing a three dimensional model and a non-Newtonian behavior of blood.

A completely different approach was proposed by Babushkina et al [2] that modeled the arterial thrombus formation using a spatial adsorption equation, their equation include the first spatial derivative of the concentration of the adhered particles and do not have a diffusion term.

Wootton et al. [136] drew attention to the effective diffusivity and modeled platelet activation and accumulation at the vessel wall whilst taking into account flow convection and shear-dependent diffusion. This blood clotting model aimed at predicting the formation of a thrombus in a vessel subject to plaque rupture and a lesion in the endothelium. The model of Wootton et al. was further employed by Jordan et al. [56] to investigate the effect of RBC-induced platelet margination and enhanced platelet diffusivity on the adhesion of platelets.

With regard to the influence of thrombus growth on the flow field, a detailed study was proposed by Leiderman and Fogelson [70], who developed a spatio–temporal mathematical model of platelet aggregation and blood coagulation under flow that includes detailed descriptions of coagulation biochemistry, chemical activation and deposition of blood platelets, as well as the two-way interaction between the fluid dynamics and the growing platelet mass, accounting for the porous nature of the thrombus and studying how advective and diffusive transport to and within the thrombus affects its growth at different stages and spatial locations. A further step in this direction was made by the model of Govindarajan et al. [39], which allows the identification of the distinct patterns characterizing the spatial distributions of thrombin, platelets, and fibrin accumulating within a thrombus.

Besides studies, such as the Sorensen one, that attribute platelet plug formation to agonists alone, there are some literature studies that propose models of platelet plug formation based mainly on the mechanical aspects. Yazdani et al. [140] developed a shear-dependent platelet adhesive model based on the Morse potential that is calibrated by existing in vivo and in vitro experimental data, coupled with a tissue-factor/contact pathway coagulation cascade, representing the relevant biology of thrombin generation and fibrin deposition. Massai et al. [76] performed a comprehensive analysis of the local hemodynamics within an image-based model of a 51% stenosed internal carotid artery and focused on the influence of disturbed

flow caused by the stenosis on flow-induced platelet activation. Rukhlenko et al. [99] investigated the shear stress-induced permeability of the vessel wall to procoagulants building up inside an atherosclerotic plaque. They implemented a two dimensional domain with a stenosis and treated blood coagulation as a phase transition from a liquid to polymerized and gelled state, modeling the permeability of the vessel wall to procoagulants as a function of wall shear stress.

Although the existing literature provides valuable models of platelet aggregation and thrombus formation, a thrombogenesis model which takes into account the bio-chemical aspect of the problem, i.e the role of the agonists generated at sites of vascular injury, but also the role of shear gradients [83] is still lacking. The role of shear gradients would be expected to become critical in the case of stenosed arteries/arterioles and/or within cardiovascular devices. To this regard, the present work proposes a computational model that includes: i) platelet activation, induced by both agonists generated at sites of vascular injury and high shear stress; ii) kinetics and mechanics of platelet-platelet and platelet-surface adhesion; iii) platelet aggregation induced by shear deceleration; iv)alterations in local fluid dynamics due to the presence of a thrombus; v) platelet recirculation; and vi) platelet production by megakaryocytes.

4.4 Methods: Computational modeling of thrombus formation

The present work aims to study platelet aggregate size and platelet deposition at the wall in a damaged blood vessel, evaluating in detail the role of shear gradients in thrombus formation. COMSOL Multiphysics 5.4, a multi-physics commercial software package based on the finite element method, was used.

The hyphothesis of continuum system is assumed and the platelets along with the agonists and anticoagulant agents were considered as dilute species that are transported by the blood flow.

Blood is regarded as an incompressible, Newtonian fluid. The assumption of Newtonian behavior is considered valid at high shear rates, which are typical of the arterial flows that are our primary interest.

The Navier-Stokes equations and the convection-diffusion-reaction equations were solved using the Laminar Flow module and the Transport of Diluted Species module in COMSOL. A None units system model was created, in order to handle the different concentration units, $PLTml^{-1}$ (platelet concentration) and $molL^{-1}$ (agonist concentration), that characterize the system. For these studies, a two-dimensional rectangular flow channel was simulated.

Schematizing the implementation of the present model, it is composed of four fundamental parts: i) chemical platelet activation and aggregation; ii) mechanical platelet activation and aggregation (role of shear gradients); iii) thrombus growth

and its influence on the flow field; and iv) platelet recirculation and production.

To model platelet activation and aggregation induced by agonists, we based our work on the model of Sorensen et al. [114],[115]. Sorensen et al. developed a two-dimensional model that simulates platelet-platelet and platelet-surface adhesion, platelet activation by relevant agonists, platelet phospholipid-dependent thrombin generation, and thrombin inhibition by antithrombin ATIII with heparin catalysis.

4.4.1   Chemical platelet activation and aggregation

Sorensen model

The Sorensen et al. model can be described by a coupled set of convection-diffusion-reaction equations, each of which has the form:

$$\frac{\partial [C_i]}{\partial t} + \boldsymbol{u} \cdot \boldsymbol{div}([C_i]) = \boldsymbol{div}(D_i \cdot \boldsymbol{grad}[C_i]) + S_i \tag{4.1}$$

Here, $\boldsymbol{div}$ is the divergence operator and $\boldsymbol{grad}$ is the gradient operator. D_i refers to the diffusivity of species i in blood; u is the two-dimensional fluid velocity vector; $[C_i]$ is the concentration of species i; and S_i is a source term for species i. The species involved in this model are the following:

1. Resting platelets (abbreviated to RP);

2. Activated platelets (abbreviated to AP);

3. Agonist released from platelet granules, such as ADP (abbreviated to a_{pr});

4. Agonist synthesized by the activated platelet, such as thromboxane $TxA2$ (abbreviated to a_{ps});

5. Prothrombin, abbreviated to PT;

6. Thrombin, generated from prothrombin on platelet phospholipid membranes (abbreviated to T);

7. ATIII, antithrombin, which inhibits thrombin and whose action is catalyzed by heparin (abbreviated to AT).

The following is the form of the source term S_i considered by the authors for each species:

-

$$S_{RP} = -k_{pa,chem} \cdot [RP] \tag{4.2}$$

-

$$S_{AP} = k_{pa,chem} \cdot [RP] \tag{4.3}$$

-

$$S_{apr} = +\lambda_j \cdot k_{pa,chem} \cdot [RP] - k1, j \cdot [a_{pr}] \tag{4.4}$$

-

$$S_{aps} = +s_{pj} \cdot k_{pa,chem} \cdot [RP] - k1, j \cdot [a_{ps}] \tag{4.5}$$

-

$$S_{pt} = -\beta[PT](\phi_{at} \cdot [AP] + \phi_{rt} \cdot [RP]) \tag{4.6}$$

-

$$S_t = -\Gamma[T] + [PT](\phi_{at} \cdot [AP] + \phi_{rt} \cdot [RP]) \tag{4.7}$$

-

$$S_{at} = -\Gamma \cdot \beta[T] \tag{4.8}$$

In these equations, $k_{pa,chem}$ represents a first-order reaction rate constant (in s^{-1}), which determines the rate of activation of resting platelets–i.e. the rate of consumption of resting platelets and of generation of activated platelets by the first-order reaction $k_{pa,chem}[RP]$– as a function of local agonist concentrations; λ_j is the amount of agonist j released per platelet, so that $+\lambda_j \cdot k_{pa} \cdot [RP]$ represents the rate at which agonist j is generated from newly activated platelets. The equation for a_{ps} represents the transport, generation, and inhibition of an agonist which is synthesized by the activated platelet and the term $s_{p,j}$ is the rate of synthesis of the agonist. In this equation and in that for a_{pr} , $k_{1,j}$ is a first-order reaction rate constant for the inhibition of agonist j.

To define $k_{pa,chem}$, the authors considered a simplistic linear rate equation with an activation threshold:

$$k_{pa,chem} = \begin{cases} 0, \Omega < 1, \\ \frac{\Omega}{t_{act}}, \Omega \geq 1 \end{cases} \tag{4.9}$$

where Ω is the activation function:

$$\Omega = \sum_{j=1}^{n_a} w_j \frac{[a_j]}{[a_{j,crit]}} \tag{4.10}$$

In these equations, n_a is the total number of agonists in the model; a_j is the concentration of the j-th agonist; $a_{j,crit}$ is the threshold concentration of that agonist for platelet activation; w_j is an agonist-specific weight to mimic the differential effects of strong and weak agonist on the activation reaction which here we assume equal to one for all the agonists; and t_{act} is a "characteristic" time constant for platelet activation in s.

The source terms for PT, T, and AT represent the thrombin-related portion of the model. It is assumed that the generation of thrombin from prothrombin takes place both on surface-bound and bulk platelets; the equations for surface-based thrombin

generation are incorporated into the boundary conditions, described below. To represent the different rates of thrombin generation from prothrombin at the surface of resting and activated platelets, the rate constants ϕ_{rt} and ϕ_{at} in the source terms for PT and T were employed. In the source terms for T and AT, Γ is the rate of the heparin-catalyzed inactivation of thrombin by antithrombin, which depends on different factors, such as the concentration of heparin [H] (which is assumed constant during the process), the concentration of thrombin and antithrombin:

$$\Gamma = \frac{k_{1,T}[H][AT]}{\alpha K_{AT} K_T + \alpha K_{AT}\beta[T] + [AT]\beta[T]} \tag{4.11}$$

In Eq.(4.11), $k_{1,T}$ is a first-order rate constant in s^{-1}, K_T and K_{AT} are the dissociation constants (in μM) for heparin/thrombin and heparin/ATIII, respectively; α represents a factor to simulate a change in affinity of heparin for ATIII when it is bound to thrombin or for thrombin when it is bound to ATIII; and β is a conversion factor to convert thrombin concentration from Uml^{-1} to μM (see Appendix C for the values of these parameters).

Platelet-platelet and platelet-surface adhesion are modeled via surface-flux boundary conditions. Platelet activation due to surface adhesion is also included, as are surface-based agonist generation and agonist-induced activation of wall-bound resting platelets. The equations for these boundary conditions are as follows: (where a positive term indicates an efflux or consumption from the domain and a negative term indicates an influx or generation):

- reactive wall flux boundary condition BC for RP: adhesion to surface only, not to other platelets

$$j_r(x,t) = S(x,t) \cdot k_{rs} \cdot [RP]; \tag{4.12}$$

- reactive wall flux BC for AP: adhesion to surface and to deposited activated platelets

$$j_a(x,t) = (S(x,t) \cdot k_{as} + \frac{M_{as}(x,t)}{M_\infty} \cdot k_{aa}) \cdot [AP]; \tag{4.13}$$

- reactive wall flux BCs for a_{pr}: platelet-released agonist generation

$$j_{pr}(x,t) = -\lambda_j \cdot (\theta \cdot S(x,t) \cdot k_{rs} \cdot [RP] + k_{pa} \cdot M_r(x,t)); \tag{4.14}$$

- reactive wall flux BCs for a_{ps}: platelet-synthesized agonist generation

$$j_{ps}(x,t) = -M_{at}(x,t) \cdot s_{p,j}; \tag{4.15}$$

- reactive wall flux BC for PT: consumption due to thrombin generation:

$$j_{pt}(x,t) = \beta \cdot (M_{at}(x,t)\phi_{at} + M_r(x,t)\phi_{rt}) \cdot [PT]; \tag{4.16}$$

58

- reactive wall flux BC for T: generation from prothrombin on deposited platelets:

$$j_t(x,t) = -(M_{at}(x,t)\phi_{at} + M_r(x,t)\phi_{rt}) \cdot [PT]; \qquad (4.17)$$

Here, species concentrations are the values at a reactive wall. In these equations, k_{rs} , k_{as} and k_{aa} are heterogeneous reaction rate constants that govern the rates of adhesion between, respectively, resting platelets and the surface; activated platelets and the surface; and depositing and surface-bound activated platelets.

The platelet-surface deposition equations (4.12),(4.13),(4.14) include a saturation effect which prevents additional platelet-surface adhesion once the capacity of the surface for platelets is reached. The saturation term is defined as follows:

$$S(x,t) = 1 - \frac{M(x,t)}{M_\infty} \qquad (4.18)$$

where M_∞ is the total capacity of the surface for platelets and $M(x,t)$ is the total surface coverage with platelets at time t and at position x, (both in PLT cm^{-2}) :

$$M(x,t) = \int_0^t (j_r(x,t) + k_{as}S(x,t) \cdot [AP])dt. \qquad (4.19)$$

The authors also define $M_{as}(x,t)$ which represents the portion of the total surface coverage $M(x,t)$ which is due to activated platelets, and it is defined as follows:

$$M_{as}(x,t) = \int_0^t (\theta \cdot j_r(x,t) + k_{as}S(x,t) \cdot [AP] + k_{pa,chem} \cdot M_r(x,t))dt \qquad (4.20)$$

Here, θ is the fraction of adhering, resting platelets which activate upon surface contact and which can vary between 0 and 1; k_{pa} is the activation rate constant evaluated at the wall as a function of the agonist present; and $M_r(x,t)$ is the portion of the total surface coverage due to resting platelets:

$$M_r(x,t) = \int_0^t ((1-\theta)j_r(x,t) - k_{pa,chem} \cdot M_r(x,t))dt \qquad (4.21)$$

so that $k_{pa,chem}M_r(x,t)$ is the rate of activation of deposited, resting platelets by agonists. Equations (4.16) and (4.17) are the thrombin-related surface fluxes and are analogous to the bulk thrombin generation source terms with bulk concentrations replaced by surface concentrations. In these equations, $M_{at}(x,t)$ is the total amount of deposited, activated platelets (activated platelet-surface plus platelet-platelet adhesion):

$$M_{at}(x,t) = \int_0^t (\theta \cdot j_r(x,t) + j_a(x,t) + k_{pa,chem} \cdot M_r(x,t))dt. \qquad (4.22)$$

Red blood cells have been shown to have a shear-dependent diffusion-augmenting effect on the transport of platelets and large proteins. One way to simulate this is by

adjusting the diffusivities D_i of platelets and larger species (thrombin, prothrombin, and ATIII) from the Brownian values, in particular $D_i = D_{b,i} + D_s$, where $D_{b,i}$ and D_s are the Brownian and shear-enhanced diffusivities, respectively. To this regard, the Keller formulation is implemented [59], in which the augmentation factor is linearly proportional to local shear rate and to red blood cell size:

$$D_s = 0.18 \cdot d_{rbc}^2 \cdot \dot{\gamma}/4 \qquad (4.23)$$

where d_{rbc} is the diameter of a red blood cell $\sim 5.5 \mu m$, and $\dot{\gamma}$ is the local fluid shear rate. In arteries and arterioles, that are our primary interest, the shear rate is generally > 500 1/s. Thus, for instance, platelet enhanced diffusivity is at least 10^3 higher of the molecular one.

Modeling chemical platelet activation and aggregation with COMSOL

A rectangular two-dimensional domain was implemented in COMSOL and different domain sizes were implemented. The Navier-Stokes equations were solved assuming a pressure gradient between the inlet and the outlet of the domain –except in case of the simulations for the validation of the chemical part of the model, see Results– and no slip conditions were imposed at the rigid walls.

The convection-diffusion-reaction equations were solved coupled with the Laminar Flow module. For the platelets and the larger species (thrombin, prothrombin and antithrombin), the shear-enhanced diffusivity evaluated via eq. (4.23) was added to the Brownian diffusivity.

At the inlet, uniform, constant concentration Dirichlet boundary conditions were imposed for all species. In particular, for prothrombin, resting and activated platelets and antithrombin, the physiological values reported by Sorensen et al. were set, while for the other species a zero concentration inlet was considered. Table 4.1 reports the physiological values of the main model parameters and Appendix C reports the values of the remaining parameters.

At the outlet, an outflow condition, i.e. $-\vec{n} D_i \nabla C_i = 0$, was imposed for all species. The source terms reported by Sorensen et al. were set in the model. In order to avoid function discontinuities, and consequently numerical instabilities, it was decided to model the platelet activation rate as $\Omega \cdot step(\Omega)$ where $step(\Omega)$ is a smooth step function localized where Ω is equal to one and with the minimun and the maximum values equal to zero and one, respectively.

As already described, Sorensen et al. modeled platelet-platelet and platelet-surface adhesion through surface-flux boundary conditions. The flux boundary conditions are coupled with the saturation term (Eq.4.18) and the expression of M, the total surface coverage with platelets (Eq.4.19). Firstly, in order to have a single uncoupled equation that describes the behavior over time of the total surface coverage with platelets, M, we combined Equations (4.12) (4.18), and (4.19),

obtaining:

$$M(x,t) = \int_0^t ((1 - \frac{M(x,t)}{M_\infty})k_{rs}[RP] + (1 - \frac{M(x,t)}{M_\infty})k_{as}[AP])dt. \qquad (4.24)$$

Differentiating Eq.(4.24), it is possible to obtain an ordinary differential equation that describes the evolution of the total surface coverage with platelets over time.

$$\frac{dM(x,t)}{dt} = (1 - \frac{M(x,t)}{M_\infty})k_{rs}[RP] + (1 - \frac{M(x,t)}{M_\infty})k_{as}[AP], \qquad (4.25)$$

Proceeding analogously for $M_{as}(x,t)$, the portion of the total surface coverage due to activated platelets, M_r, the portion due to resting platelets, and $M_{at}(x,t)$, the total amount of deposited activated platelets, we obtain:

$$\frac{dM_r(x,t)}{dt} = (1 - \theta)(1 - \frac{M(x,t)}{M_\infty})k_{rs}[RP] - k_{pa,chem}M_r(x,t) \qquad (4.26)$$

$$\frac{dM_{as}(x,t)}{dt} = (1 - \frac{M(x,t)}{M_\infty})(\theta k_{rs}[RP] + k_{as}[AP]) + k_{pa,chem}M_r(x,t) \qquad (4.27)$$

$$\frac{dM_{at}(x,t)}{dt} = (1 - \frac{M(x,t)}{M_\infty})(\theta k_{rs}[RP] + k_{as}[AP]) + \frac{M_{as}}{M_\infty}k_{aa}[AP] + k_{pa}M_r(x,t) \quad (4.28)$$

In order to impose the proper flux boundary conditions (Eqs.4.12-4.17), the ODE system above has to be solved. Thus, the overall model is represented by a coupled Navier Stokes-CDR-ODE process. The ODE system was solved using the Mathematic module Boundary ODEs. Here the right terms in Equations (4.25)-(4.28) were set as source terms. For antithrombin, a no flux condition was imposed.

4.4.2 Modeling the influence of thrombus growth on the flow field

Thrombus growth was tracked with time, assuming an impermeable thrombus, and the associated alterations in local fluid dynamics were determined. To this end, a deformable domain was considered. More specifically, it was decided to parametrize the normal displacement of the domain boundary representing the reactive surface –i.e. the damaged wall– on which platelets are adhering. This deformation of the spatial domain, discretized by finite elements, is possible by using the Moving mesh module of COMSOL 5.4 and choosing an Arbirary Lagrangian-Eulerian formulation (ALE). The normal mesh displacement at the reactive wall was imposed as follows:

$$d_n = h \cdot V_{plt} \cdot M_{at}, \qquad (4.29)$$

where V_{plt} is the volume of a single platelet, M_{at} is the total platelet deposition on the reactive wall [PLTs/cm²] and h is a scale factor that takes into account the

presence of red blood cells in the thrombus. With this formulation, at each time step, the total platelet deposition is evaluated and consequently the normal mesh displacement is determined. This mesh displacement influences the flow field at the following time step.

At the other boundaries, a zero normal mesh displacement was imposed.

A thrombus can be composed mainly of platelets–termed white thrombus–, or it can be composed of platelets and red blood cells because during its formation and evolution it can trap a large number of red blood cells–termed red thrombus. In order to take into account the presence of red blood cells in establishing the thrombus size, the term V_{plt} can be increased in Eq. 4.29. The volume of a single red blood cell is around $24 \cdot V_{plt}$. Thus, ranging the values of the scale factor h from 1 –i.e. a thrombus composed exclusively of platelets– to 24 –i.e. the unrealistic condition of a thrombus composed exclusively by red blood cells– it is possible to model the size of thrombi of different composition. For this study, an intermediate value of $h = 9$ was considered.

4.4.3 Modeling the role of shear gradients

Platelet activation and aggregation induced by shear gradients, as demonstrated by Nesbitt et al. [83], was included in the present model.

To implement the mechanical platelet activation due to the high shear rate in the contraction zone, it was decided to use a first-order reaction rate constant $k_{pa,mech}$ (in s^{-1}), which determines the rate of activation of resting platelets as a function of local shear rate. Following the Sorensen approach, for $k_{pa,mech}$, a linear equation with an activation threshold was considered:

$$k_{pa,mech} = \begin{cases} 0, & \frac{\dot{\gamma}}{\dot{\gamma}_{crit}} < 1, \\ \frac{\dot{\gamma}}{\dot{\gamma}_{crit} \cdot t_{act}}, & \frac{\dot{\gamma}}{\dot{\gamma}_{crit}} \geq 1 \end{cases} \tag{4.30}$$

where $\dot{\gamma}$ is the shear rate of the blood flow and $\dot{\gamma}_{crit}$ is the critical shear rate at which the resting platelets start to become activated. Thus, in the proposed model, the rate of activation of resting platelets is the sum of the chemical activation rate and the mechanical activation rate:

$$k_{pa} = k_{pa,chem} + k_{pa,mech} \tag{4.31}$$

Based on the experimental evidence [83], it appears that platelet aggregation is influenced by the magnitude of the shear gradient. Thus, to model the adhesion and aggregation of the platelets downstream of the contraction, it was decided to introduce a flux boundary condition for the resting and activated platelets that is proportional to the absolute value of the shear gradient. A threshold was introduced also for the flux boundary conditions, to account for the fact that the mechanical platelet deposition occurs when there is a decrease in the shear rate, so a negative

value of the derivative of the shear rate over x, the length of the domain. The flux boundary condition that mimics the mechanical deposition of resting platelets is:

$$j_{r,mech}(x,t) = \begin{cases} 0, & \frac{\partial \dot{\gamma}}{\partial x} \geq 0, \\ \frac{1}{max(\dot{\gamma})}|\frac{\partial \dot{\gamma}}{\partial x}|(S(x,t) \cdot k_{rs}[RP]), & \frac{\partial \dot{\gamma}}{\partial x} < 0 \end{cases} \tag{4.32}$$

While the flux boundary condition that mimics the mechanical deposition and aggregation of activated platelets is:

$$j_{a,mech}(x,t) = \begin{cases} 0, & \frac{\partial \dot{\gamma}}{\partial x} \geq 0, \\ \frac{1}{max(\dot{\gamma})}\left|\frac{\partial \dot{\gamma}}{\partial x}\right|(S(x,t) \cdot k_{as} + \frac{M_{as}(x,t)}{M_\infty} \cdot k_{aa}) \cdot [AP], & \frac{\partial \dot{\gamma}}{\partial x} < 0 \end{cases} \tag{4.33}$$

In Eq. (4.32)-(4.33), the shear gradient was scaled by the maximum value of the shear rate in order to obtain a more feasible value of the fluxes. The flux boundary conditions that characterize the coupled chemical and mechanical problem become:

$$j_r(x,t) = S(x,t) \cdot k_{rs} \cdot [RP] + j_{r,mech}; \tag{4.34}$$

$$j_a(x,t) = (S(x,t) \cdot k_{as} + \frac{M_{as}(x,t)}{M_\infty} \cdot k_{aa}) \cdot [AP] + j_{a,mech}; \tag{4.35}$$

$$j_{pr}(x,t) = -\lambda_j \cdot (\theta(\cdot S(x,t) \cdot k_{rs} \cdot [RP] + j_{r,mech}) + k_{pa} \cdot M_r(x,t)); \tag{4.36}$$

$$j_{ps}(x,t) = -M_{at}(x,t) \cdot s_{p,j}; \tag{4.37}$$

$$j_{pt}(x,t) = \beta \cdot (M_{at}(x,t)\phi_{at} + M_r(x,t)\phi_{rt}) \cdot [PT]; \tag{4.38}$$

$$j_t(x,t) = -(M_{at}(x,t)\phi_{at} + M_r(x,t)\phi_{rt}) \cdot [PT]; \tag{4.39}$$

and the ODE system that describes the total platelet deposition on the damaged surface, including both the chemical and mechanical contributions, becomes:

$$\frac{dM_r(x,t)}{dt} = (1-\theta)(1 - \frac{M(x,t)}{M_\infty})(k_{rs}[RP] - k_{pa}M_r(x,t) + j_{r,mech}) \tag{4.40}$$

$$\frac{dM_{as}(x,t)}{dt} = (1 - \frac{M(x,t)}{M_\infty})(\theta k_{rs}[RP] + k_{as}[AP]) + k_{pa}M_r(x,t) + j_{a,mech} \tag{4.41}$$

$$\frac{dM_{at}(x,t)}{dt} = (1 - \frac{M(x,t)}{M_\infty})(\theta k_{rs}[RP] + k_{as}[AP]) + \frac{M_{as}}{M_\infty}k_{aa}[AP] + k_{pa}M_r(x,t) + j_{r,mech} + j_{a,mech} \tag{4.42}$$

4.4.4 Modeling the role of cardiovascular circulation and platelet production

The platelet average life span is about 10 days [109], while the hemostatic process has a characteristic time that ranges between minutes and hours.

It can be assumed that during the hemostatic process, due to the circulation of blood inside the cardiovascular system, the same platelets pass many times over the damaged surface. In order to mimic the circulation of blood, and consequently platelet re-circulation in the cardiovascular system, periodic conditions were imposed, for the convection-diffusion-reaction problem, associating the inlet edge and the outlet edge of the model.

The Periodic boundary condition defines a special type of symmetry that obeys cyclic/repeating condition of the flow across the boundary surface. The two boundary faces are physically connected and the flow exiting/entering from one face then enters/exits the other face. In this way, the same platelets pass several times over the damaged surface, reproducing what physiologically occurs in the cardiovascular system, which is a loop. We are allowed to implement a periodic boundary condition, for the convection-diffusion-reaction problem, in our domain because in the rest of the cardiovascular system, which is assumed to be undamaged, the changes in the concentration of the considered species are negligible.

On the other hand, resting platelets are produced continuously by megakaryocytes. This continuous and constant platelet production was implemented in our model, adding a constant production term S_p to the source term that describes the resting platelet reaction:

$$S_{RP} = -k_{pa} \cdot [RP] + S_p \tag{4.43}$$

4.4.5 Meshing and Solver features

To study the chemical platelet activation and aggregation, the domain was discretized using a fine mesh, and five boundary mesh layers were considered at the reactive wall. The regularity and the simplicity of the geometry was exploited; quadrilateral elements were used enabling an extremely regular computational mesh and thus allowing a reduction in computational time. This rather fine mesh allows an accurate estimation of the platelet distribution along the damaged surface. However, once the moving mesh was introduced, to ensure the stability of the calculation it was necessary to change the discretization of the computational domain. The quadrilateral elements were replaced by triangular elements, and an increased mesh size was considered because small elements can induce node overlapping during the process of mesh deformation.

In order to improve the accuracy of the model and avoid numerical overshoot in the time dependent solver, we choose to increase the maximum number of iterations (from 8 to 50) and to increase the maximum BDF order from 1 to 5. To improve

convergence, we choose to change the COMSOL nonlinear method from Constant (Newton) to Automatic (Newton) which implements a damped Newton's method approach. This automatically updates the Jacobian and uses a dynamic damping term, and it is recommended in case of strongly nonlinear problems.

Stabilization techniques

As we have already seen in the previous chapter (in the computational drug dispersion model), for convection-dominated transport problems, the Galerkin method used by COMSOL to discretize the equations may become unstable [107]. Since our CDR problem is convection-dominated, with a Péclet number of $\sim 10^3$, stabilization techniques are required. Also in this case, it was decided to consider isotropic diffusion, an inconsistent method, that adds to the physical diffusion coefficient an artificial isotropic diffusion coefficient and a value of the tuning parameter $\delta = 0.25$ was set.

4.5 Results from the thrombus formation model

The developed computational model allows us to evaluate the thrombus size within the blood vessel, average platelet deposition and its behavior along the length of the damaged surface.

The results reported in this section show the different aspects of the thrombogenesis implemented in this model.

Firstly, the thrombus formation induced by agonists was shown in terms of platelet deposition (Fig.4.6) and in terms of domain deformation (Fig.4.7). Then the results of the mechanical platelet activation and aggregation processes were reported, in terms of distribution of mechanically activated platelets (Fig.4.8) and in terms of platelet aggregate size promoted by shear gradients (Fig.4.9). Finally the role of the shear gradients were investigated in detail (Fig.4.11 and 4.12).

Table 4.1 provides the physiological values of the main model parameters (see Appendix C for the remaining parameters).

Firstly, the part of the proposed model concerning the chemical platelet activation and aggregation, developed basing on Sorensen et al. work, was tested. The results obtained were compared with data from the literature involving parallel-plate Poiseuille flow of whole blood over a type I collagen substrate.

Figure 4.6 reports the comparison between the total platelet deposition as a function of axial position along the domain's reactive wall obtained by our COMSOL model against two series of experimental results, reported by Hubbell and McIntire [53] and Wagner and Hubbell [130]. We referred to the experimental data series used by Sorensen et al. to validate their model.

In the left panel, the comparison with the experimental results obtained by Hubbell and McIntire [53]– for whole blood with 10 U ml^{-1} heparin after 120 s of

Table 4.1: Physiological values of the main parameters used in the thrombus formation model

Quantity	Symbol	Value	Unit
Blood dynamic viscosity [55]	μ	0.0035	Pa· s
Blood density [114]	ρ	1110	kg/m^3
Platelet Brownian diffusion coefficient [114]	$D_{b,plt}$	$1.58 \cdot 10^{-9}$	cm^2 /s
ADP Brownian diffusion coefficient [114]	$D_{b,ADP}$	$2.57 \cdot 10^{-6}$	cm^2 /s
TxA2 Brownian diffusion coefficient [114]	$D_{b,TxA2}$	$2.14 \cdot 10^{-6}$	cm^2 /s
Thrombin Brownian diffusion coefficient [114]	$D_{b,T}$	$4.16 \cdot 10^{-7}$	cm^2 /s
Prothrombin Brownian diffusion coefficient [114]	$D_{b,PT}$	$3.32 \cdot 10^{-7}$	cm^2 /s
Antithrombin Brownian diffusion coefficient [114]	$D_{b,AT}$	$3.32 \cdot 10^{-7}$	cm^2 /s
Resting Platelet initial concentration [114]	$[RP]_i$	$1.5 - 3 \cdot 10^8$	PLT/ml
Activated platelet initial concentration [114]	$[AP]_i$	$0 - 0.05[RP]$	PLT/ml
Prothrombin initial concentration [114]	$[PT]_i$	1.1	μM
Antithrombin initial concentration [114]	$[AT]_i$	2.844	μM
Thrombin critical concentration [114]	$[T]_{crit}$	0.1	U ml^{-1}
TxA2 critical concentration [114]	$[TxA2]_{crit}$	0.6	μM
ADP critical concentration [114]	$[ADP]_{crit}$	2	μM
Shear rate activation threshold [102],[62]	$\dot{\gamma}_{crit}$	10000	s^{-1}
Rate of adhesion of resting platelets [115]	k_{rs}	0.0037	cm/s
Rate of adhesion of activated platelets [38] [115]	k_{as}	0.135	cm/s
Platelet production rate [44],[63]	S_p	500	PLT/(ml · s)
Platelet volume [109]	V_{plt}	$4.28 \cdot 10^{-12}$	cm^3

flow and a wall shear rate $\dot{\gamma}_w =$100 s^{-1}– is reported.

In the right panel, the comparison with the experimental results of Wagner and Hubbell [130] – for whole blood with 2 U/ml heparin and with the thrombin active-site inhibitor PPACK after 75 s of flow with a shear rate $\dot{\gamma}_w = 1000 s^{-1}$– is reported. In the latter case, in order to compare correctly our model results with Wagner and Hubbell's results, the thrombin related equations of the COMSOL model were neglected, assuming that PPACK completely inhibits platelet-mediated thrombin generation [115].

A domain with an height of 200 μm and a length of 5 mm and 9 mm for simulation in the left and the right panel, respectively, were considered. To be consistent with the experimental analysis [53],[130]–whereby the inlet portion were coated with nonadhesive albumin and the remaining coated with adhesive type I collagen– the first 1 mm of the computational domains were modeled as intact surface and the rest as damaged surface–in Fig.4.6 the platelet deposition along the damaged surface is reported–.

Considering the relation between wall shear rate and maximum velocity in a Poiseuille flow for a Newtonian fluid $\dot{\gamma}_w = (\frac{\partial u_x}{\partial y})_w = \frac{2U_{max}}{H}$, Poiseuille profiles with a maximum velocity of 0.5 cm/s and 5 cm/s was imposed at the inlet in order
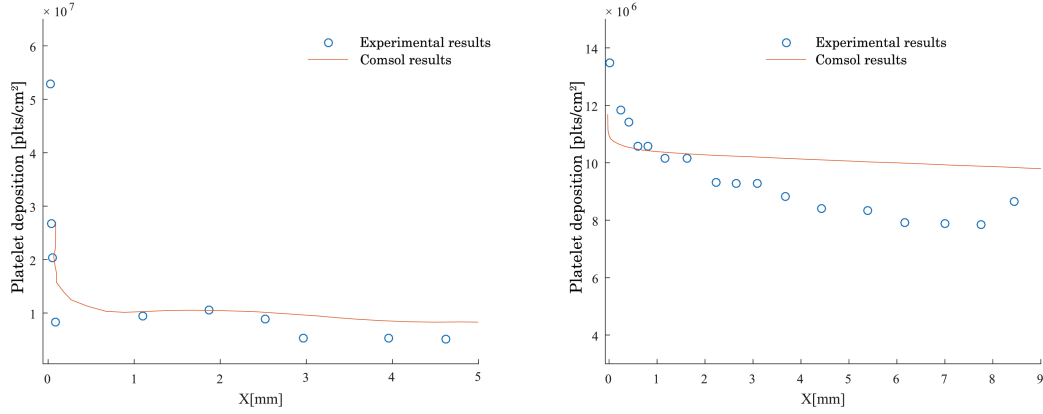
Figure 4.6: Comparison of axial platelet deposition predicted by the developed model against experimental results of Hubbell and McIntire [53] after 120 s with heparin concentration of 10 U/ml and $\dot{\gamma} = 100s^{-1}$ (left panel) and experimental results of Wagner and Hubbell [130] for whole blood with 2 U/ml heparin and with thrombin active-site inhibitor PPACK after 75 s of flow with $\dot{\gamma} = 1000s^{-1}$(right panel).

to guarantee the same shear rates of the experimental data 100 s^{-1} and 1000 s^{-1}, respectively and at the outlet a zero pressure condition was imposed. Furthermore, following the Sorensen procedure, for these simulation, at the inlet of the domain a continuous influx of resting platelets and a little continuous influx of activated platelets – $0.05 \cdot [RP]$– were considered and an outflow condition at the outlet was set.

Figure 4.6 shows that the proposed COMSOL model succeeds in predicting the experimental platelet deposition magnitudes both in the case of low shear rate ($\dot{\gamma} = 100s^{-1}$) and in the case of high shear rate ($\dot{\gamma} = 1000s^{-1}$). However, for high shear rate, the shape of the curve differs from that observed experimentally, being more flat. Both in experimental and numerical case, the deposition curves decrease along the length of the domain, Hubbell and McIntire [53] justified this behavior saying that "near the inlet, the thrombi are larger because more platelets are available near the surface to adhere and aggregate"; from the numerical point of view this is justified by the fact that a little amount of activated platelets is implemented at the inlet and they tend to adhere immediately.

The deformation of the domain under thrombus growth 200 seconds after the onset of damage of the blood vessel is reported in Figure 4.7. Physiological conditions in a blood vessel without stenosis are implemented. In this simulation, the more realistic case, whereby only the central portion is modeled as a damaged surface, is considered; to do this the flux conditions and the releasing of agonists were implemented only in this central segment–. A rectangular domain 0.1 cm x 0.6 cm
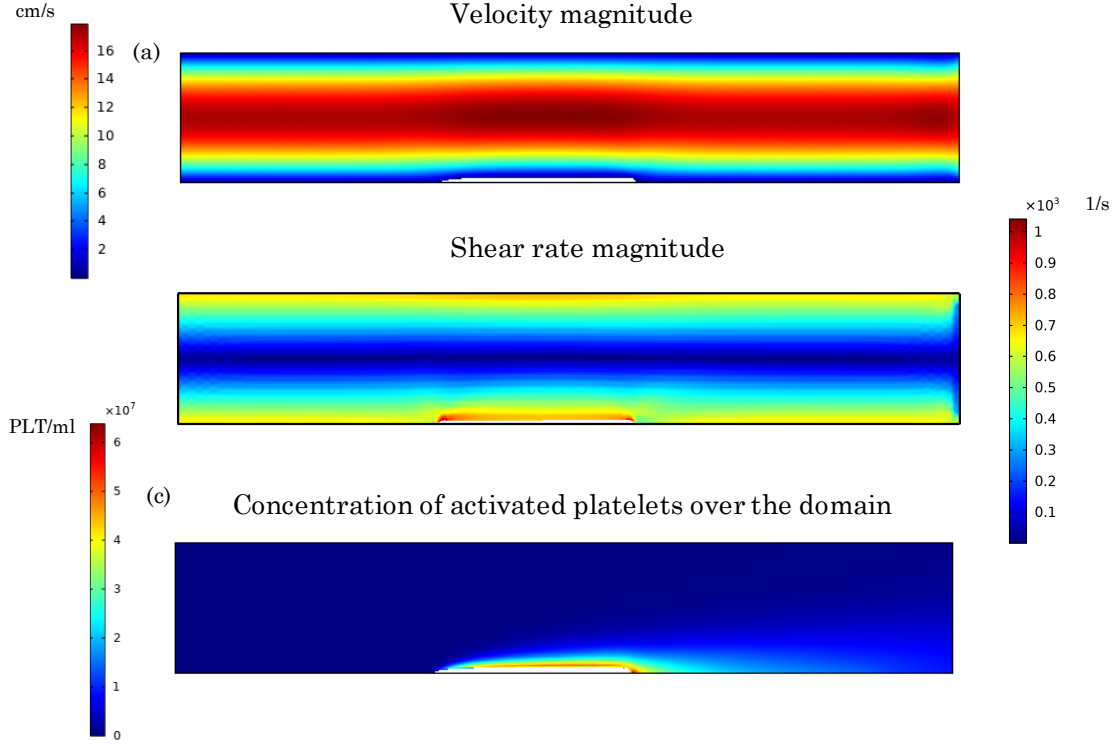
67

Figure 4.7: Thrombus growth after 200 sec in a straight vessel of height 0.1 cm and 0.6 cm length. Panel a) velocity magnitude; Panel b) Shear rate magnitude; Panel c) concentration of activated platelet (to facilitate viewing the thrombus size was increased of a factor of 10)

was considered and a pressure gradient of 30 Pa was imposed.

In this analysis, having a low shear rate and low spatial shear gradients (Fig.4.7 panel b), the mechanical contribution to thrombus formation is negligible. Panel (a) depicts the behavior of the flow field. Under physiological conditions, the velocity field has a slight increase of magnitude –and a consequent slight increase of the shear rate, see panel (b)– in the contraction zone related to the thrombus. Panel c shows the concentration of activated platelets over the domain. Due to the low shear rate, the platelets are activated exclusively by the agonists at the site of injury. Indeed, the activated platelets exhibit the maximum concentration at that location, and then they are transported downstream by the flow field.

On the other hand, Figure 4.8 shows mechanical platelet activation. The domain (0.1 cm x 2 cm) is characterized by an axisymmetric stenosis, within which the flow velocity and consequently the shear stress substantially increase. Blood vessels with such axisymmetric stenosis can be encountered, for example, in some cases
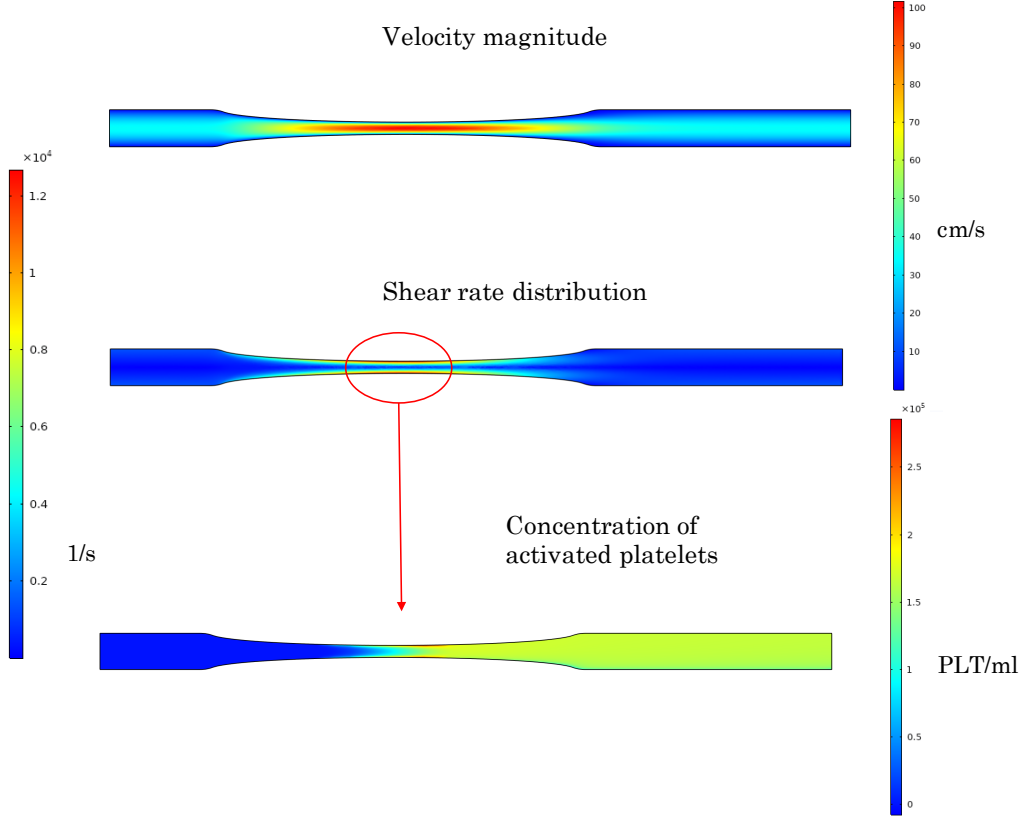
Figure 4.8: Platelet activation induced by high shear rate in an axisymmetric stenosed vessel

of stent restenosis. A pressure gradient of 1500 Pa between domain inlet and outlet was imposed and where the shear rate reaches the activation threshold, i.e. $\dot{\gamma}_{crit} = 10000 s^{-1}$ (red arrow in figure), the resting platelets become activated. The platelet reaction rate $k_{pa,mech}$ was modeled with a simple linear expression directly proportional to the shear rate Eq.(4.30); thus, activated platelets have the maximum concentration at the wall. It is worth noting that mechanical activation involves a more uniform distribution of the activated platelets compared to chemical activation, because in this case, the activated platelet are produced not only in the site of injury but in all site in which the shear rate threshold is reached.

The part of the model related to shear gradients, i.e. platelet activation in the contraction zone followed by platelet aggregation in the deceleration zone, was validated against the experimental results reported by Nesbitt et al.[83]. For this analysis, a domain with a stenosis that emulates the microchannel used in [83] was considered (50 μm x 500 μm), see figure 4.4 (c). Imposing a pressure gradient of 700 Pa between the inlet and the outlet, a flow field with a peak of the shear rate of
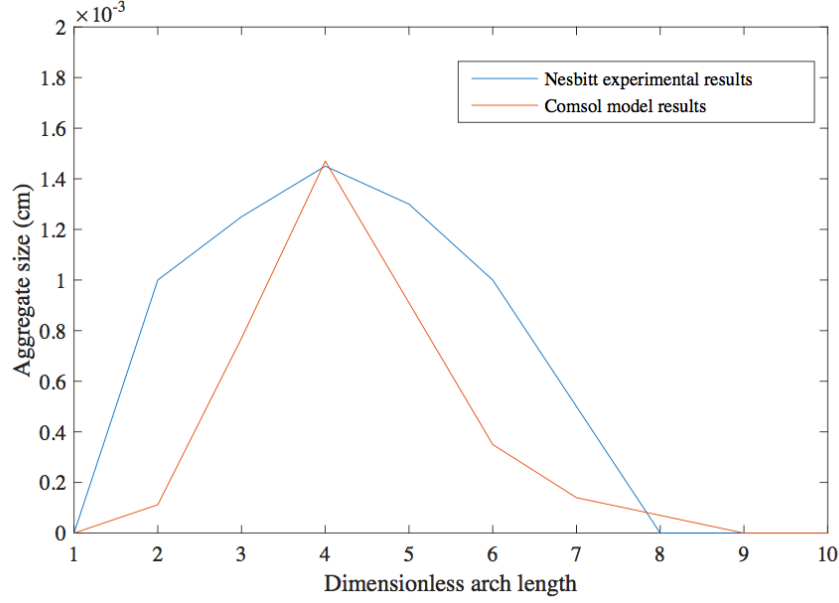
69

Figure 4.9: Comparison of the distribution of the platelet aggregate predicted by the developed model against experimental results of Nesbitt el al. [83] after 152 sec with a peak of the shear rate equal to 20000 s^{-1} in vessel 50 μm x 500 μm

20000 s^{-1} was established and a continuous influx of resting platelets was considered at the inlet. Figure 4.9 shows the size of the platelet aggregate in the deceleration zone along the dimensionless length of the domain after 152 seconds, as observed in vitro by [83] and as predicted by our model. The COMSOL model succeeds in predicting the maximum thrombus size and its position along the reactive wall. However, the predicted platelet aggregate has a sharp wedge shape that fails to reflect the experimental one.

Finally, figures 4.11 and 4.12 are intended to investigate the role of mechanical platelet activation and aggregation in thrombus formation as compared with the role of chemical platelet activation and aggregation. For this analysis, the domain represented in figure 4.10 was considered, and the percentage of stenosis is defined as $(1 - \frac{L_2}{L_1}) \cdot 100$. Blood vessels with such a localized stenosis can be found in the case of presence of atherosclerotic plaques or in the case of abnormal evolution of the thrombus itself.

For these simulations, a pressure gradient of 400 Pa between the inlet and the outlet of the domain was imposed, for studying the pulsatile case (Fig.4.11) a transient pressure gradient was implemented –i.e., $P_{inlet} = 400 \cdot cos(\omega t)$ at the inlet and zero pressure at the outlet–.

Figure 4.11 reports the maximum platelet depositions predicted after 300 seconds in a 80% stenosed flow channel (see Fig.4.10) with a Reynolds number in the
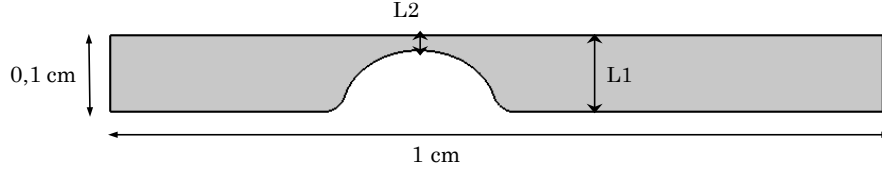
Figure 4.10: Computational domain used to investigate the role of shear gradients in thrombus formation

non-contracted section equal to 15, considering only the chemical platelet activation and aggregation and adding the role of the shear gradients (s.m.g.). This figure shows that in a vessel characterized by a significant variation of shear rate (as is the case with a vessel with a percentage of stenosis of 80%), the maximum platelet deposition considering the shear gradient contribution is substantially higher than the one evaluated considering only the chemical platelet activation and aggregation, both for steady and pulsatile flow. In the case of pulsatile flow, the maximum platelet deposition increases slightly as a result of the greater residence time of the species.

The influence of the percentage of the vessel stenosis on the maximum aggregate size is shown in Fig.4.12. Maintaining the same fluid dynamic features (Re=15) at the inlet and increasing the percentage of the localized stenosis from 0 (i.e. straight channel) to 80%, the maximum aggregate size, evaluated after 300 seconds, increases tenfold.

Discussion

The present work provides a computational model capable of predicting platelet aggregation and deposition along the damaged surface and the related thrombus size within a two-dimensional domain.

A thrombus is the physiological response of the cardiovascular system to an injury of a blood vessel. As we have described, a thrombus is the result of the hemostatic mechanism. In this model, the primary hemostasis that leads to the formation of a platelet plug is implemented. With regard to secondary hemostasis, following the Sorensen et al. [114] approach, it was modeled only partially by introducing the formation of thrombin from prothrombin and its inibhition by
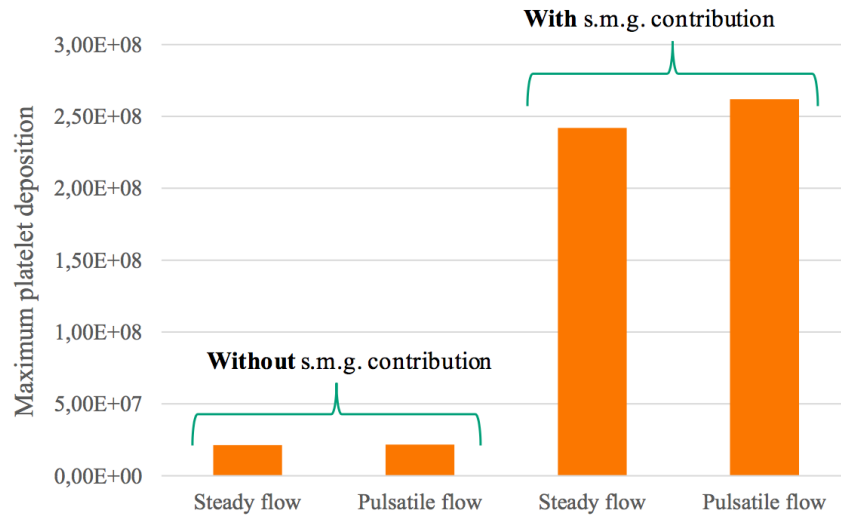
Figure 4.11: Influence of the shear gradients on the maximum platelet deposition at the wall after 300 sec considering a percentage of stenosis 80% and Re=15, in case of steady and pulsatile flow
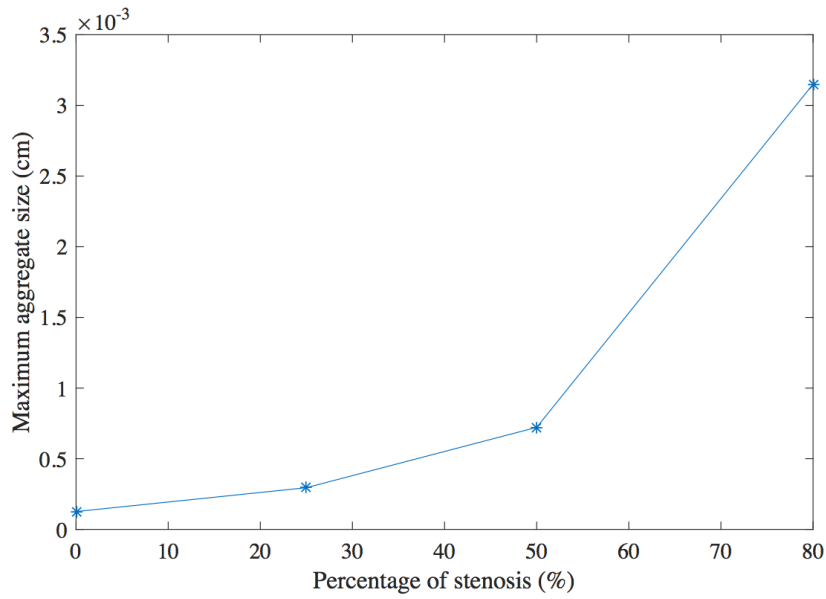

Figure 4.12: Influence of the percentage of stenosis of the blood vessel on maximum platelet aggregate size after 300 and with Re=15

antitrombin and heparin.

The results of the chemical platelet activation and aggregation were validated against two experimental data series (see Fig.4.6). The results in terms of predicted magnitude are satisfactory, while for high shear stress the model does not fully succeed in predicting the behavior of platelet deposition over the domain length. However, an analogous trend is found in the Hosseinzadegan and Tafti model [51] which, like ours, is based on the Sorensen et al. study.

The thrombus growth modeling proposed in the present work is very simple. Nevertheless, the thrombus shape observed and the distribution of the activated platelets over the domain (see figure 4.7) are consistent with those observed in previous experimental studies, for instance by Leiderman and Fogelson [70]. Furthermore, the proposed thrombus size formulation (Eq.4.29) allows us to take into account thrombi of different compositions by simply varying the volume blood cell multiplication factor.

On the other hand, the thrombus shape observed in validating the shear gradient related part of the model does not reproduce the experimentally observed one (see figure 4.9). The wedge shape of the thrombus observed here may be related to numerical instabilities. The platelet aggregation induced by shear deceleration is directly proportional to the shear-gradient $\frac{\partial \dot{\gamma}}{\partial x}$, which, resulting from two successive numerical differentiations of the solution of the flow field, can have a noisy output signal. More smooth shear gradient results were obtained by increasing the element order of the fluid dynamics discretization, using P2+P1 elements (P2 for the velocity, and P1 for the pressure). This led to a higher demand on computational resources due to the increase in number of degrees of freedom. The model requires an improvement if precise determination of the shape of the platelet aggregate is desired. Nevertheless, the model has succeeded in predicting the magnitude and position of the maximum aggregate size in the case of a stenosis. This information is fundamental in optimizing the design of the flow path of an endovascular device.

The implementation of the role of the shear gradients, which was revealed to be fundamental in thrombus formation [83], is the main novelty of this model. Figures 4.12 and 4.11 confirm the Nesbitt et al. results underlining that if shear gradients occur, then thrombus formation and evolution is driven principally by the mechanical platelet activation and aggregation rather than chemical ones, regardless of whether the flow is pulsatile or steady.

A thrombus formation model that takes into account the chemical and mechanical platelet activation and aggregation and the most important physiological aspects of the problem is computationally very expensive. In this respect, some simplifications were adopted to render the computations tractable. Regarding the geometry, the domains considered are extremely simplified. A step forward would be the implementation of more realistic geometries.

The fibrin formation and its role in the stabilization of the platelet aggregate was

not implemented. However, the thrombotic deposition encountered in cardiovascular devices, whose evaluation is the ultimate goal of this model, is characterized by less fibrin involvement than encountered in low-shear venous thrombosis [114].

Thromboembolism is another feature that was not taken into account in this work. High shear stress has a dual role on thrombus formation and evolution: on the one hand, high shear stresses promote platelet activation, but on the other hand induce the disaggregation of a platelet plug. In the developed model, the thrombus continues to grow until it occludes the blood vessel and the blood flow stops. In the perspective of predicting thrombotic deposition and occlusions, this aspect may make our model very conservative.

Blood is regarded as a Newtonian fluid, this assumption, in case of arterial flow, that is our primary interest, is a good approximation of the real rheological behavior of blood. However, in case of in irregular geometries, such as stenoses, this is a quite strong assumption. It is worth to point out that, in such cases, the shear rate may be locally low, for istance in the recirculation zone. Some previous thrombus formation models, such as [15] [11], considered the shear thinning blood behavior. Choi and Barakat [22] investigated the impact of non-Newtonian behavior on the blood flow field over a two-dimensional backward facing step, representing flow disturbance. They found that spatial gradients of shear stress tend to be larger for the non-Newtonian fluid. In this perspective, our model may tend to underestimate the thrombotic deposition. However, this aspect would compensate for the neglecting of the possibility of thromboembolism.

Despite its simplicity and its limitations, the present work represents an important attempt to couple different key aspects of the thrombus formation and evolution process: chemical and mechanical platelet activation and aggregation, the influence of thrombus growth on the flow field and platelet re-circulation and production.

The model promises to serve as a useful tool in helping to predict thrombotic deposition in the cardiovascular system and it may be particularly interesting, from a clinical point of view, to predict thrombus formation in the pathological situations involving blood flow disturbances, such as implanted endovascular devices, stenosis generated by advanced atherosclerotic disease or restenosis due to stent implantation.

Chapter 5

Conclusions

In this thesis, the potential of the mathematical fluid dynamical modeling in biomedical field was exploited.

Three mathematical models, one analytical and two computational, were described. Three different biomedical issues, in which the fluid dynamics of the system plays a fundamental role, were modeled: i) the fluid-structure interactions between cerebro-spinal fluid pulsatility and the spinal cord (analytical modeling); ii) Drug enhanced dispersion in the subarachnoid space (numerical modeling); and iii) the thrombus formation and evolution in the cardiovascular system (numerical modeling).

The results obtained in the present thesis confirm that fluid-dynamic based mathematical models are useful tools in many respects: i) Investigate the pathogenesis of diseases that is still uncertain; ii) Give quantitative informations for protocols and facilities that are not optimized yet; iii) Optimize the design of internal devices.

The presented models represent a first approach and present several shortcomings that can be improved. All three models have been implemented and developed on very simplified domains and neglect some physiological processes and anatomical details. Nevertheless, they have provided some promising outcomes.

The developed analytical spinal cord-cerebrospinal fluid interaction model has shed light on scenarios that may induce the occurrence of Syringomyelia. It was seen how the deviation from the physiological values of the Young modulus of the spinal cord – due, for instance, to pia mater injuries –, the capillary pressures at the SC-SAS interface and the permeability of blood networks can lead to syrinx formation.

The computational model of drug dispersion has allowed to quantitatively estimate the drug effective diffusivity, a feature that can aid the tuning of intrathecal delivery protocols.

Finally, the comprehensive thrombus formation model has provided a quantification tool for the thrombotic deposition. To our knowledge, it includes, for the first

time, the crucial pro-thrombogenetic role of spatial shear gradients, becoming particularly interesting in the pathological scenarios within which flow disturbances occur. This tool could prove helpful for biomedical engineers in predicting the thrombus formation and evolution, as a consequence of flow disturbances induced by the implantation of cardiovascular devices as well as for clinicians in predicting possible thrombotic deposition in an atherosclerotic patients.

If on the one hand, the reported models have delivered interesting outcomes, on the other hand they can lend themselves to equally interesting developments. For instance, a possible development of the fluid-structure interaction model is the stability analysis of the governing equations around the solutions herein presented (or their polynomial approximation) in the spirit of the work by Toro et al. [126]. This would allow one to assess the parametric conditions for the growth of syrinx formation. In that case, the assumption of no mass exchange between the fluid networks should be relaxed.

The drug dispersion model lend itself to the implementation of a 3D subject-specific SAS domain based on detailed MRI imaging [106], in order to quantify the role of the fine structure within the SAS and the morphological irregularity of meninges – SAS walls roughness – in the estimation of the drug effective diffusivity.

The implementation of more realistic domains that can represent thoroughly the blood flow within and around endovascular devices and the embedding of hemostatic and hemodynamic features that were neglected, are compelling developments of the thrombus formation model. Implementing the shear thinning behavior of blood would allow to estimate more accurately the shear gradient and consequently the thrombotic deposition and to better simulate recirculation zones characterized by locally low shear rate. At the same time, the embedding of the shear thinning rheological behavior of blood as well the role of fibrin stabilization would make the model suitable to evaluate thrombus aggregate size in case of arterial thrombosis but also vein thrombosis. Finally an experimental campaign *ad hoc* would be a beneficial development in order to validate the role of the shear micro-gradients compared to the chemical one and to calibrate more accurately some parameters of the model, such as the scaling term of the thrombus size h or the scaling factor of the mechanical aggregation (Eq. (4.32)-(4.33)).

In conclusion, in biomedical issues fluid dynamics is often a fundamental aspect to investigate. Thus, a multidisciplinary approach is essential to study and solve some biomedical issues. In this framework, the fluid dynamic modeling of biological fluids is a very important methodology that can help to achieve different goals of the biomedical research, from understanding of pathophysiology of developing and progressing diseases to establish novel treatment modalities and devices design.

Appendix A

Dimensional boundary conditions in the spinal cord and derivation of the kinematic condition

For the reader convenience, the dimensional form of the boundary conditions for the spinal cord–considered in modeling the fluid-structure interactions between cerebro-spinal fluid and the spinal cord–are here reported. At the interface between the SAS and the SC (i.e., $r=1+\zeta$) they read

$$2G\frac{\partial u_r}{\partial r} + \frac{2Gv}{1-2v}\left(\frac{\partial u_r}{\partial r} + \frac{u_r}{r}\right) - \alpha \sum_{i=c,v,e} p^i = 2\mu\frac{\partial v_r}{\partial r} - P_0, \tag{A.1}$$

$$G\frac{\partial u_r}{\partial x} = \mu\left(\frac{\partial v_r}{\partial x} + \frac{\partial v_x}{\partial r}\right), \tag{A.2}$$

$$\{p^v, p^c\} = \{\bar{P}_v, \bar{P}_c\} + \{P_v, P_c\} \cdot e^{i(kx-\omega t)}, \tag{A.3}$$

$$v_x\frac{\partial \zeta}{\partial x} - v_r + \phi k\left(\frac{\partial p^e}{\partial x}\frac{\partial \zeta}{\partial x} - \frac{\partial p^e}{\partial r}\right) = (1-\phi)\frac{\partial \zeta}{\partial t}, \tag{A.4}$$

At the interface between the SC and the CC (i.e., $r=r_i$) we have

$$2G\frac{\partial u_r}{\partial r} + \frac{G}{1-2v}\left(\frac{\partial u_r}{\partial r} + \frac{\partial u_x}{\partial x} + \frac{u_r}{r}\right) - \alpha \sum_{i=c,v,e} p^i + \bar{P}_e = 0, \tag{A.5}$$

$$u_r = \frac{\partial p^c}{\partial r} = \frac{\partial p^v}{\partial r} = 0. \tag{A.6}$$

The kinematic condition A.4 was derived from a mass balance in a small poro-elastic volume across the interface, by virtue of Darcy's law. The kinematic condition links the deformation of the SC-SAS interface to the other unknowns.

The mass balance for an infinitesimal volume across the (porous) solid-fluid interface read

$$\rho\left(\vec{v}_{csf} \cdot \vec{n} - \vec{\zeta} \cdot \vec{n}\right) = \rho\phi\left(\vec{v^e} \cdot \vec{n} - \vec{\zeta} \cdot \vec{n}\right), \tag{A.7}$$

where $\vec{v}_{csf}=\{v_x, v_r\}$ is the CSF velocity vector from the side of the subarachnoid space, $\vec{\zeta}$ is the deformation velocity of the interface, $\vec{n}$ is the normal versor at the interface and $\vec{v^e}$ is the CSF velocity inside the spinal cord, which Darcy's law reads $v^e=-\frac{\kappa^e}{\mu^e}\nabla p^e$. After developing the scalar products in (A.7), the kinematic condition (A.4) is recovered, corresponding to equation (2.28) in dimensionless form.

Appendix B

Coefficients of the solutions expression in the fluid-structure interaction model

In the solutions of the flow field and the capillary and venous pressures of the fluid-structure interaction model, equations (2.45),(2.46),(2.50) the coefficients read

$$
\begin{align}
c_0 &= \Gamma^2(Y_0(i\Gamma)I_0(\Psi_1) - I_0(\Gamma)Y_0(i\Psi_1)), \tag{B.1}\\
c_1 &= (Y_0(i\Psi_1) - Y_0(i\Gamma)), \tag{B.2}\\
c_2 &= (I_0(\Psi_1)Y_0(i\Gamma) - I_0[\Gamma]Y_0(i\Psi_1)), \tag{B.3}\\
c_3 &= 2i(1+h)Y_1[i\Psi_1] \tag{B.4}\\
c_4 &= (\eta_3 + i\eta_4 k^2)(\,_0\tilde{F}_1(;1;\Psi_3^2/4)Y_1(-iR_i\Psi_3) + iY_0(-i\Psi_3)I_1(R_i\Psi_3)), \tag{B.5}\\
c_5 &= -2i\Psi\alpha\delta Y_0[-i\Psi_3], \tag{B.6}\\
c_6^{c,v} &= (2\alpha\Psi\delta + \eta_3 P_{c,v} + i\eta_4 k^2 P_{c,v}), \tag{B.7}\\
c_7 &= -2\Psi\alpha\delta\,_0\tilde{F}_1(;1;\Psi_3^2/4), \tag{B.8}
\end{align}
$$

where $\Psi = \eta_5\left[\frac{i\hat{v}_x'}{\delta^2 k} + (1-h)\hat{v}_r - v_r'\right]_{z_e=0}$ and $_0\tilde{F}_1(;1;\Psi_3^2/4)$ is the confluent hypergeometric function.

Appendix C

Parameters of the thrombus growth model

In this section the values of the thrombus growth model parameters are reported. The following parameters characterize the part of the model related to chemical platelet activation and aggregation and refer to the Sorensen et al. [114] work.

Table C.1: Physiological values of the parameters used in the chemical platelet activation and aggregation part of the model.

Parameter	Value	Unit
λ_{ADP}	$2.4 \cdot 10^{-8}$	nmol PLT^{-1}
$k_{1,TxA2}$	0.0161	s^{-1}
$s_{p,TxA2}$	$9.5 \cdot 10^{-12}$	nmol PLT^{-1} s^{-1}
$k_{1,T}$	13.33	s^{-1}
K_{AT}	0.10	μM
K_T	$3.5 \cdot 10^{-2}$	μM
α	1	[-]
θ	1	[-]
β	$9.11 \cdot 10^{-3}$	nmol U^{-1}
ϕ_{at}	$3.69 \cdot 10^{-9}$	U PLT^{-1}s^{-1} (μM PT)$^{-1}$
ϕ_{rt}	$6.50 \cdot 10^{-10}$	U PLT^{-1}s^{-1} (μM PT)$^{-1}$
t_{act}	1	s
$[H]$	2	μM
M_∞	$7 \cdot 10^6$	PLT cm^{-2}

Bibliography

[1] Rutherford Aris. "On the dispersion of a solute in a fluid flowing through a tube". In: *Proceedings of the Royal Society of London A: mathematical, physical and engineering sciences.* Vol. 235. 1200. The Royal Society. 1956, pp. 67–77.

[2] Evgenia S Babushkina et al. "Continuous modeling of arterial platelet thrombus formation using a spatial adsorption equation". In: *PLoS One* 10.10 (2015), e0141068.

[3] Oguz K Baskurt and Herbert J Meiselman. "Blood rheology and hemodynamics". In: *Seminars in thrombosis and hemostasis.* Vol. 29. 05. Copyright© 2003 by Thieme Medical Publishers, Inc., 333 Seventh Avenue, New . . . 2003, pp. 435–450.

[4] Ernnie Illyani Basri et al. "Computational Fluid Dynamics Study in Biomedical Applications: A Review". In: *International Journal of Fluids and Heat Transfer* 1.2 (2016).

[5] B Battal et al. "Cerebrospinal fluid flow imaging by using phase-contrast MR technique". In: *The British journal of radiology* 84.1004 (2011), pp. 758–765.

[6] K Berkouk, PW Carpenter, and AD Lucey. "Pressure wave propagation in fluid-filled co-axial elastic tubes part 1: basic theory". In: *Trans-Am. Soc. Mech. Eng. J. Bio. Eng.* 125.6 (2003), pp. 852–856. DOI: 10.1115/1.1634280.

[7] Christopher D Bertram. "A numerical investigation of waves propagating in the spinal cord and subarachnoid space in the presence of a syrinx". In: *J. Fluid Struct.* 25.7 (2009), pp. 1189–1205. DOI: 10.1016/j.jfluidstructs.2009.06.008.

[8] Christopher D Bertram. "Evaluation by fluid/structure-interaction spinal-cord simulation of the effects of subarachnoid-space stenosis on an adjacent syrinx". In: *J. Biomech. Eng.* 132.6 (2010), p. 061009. DOI: 10.1115/1.4001165.

[9] Christopher D Bertram, Andrew R Brodbelt, and Marcus A Stoodley. "The origins of syringomyelia: numerical models of fluid/structure interactions in the spinal cord". In: *J. Biomech. Eng.* 127.7 (2005), pp. 1099–1109.

[10] Christopher D Bertram and Matthias Heil. "A poroelastic fluid/structure-interaction model of cerebrospinal fluid dynamics in the cord with syringomyelia and adjacent subarachnoid-space stenosis". In: *J.Biomech. Eng.* 139.1 (2017). DOI: 10.1115/1.4034657.

[11] Jacopo Biasetti et al. "An integrated fluid-chemical model toward modeling the formation of intra-luminal thrombus in abdominal aortic aneurysms". In: *Frontiers in physiology* 3 (2012), p. 266.

[12] Maurice A Biot. "General theory of three-dimensional consolidation". In: *J. Appl. Phys.* 12.2 (1941), pp. 155–164. DOI: 10.1063/1.1712886.

[13] Maurice A Biot and DG Willis. "The elastic coeffcients of the theory of consolidation". In: *J. appl. Mech* 24 (1957), pp. 594–601.

[14] Danny Bluestein. "Utilizing Computational Fluid Dynamics in cardiovascular engineering and medicine—What you need to know. Its translation to the clinic/bedside". In: *Artificial organs* 41.2 (2017), p. 117.

[15] Tomáš Bodnár and Adélia Sequeira. "Numerical simulation of the coagulation dynamics of blood". In: *Computational and Mathematical Methods in Medicine* 9.2 (2008), pp. 83–104.

[16] Clarence H Brown et al. "Morphological, biochemical, and functional changes in human platelets subjected to shear stress". In: *The Journal of laboratory and clinical medicine* 86.3 (1975), pp. 462–471.

[17] E. Buchser et al. "Efficacy of intrathecal bupivacaine: How important is the flow rate?" In: *Pain Med.* 5 (2012), pp. 248–252.

[18] James R Byrnes and Alisa S Wolberg. "Red blood cells in thrombosis". In: *Blood, The Journal of the American Society of Hematology* 130.16 (2017), pp. 1795–1799.

[19] Francisca Carvalhal et al. "Antithrombotics from the Sea: Polysaccharides and Beyond". In: *Marine drugs* 17.3 (2019), p. 170.

[20] Shaokoon Cheng et al. "Effects of fluid structure interaction in a three dimensional model of the spinal subarachnoid space". In: *J. Biomech.* 47.11 (2014), pp. 2826–2830. DOI: 10.1016/j.jbiomech.2014.04.027.

[21] W-L Chien, H Rising, and JM Ottino. "Laminar mixing and chaotic mixing in several cavity flows". In: *Journal of Fluid Mechanics* 170 (1986), pp. 355–377.

[22] Hyo Won Choi and Abdul I Barakat. "Numerical study of the impact of non-Newtonian blood behavior on flow over a two-dimensional backward facing step". In: *Biorheology* 42.6 (2005), pp. 493–509.

[23] Srdjan Cirovic. "A coaxial tube model of the cerebrospinal fluid pulse propagation in the spinal column". In: *J. Biomech. Eng.* 131.2 (2009), p. 021008. DOI: 10.1115/1.3005159.

[24] Srdjan Cirovic and Minsuok Kim. "A one-dimensional model of the spinal cerebrospinal-fluid compartment". In: *J. Biomech. Eng.* 134.2 (2012), p. 021005. DOI: 10.1115/1.4005853.

[25] MW Collins, Giuseppe Pontrelli, and MA Atherton. *Wall-fluid interactions in physiological flows.* Vol. 6. WIT press, 2004.

[26] Fiorenzo Conti, Piero Paolo Battaglini, and Edoardo Mora. *Fisiologia médica.* McGraw-Hill, 2010.

[27] H Davson, K Welch, and MB Segal. "The secretion of the cerebrospinal fluid". In: *The physiology and pathophysiology of the cerebrospinal fluid* 201 (1987), pp. 73–83.

[28] Stefanie Dimmeler. "Cardiovascular disease review series". In: *EMBO molecular medicine* 3.12 (2011), pp. 697–697.

[29] GF Dommisse. "The arteries, arterioles, and capillaries of the spinal cord. Surgical guidelines in the prevention of postoperative paraplegia." In: *Ann. R. Coll. Surg. Engl.* 62.5 (1980), p. 369.

[30] Novak SJ Elliott et al. "Fluid–structure interactions in a cylindrical layered wave guide with application in the spinal column to syringomyelia". In: *J. Fluid Struct.* 70 (2017), pp. 464–499. DOI: 10.1016/j.jfluidstructs.2016.11.007.

[31] NSJ Elliott. "Syrinx fluid transport: modeling pressure-wave-induced flux across the spinal pial membrane". In: *J. Biomech. Eng.* 134.3 (2012). DOI: 10.1115/1.4005849.

[32] NSJ Elliott et al. "Syringomyelia: a review of the biomechanics". In: *J. Fluid Struct.* 40 (2013), pp. 1–24. DOI: 10.1016/j.jfluidstructs.2013.01.010.

[33] Graham Flint and Clare Rusbridge. *Syringomyelia: A Disorder of CSF Circulation.* Springer, 2014.

[34] AARON L Fogelson. "Aggregation: Mechanical Properties and Chemically-Induced Phase Transitions". In: *Fluid Dynamics in Biology: Proceedings of an AMS-IMS-SIAM Joint Summer Research Conference Held July 6-12, 1991 with Support from the National Science Foundation and NASA Headquarters.* Vol. 141. American Mathematical Soc. 1993, p. 279.

[35] Aaron L Fogelson. "Continuum models of platelet aggregation: formulation and mechanical properties". In: *SIAM Journal on Applied Mathematics* 52.4 (1992), pp. 1089–1110.

[36] Andrew J Gale. "Continuing education course# 2: current understanding of hemostasis". In: *Toxicologic pathology* 39.1 (2011), pp. 273–280.

[37] Amy E Geddis and Kenneth Kaushansky. "The root of platelet production". In: *Science* 317.5845 (2007), pp. 1689–1691.

[38] Paul D Goodman et al. "Computational model of device-induced thrombosis and thromboembolism". In: *Annals of biomedical engineering* 33.6 (2005), pp. 780–797.

[39] Vijay Govindarajan et al. "Computational study of thrombus formation and clotting factor effects under venous flow conditions". In: *Biophysical journal* 110.8 (2016), pp. 1869–1885.

[40] Dan Greitz. "Unraveling the riddle of syringomyelia". In: *Neurosurg. Rev.* 29.4 (2006), pp. 251–264. DOI: `10.1007/s10143-006-0029-5`.

[41] Andrea Guala. "Mathematical modelling of cardiovascular fluid mechanics: physiology, pathology and clinical practice". PhD thesis. Ph. D Thesis in Engineering for Natural and Built Environment-XXVII cycle, 2015.

[42] Per Thomas Haga et al. "A numerical investigation of intrathecal isobaric drug dispersion within the cervical subarachnoid space". In: *PloS one* 12.3 (2017), e0173680.

[43] Catherine E Hagan, Brad Bolon, and C Dirk Keene. "Nervous system". In: *Comparative Anatomy and Histology.* Elsevier, 2012, pp. 339–394.

[44] LA Harker. "The kinetics of platelet production and destruction in man." In: *Clinics in haematology* 6.3 (1977), pp. 671–693.

[45] Herre W Heetla et al. "Clinical relevance of pharmacological and physiological data in intrathecal baclofen therapy". In: *Archives of physical medicine and rehabilitation* 95.11 (2014), pp. 2199–2206.

[46] Matthias Heil and Christopher D Bertram. "A poroelastic fluid–structure interaction model of syringomyelia". In: *J. Fluid Mech.* 809 (2016), pp. 360–389. DOI: `10.1017/jfm.2016.669`.

[47] J David Hellums. "1993 Whitaker Lecture: biorheology in thrombosis research". In: *Annals of biomedical engineering* 22.5 (1994), pp. 445–455.

[48] S Hentschel et al. "Characterization of cyclic CSF flow in the foramen magnum and upper cervical spinal canal with MR flow imaging and computational fluid dynamics". In: *Am. J. Neuroradiol.* 31.6 (2010), pp. 997–1002. DOI: `10.3174/ajnr.A1995`.

[49]   HDM Hettiarachchi et al. "The effect of pulsatile flow on intrathecal drug delivery in the spinal canal". In: *Ann. Biomed. Eng.* 39.10 (2011), p. 2592. DOI: 10.1007/s10439-011-0346-x.

[50]   Stephen B Hladky and Margery A Barrand. "Mechanisms of fluid movement into, through and out of the brain: evaluation of the evidence". In: *Fluids Barriers CNS* 11.1 (2014), p. 26. DOI: 10.1186/2045-8118-11-26.

[51]   Hamid Hosseinzadegan and Danesh K Tafti. "Modeling thrombus formation and growth". In: *Biotechnology and bioengineering* 114.10 (2017), pp. 2154–2172.

[52]   Ying Hsu et al. "The frequency and magnitude of cerebrospinal fluid pulsations influence intrathecal drug distribution: key factors for interpatient variability". In: *Anesth. Analg.* 115.2 (2012), pp. 386–394. DOI: 10.1213/ANE.0b013e3182536211.

[53]   Jeffrey A Hubbell and Larry V McIntire. "Visualization and analysis of mural thrombogenesis on collagen, polyurethane and nylon". In: *Biomaterials* 7.5 (1986), pp. 354–363.

[54]   Trevor Huff, Prasanna Tadi, and Matthew Varacallo. "Neuroanatomy, Cerebrospinal Fluid". In: (2019).

[55]   Yongfei Jiang, Jun Zhang, and Wanhua Zhao. "Effects of the inlet conditions and blood models on accurate prediction of hemodynamics in the stented coronary arteries". In: *AIP Advances* 5.5 (2015), p. 057109.

[56]   A Jordan et al. "The effects of margination and red cell augmented platelet diffusivity on platelet adhesion in complex flow". In: *Biorheology* 41.5 (2004), pp. 641–653.

[57]   Takashi Kameyama, Yoshio Hashizume, and Gen Sobue. "Morphologic features of the normal human cadaveric spinal cord". In: *Spine* 21.11 (1996), pp. 1285–1290.

[58]   Eric R Kandel et al. *Principles of neural science*. Vol. 4. McGraw-hill New York, 2000.

[59]   K. H. Keller. "Effect of fluid shear on mass transport in flowing blood". In: *Fed. Proc.* 30 (1971), pp. 1591–1599.

[60]   HE Killer et al. "Architecture of arachnoid trabeculae, pillars, and septa in the subarachnoid space of the human optic nerve: anatomy and clinical considerations". In: *British Journal of Ophthalmology* 87.6 (2003), pp. 777–781.

[61]   HY Ko et al. "Gross quantitative measurements of spinal cord segments in human". In: *Spinal cord* 42.1 (2004), p. 35.

[62] MH Kroll. "Hellums JD, McIntire LV, Schafer AI, Moake JL". In: *Platelets and shear stress. Blood* 88 (1996), pp. 1525–1541.

[63] David J Kuter. "The physiology of platelet production". In: *Stem Cells* 14.S1 (1996), pp. 88–101.

[64] Andreas Kuttler et al. "Understanding pharmacokinetics using realistic computational models of fluid dynamics: biosimulation of drug distribution within the CSF space for intrathecal drugs". In: *Journal of pharmacokinetics and pharmacodynamics* 37.6 (2010), pp. 629–644.

[65] JJ Lawrence et al. "On the dispersion of a drug delivered intrathecally in the spinal canal". In: *J. Fluid Mech.* 861 (2019), pp. 679–720.

[66] Byoung-Kwon Lee. "Computational fluid dynamics in cardiovascular disease". In: *Korean circulation journal* 41.8 (2011), pp. 423–430.

[67] Sarah CM Lee and Christian J Lueck. "Cerebrospinal fluid pressure in adults". In: *Neuro-Ophthalmol.* 34.3 (2014), pp. 278–283. DOI: 10.1097/WNO.0000000000000155.

[68] Y.C. Lee et al. "The necessity of intrathecal chemotherapy for the treatment of breast cancer patients with leptomeningeal metastasis: a systematic review and pooled analysis". In: *Curr. Probl. Cancer* 41 (2017), pp. 355–370.

[69] Yen-Chien Lee et al. "The necessity of intrathecal chemotherapy for the treatment of breast cancer patients with leptomeningeal metastasis: A systematic review and pooled analysis". In: *Current problems in cancer* 41.5 (2017), pp. 355–370.

[70] Karin Leiderman and Aaron L Fogelson. "Grow with the flow: a spatial–temporal model of platelet deposition and blood coagulation under flow". In: *Mathematical medicine and biology: a journal of the IMA* 28.1 (2011), pp. 47–84.

[71] Torsten Liem and Ralf Vogt. "Membranous structures within the cranial bowl and intraspinal space". In: *Fascia: The Tensional Network of the Human Body.* Elsevier, 2012, pp. 57–65. DOI: 10.1016/B978-0-7020-3425-1.00043-X.

[72] Andreas A Linninger et al. "A mathematical model of blood, cerebrospinal fluid and brain dynamics". In: *J. Math. Biol.* 59.6 (2009), pp. 729–759.

[73] Andreas A Linninger et al. "Cerebrospinal fluid mechanics and its coupling to cerebrovascular dynamics". In: *Annu. Rev. Fluid Mech.* 48 (2016), pp. 219–257. DOI: 10.1146/annurev-fluid-122414-034321.

[74] Francis Loth, M Atif Yardimci, and Noam Alperin. "Hydrodynamic modeling of cerebrospinal fluid motion within the spinal cavity". In: *J. Biomech. Eng.* 123.1 (2001), pp. 71–79. DOI: 10.1115/1.1336144.

[75] Nigel Mackman. "The role of tissue factor and factor VIIa in hemostasis". In: *Anesthesia and analgesia* 108.5 (2009), p. 1447.

[76] Diana Massai et al. "Shear-induced platelet activation and its relationship with blood flow topology in a numerical model of stenosed carotid bifurcation". In: *European Journal of Mechanics-B/Fluids* 35 (2012), pp. 92–101.

[77] Edward L Mazuchowski, Lawrence E Thibault, et al. "Biomechanical properties of the human spinal cord and pia mater". In: *Summer Bioengineering Conference, Sonesta Beach Resort, Key Biscayne, FL, USA*. 2003.

[78] Claudia Menichini and Xiao Yun Xu. "Mathematical modeling of thrombus formation in idealized models of aortic dissection: initial findings and potential applications". In: *Journal of mathematical biology* 73.5 (2016), pp. 1205–1226.

[79] Bahram Mokri. "The Monro–Kellie hypothesis: applications in CSF volume depletion". In: *Neurology* 56.12 (2001), pp. 1746–1748.

[80] Martin M Mortazavi et al. "Subarachnoid trabeculae: a comprehensive review of their embryology, histology, morphology, and surgical significance". In: *World neurosurgery* 111 (2018), pp. 279–290.

[81] Elie Nader et al. "Blood Rheology: Key parameters, impact on blood flow, role in sickle cell disease and effects of exercise". In: *Frontiers in physiology* 10 (2019), p. 1329.

[82] Radboud Michael Nelissen. *Fluid mechanics of intrathecal drug delivery.* Tech. rep. EPFL, 2008.

[83] Warwick S Nesbitt et al. "A shear gradient–dependent platelet aggregation mechanism drives thrombus formation". In: *Nature medicine* 15.6 (2009), p. 665.

[84] W.W Nichols and M.F O'Rourke. *McDonald's blood flow in arteries - Fifth edition.* Hodder Arnold, 2005.

[85] Antal Nógrádi and Gerta Vrbová. "Anatomy and physiology of the spinal cord". In: *Transplantation of neural tissue into the spinal cord.* Springer, 2006, pp. 1–23.

[86] MM Overd and SC Generalis. "Laminar fluid chaotic mixing in three-dimensional continuous flow domains". In: *International Polymer Processing* 16.4 (2001), pp. 368–375.

[87] Soroush Heidari Pahlavian et al. "The impact of spinal cord nerve roots and denticulate ligaments on cerebrospinal fluid dynamics in the cervical spine". In: *PloS one* 9.4 (2014), e91888. DOI: `10.1371/journal.pone.0091888`.

[88] Sanjeev Palta, Richa Saroa, and Anshu Palta. "Overview of the coagulation system". In: *Indian journal of anaesthesia* 58.5 (2014), p. 515.

[89] Ian Peate and Lisa Bennett-Long. "Tests, scans and investigations 1. Blood tests". In: *British Journal of Healthcare Assistants* 10.8 (2016), pp. 370–373.

[90] Timothy J Pedley and XY Luo. *Fluid mechanics of large blood vessels.* Shaanxi People's Press, 1995.

[91] Mercy Halleluyah Periayah, Ahmad Sukari Halim, and Arman Zaharil Mat Saad. "Mechanism action of platelets and crucial blood coagulation pathways in hemostasis". In: *International journal of hematology-oncology and stem cell research* 11.4 (2017), p. 319.

[92] G Pizzichelli et al. "Numerical study of intrathecal drug delivery to a permeable spinal cord: effect of catheter position and angle". In: *Comput. Methods Biomech. Biomed. En.g Imaging Vis.* 20.15 (2017), pp. 1599–1608.

[93] Giuseppe Pontrelli and Enrico Rossoni. "Numerical modelling of the pressure wave propagation in the arterial flow". In: *International journal for numerical methods in fluids* 43.6-7 (2003), pp. 651–671.

[94] Milan Radojicic, Gabriel Nistor, and Hans S Keiastead. "Ascending central canal dilation and progressive ependymal disruption in a contusion model of rodent chronic spinal cord injury". In: *BMC neurology* 7.1 (2007), p. 30. DOI: 10.1186/1471-2377-7-30.

[95] Seshadri Raju. "Chapter 2 - Venous Hemodynamics". In: *Atlas of Endovascular Venous Surgery.* Ed. by Jose I. Almeida. Second. Philadelphia, 2019, pp. 21–36. ISBN: 978-0-323-51139-1. DOI: 10.1016/B978-0-323-51139-1.00002-4. URL: http://www.sciencedirect.com/science/article/pii/B9780323511391000024.

[96] F. Remes et al. "Intraventricular and lumbar intrathecal administration of antibiotics in postneurosurgical patients with meningitis and/or ventriculitis in a serious clinical state." In: *J. Neurosurg.* 119 (2013), pp. 1596–1602.

[97] A Roldan et al. "Characterization of CSF hydrodynamics in the presence and absence of tonsillar ectopia by means of computational flow analysis". In: *Am. J. Neuroradiol.* 30.5 (2009), pp. 941–946. DOI: 10.3174/ajnr.A1489.

[98] L Ros et al. "Quantitative measurements of the spinal cord and canal by MR imaging and myelography". In: *Eur. Radiol.* 8.6 (1998), pp. 966–970.

[99] Oleksii S Rukhlenko et al. "Mathematical modeling of intravascular blood coagulation under wall shear stress". In: *PloS one* 10.7 (2015), e0134028.

[100] Rolando E Rumbaut and Perumal Thiagarajan. "Platelet-vessel wall interactions in hemostasis and thrombosis". In: *Synthesis Lectures on Integrated Systems Physiology: From Molecule to Function* 2.1 (2010), pp. 1–75.

[101]   Julie Sahler et al. "Platelet storage and transfusions: new concerns associated with an old therapy". In: *Drug Discovery Today: Disease Mechanisms* 8.1-2 (2011), e9–e14.

[102]   Kjell S Sakariassen et al. "Shear-induced platelet activation and platelet microparticle formation in native human blood". In: *Thrombosis research* 92.6 (1998), S33–S41.

[103]   Laurent Sakka, Guillaume Coll, and Jean Chazal. "Anatomy and physiology of cerebrospinal fluid". In: *European annals of otorhinolaryngology, head and neck diseases* 128.6 (2011), pp. 309–316.

[104]   Luca Salerno, Giulia Cardillo, and Carlo Camporeale. "Aris-Taylor dispersion in the subarachnoid space". In: *Phys. Rev. Fluids* 5 (4 Apr. 2020), p. 043102. DOI: 10.1103/PhysRevFluids.5.043102. URL: https://link.aps.org/doi/10.1103/PhysRevFluids.5.043102.

[105]   Clément Sanchez. "Athérosclérose : pathologies associées, prévention et traitements". In: 2017.

[106]   Lucas R Sass et al. "A 3D subject-specific model of the spinal subarachnoid space with anatomically realistic ventral and dorsal spinal cord nerve rootlets". In: *Fluids Barriers CNS* 14.1 (2017), p. 36.

[107]   Fabrice Schlegel. *Understanding Stabilization Methods.* 2014. URL: https://www.comsol.com/blogs/understanding-stabilization-methods (visited on 04/12/2020).

[108]   L Schmeltz and B Metzger. "Therapeutic Areas I: Central Nervous System, Pain, Metabolic Syndrome, Urology, Gastrointestinal and Cardiovascular". In: *Comprehensive Medicinal Chemistry II. Amsterdam: Elsevier Science* (2007).

[109]   Robert S. Schwartz and C. Lockard Conley. *Blood.* 2019. URL: https://www.britannica.com/science/blood-biochemistry (visited on 04/07/2020).

[110]   MB Segal. "Extracellular and cerebrospinal fluids". In: *J. Inherit. Metab. Dis.* 16.4 (1993), pp. 617–638. DOI: 10.1007/BF00711896.

[111]   Neal Shah and Devang Padalia. "Intrathecal Delivery System". In: *StatPearls [Internet].* StatPearls Publishing, 2019.

[112]   ANGELA C Shore, DEREK D Sandeman, and JOHN E Tooke. "Capillary pressure, pulse pressure amplitude, and pressure waveform in healthy volunteers". In: *Am. J. Physiol. Heart Circ. Physiol.* 268.1 (1995), H147–H154. DOI: 10.1152/ajpheart.1995.268.1.H147.

[113]   Howard S Smith et al. "Intrathecal drug delivery." In: *Pain physician* 11.2 Suppl (2008), S89–S104.

[114] Erik N Sorensen et al. "Computational simulation of platelet deposition and activation: I. Model development and properties". In: *Annals of biomedical engineering* 27.4 (1999), pp. 436–448.

[115] Erik N Sorensen et al. "Computational simulation of platelet deposition and activation: II. Results for Poiseuille Flow over Collagen." In: *Annals of biomedical engineering* 27.4 (1999), pp. 449–458.

[116] Harlan W Stockman. "Effect of anatomical fine structure on the dispersion of solutes in the spinal subarachnoid space". In: (2007).

[117] Harlan W Stockman. "Effect of anatomical fine structure on the flow of cerebrospinal fluid in the spinal subarachnoid space". In: (2006).

[118] Karen H Støverud et al. "Poro-elastic modeling of syringomyelia–a systematic study of the effects of pia mater, central canal, median fissure, white and gray matter on pressure wave propagation and fluid movement within the cervical spinal cord". In: *Comput. Methods Biomech. Biomed. Engin.* 19.6 (2016), pp. 686–698. DOI: `10.1080/10255842.2015.1058927`.

[119] Abraham D Stroock et al. "Chaotic mixer for microchannels". In: *Science* 295.5555 (2002), pp. 647–651.

[120] Laura L Swystun and Patricia C Liaw. "The role of leukocytes in thrombosis". In: *Blood, The Journal of the American Society of Hematology* 128.6 (2016), pp. 753–762.

[121] Marcela Szopos. "Mathematical modeling, analysis and simulations for fluid mechanics and their relevance to in silico medicine". PhD thesis. 2017.

[122] Kevin M Tangen et al. "CNS wide simulation of flow resistance and drug transport due to spinal microanatomy". In: *Journal of biomechanics* 48.10 (2015), pp. 2144–2154.

[123] Geoffrey Taylor. "Dispersion of soluble matter in solvent flowing slowly through a tube". In: *Proceedings of the Royal Society of London A: Mathematical, Physical and Engineering Sciences*. Vol. 219. 1137. The Royal Society. 1953, pp. 186–203.

[124] Robert William Teasell et al. "Syringomyelia Following Spinal Cord Injury". In: 2014.

[125] Karl Terzaghi. "Theory of consolidation". In: *Theoretical Soil Mechanics* (1943), pp. 265–296. DOI: `10.1002/9780470172766.ch13`.

[126] Eleuterio F. Toro et al. "A Computational Model for the Dynamics of Cerebrospinal Fluid in the Spinal Subarachnoid Space". In: *J. Biomech. Eng.* 141.1 (Oct. 2018). 011004. ISSN: 0148-0731. DOI: 10.1115/1.4041551. eprint: https://asmedigitalcollection.asme.org/biomechanical/article-pdf/141/1/011004/6098610/bio_141_01_011004.pdf. URL: https://doi.org/10.1115/1.4041551.

[127] B Tully and Yiannis Ventikos. "Cerebral water transport using multiple-network poroelastic theory: application to normal pressure hydrocephalus". In: *J. Fluid Mech.* 667 (2011), pp. 188–215. DOI: 10.1017/S0022112010004428.

[128] Søren Vedel and Henrik Bruus. "Transient Taylor–Aris dispersion for time-dependent flows in straight channels". In: *J. Fluid Mech.* 691 (2012), pp. 95–122.

[129] Søren Vedel, Emil Hovad, and Henrik Bruus. "Time-dependent Taylor–Aris dispersion of an initial point concentration". In: *J. Fluid Mech.* 752 (2014), pp. 107–122.

[130] WR Wagner and JA Hubbell. "Local thrombin synthesis and fibrin formation in an in vitro thrombosis model result in platelet recruitment and thrombus stabilization on collagen in heparinized blood." In: *The Journal of laboratory and clinical medicine* 116.5 (1990), pp. 636–650.

[131] M. Wallace and T.L. Yaksh. "Characteristics of distribution of morphine and metabolites in cerebrospinal fluid and plasma with chronic intrathecal morphine infusion in humans". In: *Anesth. Analg.* 115 (2012), pp. 797–804.

[132] Nien-Tzu Wang and Aaron L Fogelson. "Computational methods for continuum models of platelet aggregation". In: *Journal of Computational Physics* 151.2 (1999), pp. 649–675.

[133] Richa Wardhan and Kirk Shelley. "Peripheral venous pressure waveform". In: *Curr. Opin. Anesthesiol.* 22.6 (2009), pp. 814–821. DOI: 10.1097/ACO.0b013e328332a343..

[134] EJ Watson. "Diffusion in oscillatory pipe flow". In: *J. Fluid Mech.* 133 (1983), pp. 233–244.

[135] John R Womersley. "XXIV. Oscillatory motion of a viscous liquid in a thin-walled elastic tube—I: The linear approximation for long waves". In: *The London, Edinburgh, and Dublin Philosophical Magazine and Journal of Science* 46.373 (1955), pp. 199–221.

[136] David M Wootton et al. "A mechanistic model of acute platelet accumulation in thrombogenic stenoses". In: *Annals of biomedical engineering* 29.4 (2001), pp. 321–329.

[137] Ben LC Wright, James TF Lai, and Alexandra J Sinclair. "Cerebrospinal fluid and lumbar puncture: a practical review". In: *Journal of neurology* 259.8 (2012), pp. 1530–1545.

[138] Wei-Tao Wu et al. "Multi-constituent simulation of thrombus deposition". In: *Scientific reports* 7.1 (2017), pp. 1–16.

[139] David H. Yawn. *Plasma.* 2017. URL: https://www.britannica.com/science/plasma-biology (visited on 04/06/2020).

[140] Alireza Yazdani et al. "A general shear-dependent model for thrombus formation". In: *PLoS computational biology* 13.1 (2017), e1005291.

[141] Theresia I Yiallourou et al. "Comparison of 4D phase-contrast MRI flow measurements to computational fluid dynamics simulations of cerebrospinal fluid motion in the cervical spine". In: *PloS one* 7.12 (2012), e52284. DOI: 10.1371/journal.pone.0052284.

[142] Mair Zamir and RS Budwig. "Physics of pulsatile flow". In: *Appl. Mech. Rev.* 55.2 (2002), B35–B35. DOI: 10.1115/1.1451229.

[143] Olgierd Cecil Zienkiewicz et al. "Static and dynamic behaviour of soils: a rational approach to quantitative solutions. I. Fully saturated problems". In: *Proc. R. Soc. Lond.* 429.1877 (1990), pp. 285–309. DOI: 10.1098/rspa.1990.0061.

Scientific Contributions

Pubblications

- L. Salerno, G. Cardillo, and C. Camporeale. "Aris-Taylor dispersion in the subarachnoid space Phys. Rev. Fluids 5, 043102

- G.Cardillo and C.Camporeale. "Modeling fluid-structure interactions between cerebro-spinal fluid and the spinal cord". In: Journal of Fluids and Structures -ISSN: 0889-9746 (Under Review)

- G.Cardillo and A.I. Barakat. "Computational modeling of thrombus formation: the role of the shear micro-gradients" (under preparation)

Conference Presentations

- G.Cardillo, L. Salerno, C. Camporeale. "Valutazione della diffusività efficace di un farmaco all'interno dello spazio subaracnoideo" at XXXVI Convegno di Idraulica e Costruzioni Idrauliche

- G. Cardillo, J. Biasetti, F. Cornat, A.I. Barakat. "A computational model of chemical and mechanical platelet activation and aggregation" at 46th Europian Society of Artificial Organs Congress

- G. Cardillo, J. Biasetti, F. Cornat, A.I. Barakat. "A computational model of chemical and mechanical platelet activation and aggregation" at 8th Biennal European Cell Mechanics Meeting

Poster

G. Cardillo, J. Biasetti, F. Cornat, A.I. Barakat. "A computational model of chemical and mechanical platelet activation and aggregation" at 8th Biennal European Cell Mechanics Meeting

This Ph.D. thesis has been typeset by means of the T_EX-system facilities. The typesetting engine was pdfL^AT_EX. The document class was `toptesi`, by Claudio Beccari, with option `tipotesi=scudo`. This class is available in every up-to-date and complete T_EX-system installation.